11-2023

Climatologies of Convection Across the United States

Kristofer S. Tuftedal
Stony Brook University, kristofer.tuftedal@stonybrook.edu

Recommended Citation

Tuftedal, Kristofer S., "Climatologies of Convection Across the United States" (2023). *Electronic Dissertations and Theses*. 31.
https://commons.library.stonybrook.edu/electronic-diserations-theses/31

Climatologies of Convection Across the United States

A Dissertation Presented

by

Kristofer S. Tuftedal

to

The Graduate School

in Partial Fulfillment of the

Requirements

for the Degree of

Doctor of Philosophy

in

Atmospheric and Oceanic Sciences

Stony Brook University

November 2023

Stony Brook University

The Graduate School

Kristofer S. Tuftedal

We, the dissertation committee for the above candidate for the

Doctor of Philosophy degree, hereby recommend

acceptance of this dissertation.

Dr. Michael M. French – Dissertation Advisor
Associate Professor, School of Marine and Atmospheric Sciences

Dr. Brian Colle – Chairperson of Defense
Professor, School of Marine and Atmospheric Sciences

Dr. Mariko Oue
Research Assistant Professor, School of Marine and Atmospheric Sciences

Dr. Darrel M. Kingfield
Ph.D. in Geography, NOAA/OAR/ESRL/Global Systems Laboratory, Boulder, CO

Dr. Jeffrey C. Snyder
Ph.D. in Meteorology, NOAA/OAR/National Severe Storms Laboratory, Norman, OK

This dissertation is accepted by the Graduate School

Celia Marshik

Interim Dean of the Graduate School

Abstract of the Dissertation

Climatologies of Convection Across the United States

by

Kristofer S. Tuftedal

Doctor of Philosophy

in

Atmospheric and Oceanic Sciences

Stony Brook University

2023

Tropospheric convection is one of the most important contributors to the Earth's climate system through its transport of heat, moisture, and momentum. The hazards associated with convection (i.e., tornadoes, hail, lightning, flooding, damaging wind, etc.) are one of the largest threats to life and property. Despite the importance and wide-reaching impacts of convection, many processes both internal and external to storms are not well understood. One way to elucidate convective processes in a bulk sense is through the use of large climatologies. Radar data provide both microphysical and kinematic information about these convective storms and their hazards on fine spatiotemporal scales. The work herein is the large radar-based climatologies of shallow, modest, and vigorous deep convection with data from NEXRAD, the Geostationary Operational Environmental Satellites (GOES) 16, and the High-Resolution Rapid Refresh model, to assess differences in the characteristics and environments of various scales of air-mass thunderstorms whose initiation is primarily driven by the inland propagation of the sea-breeze front. Also developed is a radar-based climatology of supercell thunderstorms, the most intense thunderstorms on Earth, with the goal to examine the intensity and transience of low-level and midlevel mesocyclones leading up to tornadogenesis or tornadogenesis failure. Radar-derived azimuthal shear is used to assess differences in the rotational intensity and transience of the low-level and midlevel mesocyclones in strongly tornadic, weakly tornadic, and non-tornadic supercells. Near storm environment characteristics from the Rapid Refresh model are used to investigate any relationships between the storm environment and the rotational intensity and transience of mesocyclones.

Dedication Page

This dissertation is dedicated to my mom, Linda Tuftedal, who passed away somewhat suddenly on 13 November 2023. Her encouragement and support got me back into school after dropping out of high school in 9th grade and pushed me to pursue my dreams of being a tornado scientist. I absolutely would not be the person, or the researcher, I am today without her. I was fortunate that she was able to see me defend my dissertation virtually. There was no doubt of her love for my brother and me and of how incredibly proud she was of us. I love her and miss her terribly. This is also dedicated to my brother, Matt Tuftedal. The countless conversations we have had related to research have been invaluable to aiding my progress during this dissertation. Also having someone to make dumb jokes with about topics that only other atmospheric scientists understand helped. This dissertation is dedicated to all the people that have helped me get to where I am today. The people who supported me when I struggled to believe in myself. To my advisor, Michael French, for his continued support and advice through the years. To my girlfriend, Alicia LaCross, for being everything I have ever needed you to be without me ever having to ask for it. You are the love of my life. To one of my best friends in the world, A.J. Chapman. You are a second brother to me and have helped me get to where I am today more than you will probably ever know. The countless weekends spent chatting and playing video games together were the releases I needed when life was beating me to a pulp. To my friends from undergrad at Iowa State University and everyone I met at Stony Brook University. You are all a big part of why I am where I am today. To the instructors that I had during my time at Kalamazoo Valley Community College. Without their guidance, there is no chance I would have survived the math and physics needed to get to this point. All of your love and dedication for your respective subject matters is what has made me think so highly of community college and why I think everyone should be able to attend them free of cost. Lastly, I would like to dedicate this dissertation to the people who doubted me and told me, to my face, that I would never amount to anything. None of you would have ever guessed that I would be receiving a Ph.D. in anything, let alone a field as complicated as atmospheric science. Your doubt in me drove me to prove you all wrong.

Table of Contents

List of Tables

List of Figures

List of Abbreviations

AGL - Above Ground Level

AOD - Aerosol Optical Depth

ARL - Above Radar Level

ARM - Atmospheric Radiation Measurement

AzShear - Azimuthal Shear

CAPE - Convective Available Potential Energy

CDT - Central Daylight Time

CI - Convective Initiation

CIN - Convective Inhibition

CM1 - Cloud Model 1

DFW - Dallas-Fort Worth

DOE - Department of Energy

EF - Enhanced Fujita Scale

ESCAPE - Experiment of Sea Breeze Convection, Aerosols, Precipitation, and Environment

ETH - Echo Top Height

F - Time of Tornadogenesis Failure

G - Time of Tornadogenesis

GOES-16 - Geostationary Operational Environmental Satellite-16

GOESBT - GOES-16 Channel 13 Cloud Top Brightness Temperature

H_{EBase} - Cell Echo Base Height

H_{dBZmax} - Height of Cell Maximum Radar Reflectivity

HRRR - High-Resolution Rapid Refresh Model

KHGX - Identifier for the WSR-88D Radar near Houston, Texas, and the Houston/Galveston National Weather Service Office

LLM - Low-Level Mesocyclone

LCL - Lifting Condensation Level

MCS - Mesoscale Convective Systems

MCIT - Multi-Cell Identification and Tracking

MLM - Midlevel Mesocyclone

MSP - Minneapolis

MU - Most Unstable

MUCAPE - Most Unstable Convective Available Potential Energy

NCAR - National Center for Atmospheric Research

NEXRAD - Next-Generation Radar

NRC - National Research Council

NRL - Naval Research Laboratory

NSE - Near Storm Environment

NSF - National Science Foundation

NWS - National Weather Service

RAP - Rapid Refresh Model

SPC - Storm Prediction Center

SRH - Storm Relative Helicity

TRACER - Tracking Aerosol Convection Interactions Experiment

UTC - Coordinated Universal Time

VCP - Volume Coverage Patterns

VIL - Vertically Integrated Liquid

VORTEX2 - Verifications of the Origins of Rotation in Tornadoes Experiment 2

VPPGF - Vertical Perturbation Pressure Gradient Force

WSR-88D - Weather Surveillance Radar - 1988 Doppler

Z_H - Radar Reflectivity Factor

Acknowledgments

The work contained in this dissertation was generously funded by NSF Grant AGS-2019968 (Kollias and Oue), the U.S. DOE Grant DE-SC0021160 (Oue), NSF Grant AGS-1748177 (French), NSF Grant AGS-2303590 (French), and NSF Grant AGS-1748177 (Kingfield). We would also like to acknowledge Darrel Kingfield for providing the processed radar data used for analyses within the mesocyclone climatology work. Lastly, we would like to acknowledge Bernat P. Treserras for his work in developing the convective cell detection and tracking algorithm and providing the convective cell database used for the convective cell climatologies.

Chapter 1

Climatologies of Sea-Breeze Induced Convection on Various Scales

1.1 Introduction

Tropospheric convection plays a pivotal role in the Earth's climate system, facilitating the transport of heat, moisture, and momentum. These processes are strongly dependent on cloud evolution. While an ordinal convective model is proposed, the variability in cloud evolution, stemming from environmental and diurnal factors, introduces uncertainties in convective parameterizations in numerical climate and cloud models (e.g., Bony et al. 2015; Fridlind et al. 2017; Ladino et al. 2017; Colin and Sherwood 2021). Modeling studies have attempted to address these uncertainties but have been constrained by the lack of high-quality observational data for validation (Lee et al. 2008; Zhu et al. 2012; Varble et al 2014; Igel et al. 2015; Peters et al. 2019). Previous studies primarily focused on observed reflectivity, limiting their ability to analyze microphysical aspects. However, recent advancements in simulating polarimetric variables using forward operators offer a promising avenue for understanding changes in storm microphysics through comparisons with observed polarimetry (Ryzhkov et al. 2011; Wolfenberger and Bern 2018; Kumjian et al. 2019).

Convection encompasses a broad spectrum, ranging from short-lived shallow convection, such as air-mass thunderstorms with lifetimes of approximately 30 minutes, to long-lived deep convection, including single cells, multicells, squall lines, and supercells, which can maintain their intensity for several hours. The near storm environment (NSE), comprising the surrounding atmospheric conditions and local topography, plays a critical role in shaping the lifecycles of convective phenomena (Thompson et al. 2013; Mulholland et al. 2018; Kerr et al. 2019; Chavas and Dawson 2021). Studies on coastal convection have shown that convective storms do not rely on synoptic-scale meteorological conditions in the same way as purely continental or maritime convection (e.g., Bergemann and Jakob 2016; Birch et al. 2016). The lack of dependence on synoptic-scale forcing allows for the investigation of convective processes independent of the larger scale meteorology.

Deep convection intensity and frequency have been observed to be more pronounced downwind of larger cities, such as Dallas-Fort Worth (DFW) and Minneapolis (MSP), compared to smaller cities (Kingfield et al. 2018). When comparing the upwind and downwind distributions of horizontal radar reflectivity factor (Z_H), vertically integrated liquid (VIL; Greene and Clark 1972; Amburn and Wolf 1997), and maximum expected size of hail (MESH), all cities analyzed showed an enhancement in the region downwind from each city. Of the four cities (DFW, MSP, Oklahoma City, and Omaha) analyzed, the strongest enhancement signals occurred for the two large cities (DFW and MSP) where Z_H, VIL, and MESH all showed significant differences between the upwind and downwind distributions of each variable. The Houston metropolitan area is quite similar in size to DFW (4608 km^2 compared to Houston's 4306 km^2), therefore it stands to reason that Houston may show a similar downwind enhancement in deep convection. However, the other cities are far from the coast. Does the influence of the sea-breeze circulation on deep convection overshadow any downwind-of-urban enhancement?

In coastal regions, the land-sea breeze circulation emerges as a key forcing mechanism for convective initiation (CI), primarily through an increase in surface convergence (Haurwitz 1947; Rotunno 1983). The land-sea breeze circulation provides a unique opportunity to study the effects of the NSE on convective lifecycles, irrespective of large-scale conditions, thus allowing for more direct attribution of these effects on storm characteristics. For instance, the Houston, Texas coastal region, characterized by a prevalent land-sea breeze circulation and varying aerosol concentrations, presents a valuable case for investigating the influence of aerosols on convective processes through convective invigoration (Lebo 2018).

The ongoing debate about warm- and cold-phase convective invigoration (how aerosol particles affect convective intensity based on different releases of latent heat) in the literature (i.e., Lebo and Seinfeld 2011; Sheffield et al. 2015; Fan et al. 2018; Abbott and Cronin 2021; Igel and van den Heever 2021; Grabowski and Morrison 2021) underscores the need for high-quality observational datasets. The collection of a robust observational dataset that can be used as an observational benchmark for modeling studies is challenging. Such a dataset requires a sufficiently large sample size of convective cloud properties over a wide range of meteorological and aerosol conditions using a convective cell centric approach rather than domain averaging approaches that fail to capture the lifecycle of convective clouds.

Results from previous studies of long-term remote sensing data collected in Houston suggest that variability in convective cloud microstructure, hydrometeor properties, and electrification is correlated to variability in aerosol conditions over and downwind of Houston (Hu et al. 2019a, b). In previous studies, National Weather Service (NWS) Weather Surveillance Radar – 1988 Doppler (WSR-88D; Crum 1993; Radar Operations Center 2022) radar observations were used to track convective cells during different cloud condensation nuclei (CCN) conditions (satellite-retrieved; Rosenfeld et al. 2016), and to investigate how variability in cloud, precipitation and lightning characteristics related to CCN conditions, though the studies neglected proper control of meteorology. Also, a recent pilot study has identified the need to collect observations of convective clouds at a temporal and spatial resolution higher than is possible from the existing operational observations (Fridlind et al. 2019). Past work show large variabilities of convective cloud properties associated with cloud lifecycles. In addition, cloud lifecycles also vary from one individual cloud to another. The observed variabilities make it prudent to analyze very large datasets worth of convective clouds to obtain more representative bulk statistics. A lack of generalizable data also hinders our ability to evaluate cloud model simulations.

In order to address the summarized challenges, a coordinated effort was undertaken in the greater Houston, Texas metropolitan area and surrounding region from 2021 to 2022 to collect a comprehensive dataset of isolated convective cells (Jensen et al. 2022). Such efforts were consolidated in the Tracking Aerosol Convection interactions Experiment (TRACER) supported by the United States Department of Energy (DOE) Atmospheric Radiation Measurement (ARM) facility and the National Science Foundation (NSF) Experiment of Sea Breeze Convection, Aerosols, Precipitation and Environment (ESCAPE) campaign. The study region was selected because it is warm and humid in the summer and commonly experiences onshore flow and sea breeze-forced CI.

To validate modeling studies and address the shortcomings in observational data, climatologies utilizing high-resolution radar data and forecast model data on short timescales are crucial. Weather radars, like the WSR-88D, provide high-quality, high spatiotemporal resolution data for studying atmospheric convection. WSR-88D data can be compared with model simulations through radar simulators (e.g., Oue et al. 2020). Satellite systems like the Geostationary Operational Environmental Satellite-16 (GOES-16) also offer high spatiotemporal resolution data of convective characteristics that radar cannot measure, such as cloud top brightness temperature, a characteristic which is commonly used as a proxy for cloud top height, for example. This study aims to address the gap in modeling work and the need for large climatologies by utilizing a convective cell centric methodology to provide climatological datasets of coastal shallow and deep convective cells using WSR-88D, GOES-16, and High Resolution Rapid Refresh model (HRRR; Smith et al. 2008; Dowell et al. 2022; James et al. 2022) data. By applying strict thresholding criteria, we distinguish different types of convective cells (shallow, modest deep, and vigorous deep convection) and conduct sensitivity testing to assess the robustness of our results. The use of a comprehensive approach aims to address the need for more representative bulk statistics of convective phenomena and facilitate the evaluation of cloud model simulations.

Objective 1: Conduct a four-year (2018–2021) climatology of convective cells in the Houston metropolitan area using WSR-88D and GOES-16 data to better understand characteristics of shallow and (modest and vigorous) deep convection.

Objective 1 used this four-year convective cell climatology to address the following research questions:

- Do we observe the three convective types (shallow, modest deep, and vigorous deep)?
- What convective cell types are dominant depending on area and time?
- What are the bulk statistics for the characteristics of each convective type?
- Do convective cells exhibit any preference in initiation location around the greater Houston metro?
- How might the NSE at the location of cell initiation affect convective type?
- How might the aerosol concentration affect cell initiation and eventual cell characteristics?
- Can we derive approximate draft speeds from WSR-88D or GOES-16 data?

1.2 Data and Methods

1.2.1 Domain and Data

Our study domain was centered on the KHGX WSR-88D near Houston, Texas and extended ±125 km to the north, east, south, and west, creating a 250 km by 250 km domain. The Houston region was selected because the coastline with the Gulf of Mexico generates regular land-sea breeze circulations which provide a forcing mechanism for CI. The chosen domain also provides regions of relatively “pristine” and “polluted” aerosol regimes to the southwest and northeast respectively. The area to the northeast of Houston is generally downstream of pollution sources, such as the Houston metropolitan area itself and oil refineries near Houston, allowing for the advection of this polluted air over this sub-region. The area to the southwest of Houston is generally upstream and made up of mostly rural land even further upstream, allowing the air here to be far less polluted.

Data from KHGX, GOES-16, and the HRRR were collected for the period of June through September 2018–21 where CI occurred during local daytime, 09:00–21:00 Central Daylight Time (CDT). Initiation during local daytime was chosen to increase the likelihood that sea breeze propagation was a primary forcing mechanism for CI and to enable the analysis of GOES aerosol optical depth (AOD) data.

During the study period, the volume coverage patterns (VCPs) available to KHGX changed with the implementation of VCP 215 (15 elevation angles from 0.5˚ to 19.5º) and 112 (14 elevation angles from 0.5˚ to 19.5º) and the removal of VCPs 11, 211, 21, and 221 (Radar Operations Center 2015; Zittel 2019). Aside from differing VCPs, different dynamic scanning techniques can adjust how the radar scans without changing the VCP (Chrisman 2009; 2013; 2014; 2016). The differing VCPs and dynamic scanning techniques have an effect on the time required to complete a single

VCP. Despite variations in rescan time, the time required to complete any of the VCPs is ~5 minutes. Different VCPs also collect slightly different sets of elevation data, which can substantially affect the uncertainty in any height or VIL analyses presented herein.

Z_H from KHGX was collected during normal weather surveillance operations and horizontally regridded to a 250 km by 250 km domain with 500 m by 500 m horizontal spacing for each volume scan. The height was calculated based on the elevation angle and range. The gridded data was then used to estimate VIL, radar-derived echo top height (ETH), and radar-derived profile depth (H_{cell}).

HRRR data were regridded to the same 500 m by 500 m grid used for Z_H. We calculated VIL from gridded Z_H data from KHGX using equation (1):

$$VIL\ (dB) = 10 * \log_{10}\left(\frac{\sum_{i=0}^{i=(i_{max}-1)} 3.44 * 10^{-6}\left[\frac{(Z_i + Z_{i+1})}{2}\right]^{4/7} dh}{1\ {}^{kg}/_{m^2}}\right) \tag{1}$$

where i_{max} is the total number of sweeps for a given VCP, Z is the radar reflectivity of a given sweep (i) in units of mm^6 m^{-3}, and dh is the vertical spacing between sweeps. VIL assumes a Marshall-Palmer drop-size distribution, which introduces uncertainty since it may not be completely valid for convective events in coastal regions. Other sources of uncertainty in VIL include beam spreading with increasing distance from the radar and data sparsity at high elevations within 30 km of KHGX. The uncertainty from beam spreading with distance has been shown to be relatively small, but VIL within 30 km of the radar tends to be underestimated for 5-minute WSR-88D VCPs (Oue et al. 2022).

GOES-16 Channel 13 cloud top brightness temperature data (GOESBT) were analyzed such that each 5-minute image was linked to the KHGX scan time nearest to each GOESBT product time. GOES-16 AOD calculations require cloud-free pixels to generate AOD data. In many cases, the location of cell initiation already contains some form of cloud cover (be it low-, middle-, or upper-level clouds) at the time of initiation, which inhibits AOD generation. When AOD values are generated, they are classified as low-, medium-, or high-quality returns. To ensure a large enough sample size, AOD data denoted as medium- or high-quality were temporally averaged for the 30 minutes preceding cell initiation at the location of cell initiation.

1.2.2 Cell Tracking

Convective cells were detected and tracked as a part of the Multisensor Agile Adaptive Sampling flamework (Kollias et al. 2020; Lamer et al. 2023) using the KHGX and GOES-16 datasets. KHGX VIL and GOES-16 observations were used as input to a modified version of the multi-cell identification and tracking (MCIT) algorithm (Rosenfeld 1987; Gagin et al. 1985; Hu et al. 2019a) to track all features with VIL of ≥ -20 dB during that period. Detailed specifics of the MCIT algorithm can be found in Hu et al. (2019a). The MCIT algorithm ingests time series of volume scans and tracks local maxima of VIL by identifying the two cells in consecutive radar scans that have common maximum VIL (i.e., the areas of VIL have some overlap from one time to the next.) To check for overlap from timestep to the next, pySTEPS (Pulkkinen et al. 2019a,b) is used to compute velocity fields and find the shift in images. The current image is then checked with the advected cell from the computed velocity field and checks for overlap between the actual cell and computed cell location. The tracking continues until the cell dies, splits, or merges.

The algorithm was modified to account for ambiguous situations in cell identification and tracking. When iterating over all cells, an ambiguous situation arises when more than one cell (cell A and cell C) considers the same neighbor (cell B) as a candidate for cell merging. In this case, the algorithm has been modified to merge the cells with the same neighbor (cells A and C merge with cell B) and with one another (cells A and C merge together), recursively. In cell tracking, an ambiguous situation may arise in two different scenarios:

1. A cell from *map(t+1)* is the potential split or continuation of two or more cells from *map(t)*. In this case, continuation has been set to prevail over split situations. Nevertheless, if different cells from *map(t)* are the potential source of the cell from *map(t+1)*, the cell with maximum integrated common VIL is the one selected.
2. A cell in *map(t)* has two or more potential split or continuity cells in *map(t+1)*. In this case, as before, continuation prevails over split situations, but if different cells are candidates, the cell with maximum integrated common VIL is the one selected. Only one cell can be defined as continuity, the rest are labelled as splits.

The outlined modifications of the MCIT algorithm have improved the cell tracking continuity by providing more persistent representations of evolving cells. Detailed description of the cell tracking algorithm is also available in Lamer et al. (2023). The initial analysis from the modified MCIT algorithm identified 1,664,215 features with a VIL value ≥ -20 dB during local daytime (09:00 to 21:00 CDT).

1.2.3 Cell Classification

To better characterize evolution of each cell, we employed the following cloud properties:

1) ETH: the height at the middle of the highest gate with detectible signal (Z_H > -10 dBZ) from KHGX;

2) H_{cell}: the depth between the top of the highest gate of the radar detectible signal for a cell and the bottom of the lowest gate of the radar detectible signal (not corrected for increasing altitude with increasing range from the radar).

3) ERatio (Fig. 1.1): the ratio of the ETH to H_{cell}; and

4) the tracked cell area based on VIL (Area)

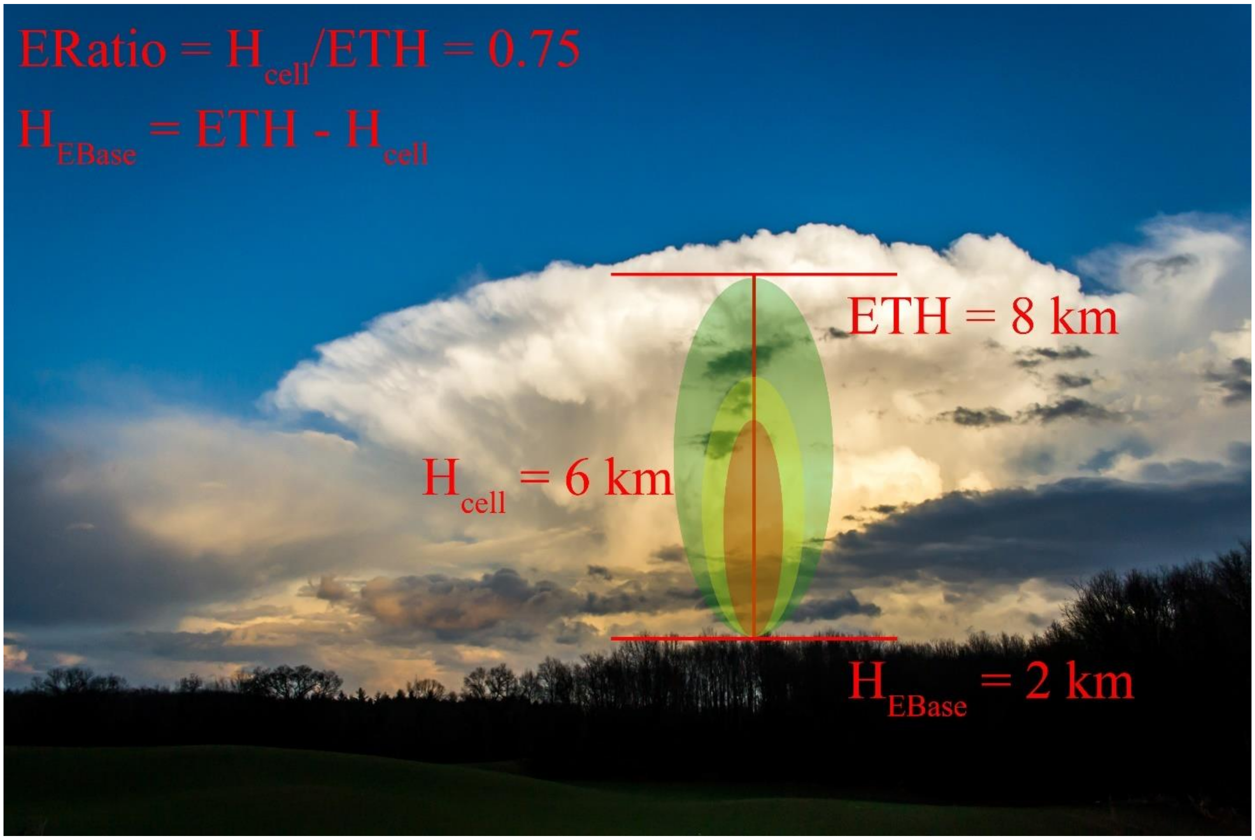

Figure 1.1: A visual illustration of ERatio, H_{cell}, and H_{EBase}. The image is meant to provide a visual context for the three variables. The red, yellow, and green shaded areas represent arbitrary high, medium, and low reflectivity contours respectively. ERatio and H_{EBase} are calculated using the maximum ETH and H_{cell}, which are radar-derived quantities and will always be less than the actual height of the storm top and physical depth of a given cell.

Using the three properties, and GOESBT and VIL, we classified tracked features into three categories: 1) shallow, 2) modest deep, and 3) vigorous deep convective cells. Thresholds for the classification are listed in Table 1.1. The thresholds were empirically derived to avoid false classification of cloud systems such as high cirrus clouds, mesoscale convective systems (MCSs), or large regions of stratiform precipitation. We also used the initial cluster fraction of the cell, which is the ratio of the area of a given cell to the area of a cluster (parent) of the cell at the beginning of the cell lifetime, equal to 1 (a value of 1 meaning the cell is discrete). The split/merged cells are removed in this study. The area threshold is used only to classify the shallow cells to ensure that such shallow features are not large regions of stratiform precipitation. The use of extensive thresholding removes noisy features, likely due to non-meteorological echoes (e.g., ground clutter, insects, etc.). Cells that have their "birth" or "death" occur on a domain edge are removed to avoid analyzing cases which are ongoing before or after entering or leaving the study domain. Cells which pass within 15 km of KHGX are also removed to mitigate the lack of data in the "cone of silence."

	Shallow Convection	Modest Deep Conv.	Vigorous Deep Conv.
Initial Cluster Fraction	1	1	1
Lifetime Min. GOESBT	≥ 268 K	≤ 250 K	≤ 250 K
Lifetime Max. VIL	≥ -10 dB	≥ 0 dB	≥ 0 dB
Lifetime Max. ETH	< 8 km	8 ≤ ETH < 12 km	≥ 12 km
Lifetime Max. ERatio	≥ 0.60	≥ 0.75	≥ 0.75
Lifetime Max. Area	≤ 30 km^2	N/A	N/A
Splits/Merges Removed	Yes	Yes	Yes
# of cells	35,996	7,935	4,869
# of radar scans	142,923	92,798	95,219

Table 1.1: A table of the thresholds used to isolate shallow, modest deep, and vigorous deep convection from all tracked features from the modified version of the MCIT algorithm.

The shallow and deep convective cells selected based on the thresholds were then analyzed separately and compared with one another. Sensitivity studies were also performed on each case type by varying all thresholds (except initial cluster fraction and split/merge status) by ±5% individually and simultaneously to observe any changes in the distributions of certain variables for each case type.

1.2.4 Climatological Analyses and Statistical Analysis

Cell properties introduced in sections 1.2.2 and 1.2.3 for all cells classified into the three categories during the four-year observation period were examined to allow for bulk analyses of cell type characteristics. Analyses used herein include observations during specific times during cells' lifetimes (such as the time of initiation), aggregates of all scans from the entire lifecycle of all cells of a given type, changes in variables over cell-normalized lifetimes, diurnal changes in the given variables, and spatial differences in initiation location. Our analysis strategy enabled us to investigate how cells changed as they grew, matured, and decayed, as well as allowed for the direct comparison of how case types differ from each other.

To parse out any potential environmental controls on shallow and deep CI and intensity, HRRR model data and GOES-16 AOD data were analyzed. The HRRR data were utilized to collect the convective available potential energy (CAPE), convective inhibition (CIN), various shear parameters, and vertical profiles of temperature, dew point, and wind speed and direction interpolated to the grid point of a given cells' initiation point for the forecast hour prior to each cells' initiation time. The AOD data were analyzed to investigate any role that aerosol loading may play in affecting CI. The nonparametric Mann-Whitney U test was used to investigate statistical differences among regional cell initiation AOD distributions (Mann and Whitney 1947). To further elucidate any differences between case types or within a given case type, days where the number of cells of a specific type exceeded the 95th percentile of the number of cells for days where those cell types were present were selected and analyzed separately.

1.3 Results

The empirically derived thresholds shown in Table 1.1 were used to isolate shallow, modest deep, and vigorous deep convective cells from all other features tracked by the modified MCIT algorithm. Use of the summarized thresholds provided 35,996 shallow, 7,935 modest deep, and 4,869 vigorous deep convective cells for analysis over the four-year observation period.

1.3.1 Overall Cell Characteristics

The monthly average number of cells varies little from month to month for June, July, August, and September and is highest in August for all three case types (Fig. 1.2). In general, there is approximately an order of magnitude more shallow convective events than modest deep or vigorous deep convective cells for any given month.

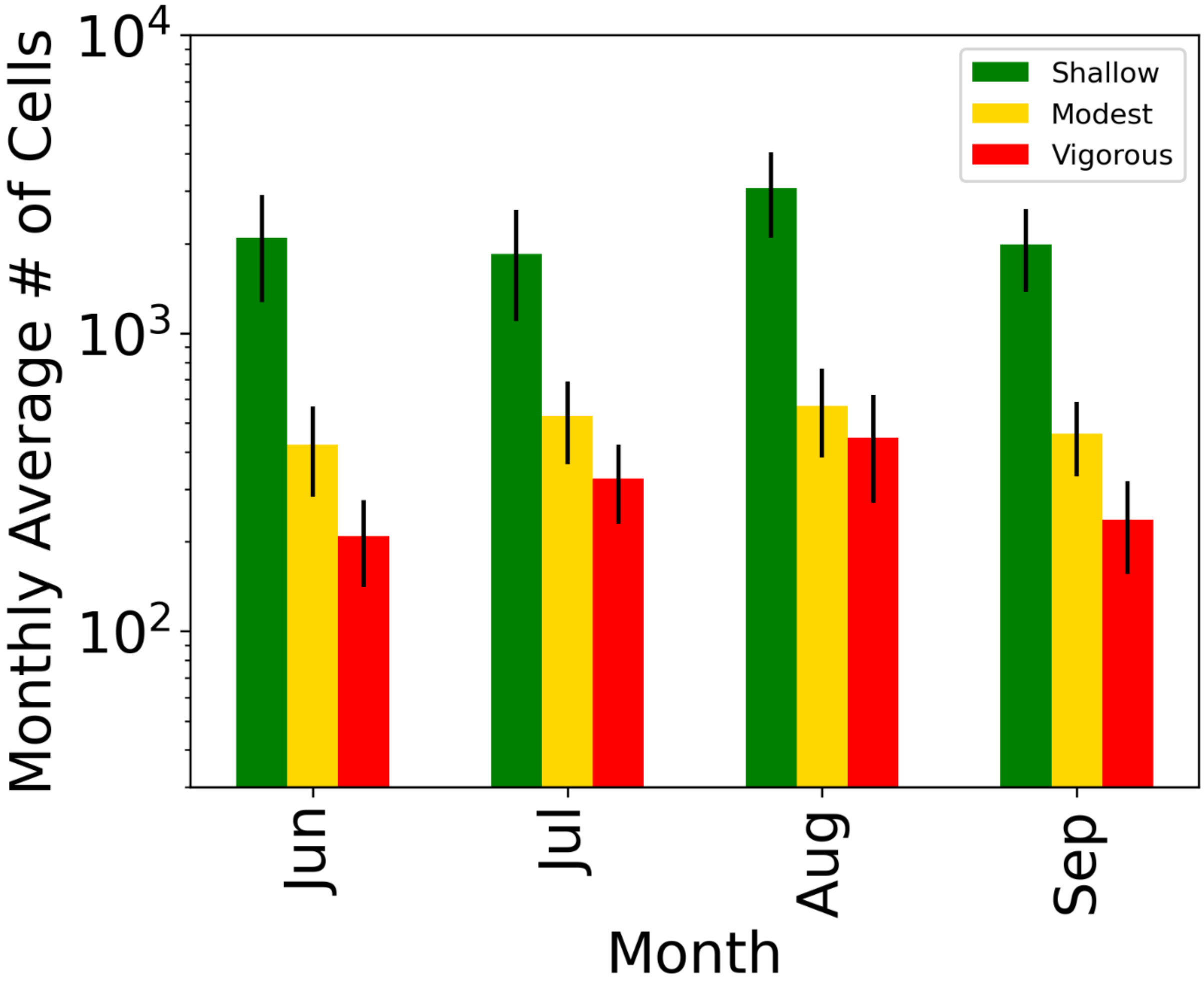

Figure 1.2: Bar graphs showing the monthly average cell count for shallow (green), modest deep (yellow), and vigorous deep (red) convection. The vertical black lines at the top of each bar denote ± one standard deviation.

Storm motion could be important for understanding storm evolution, so propagation speed and direction of cell motion were analyzed. Figure 1.3 shows the frequency distributions of the propagation speed and direction as a function of normalized lifetime for the three cell types investigated. The frequencies shown are normalized by the total number of samples at each normalized lifetime bin (every 0.025). All cell types tend to have storm motions ranging primarily between southerly to easterly. Shallow convective cells, on average, move the slowest out of the three cell types and have less variability in speed than modest and vigorous deep convective cell.

Over the lifetime of these cells, shallow convective cell speed varies little and is much slower when compared to deep convection. Overall, for the three categories, the convective cells mainly tend to have storm motions spanning from southwesterly to easterly. Larger variability in storm motion is found at the later period of the cell lifetime for modest and vigorous deep cells, where the greatest variability is seen in the vigorous deep cells. Therefore, some of the vigorous deep convective cells may be supercellular in nature because of the large deviations from the early storm motions near the time of initiation, but the presence of supercells cannot be confirmed without further analyses of detailed conditions for supercells outside of the scope of this research. The direction of cell motion (particularly early in the lifetimes of these cells) indicates the possibility that the sea breeze along the Gulf Coast plays a part in storm initiation and propagation as the observed directions would be consistent with the inland propagation of the sea-breeze, which propagates from southeast to northwest from the coastline.

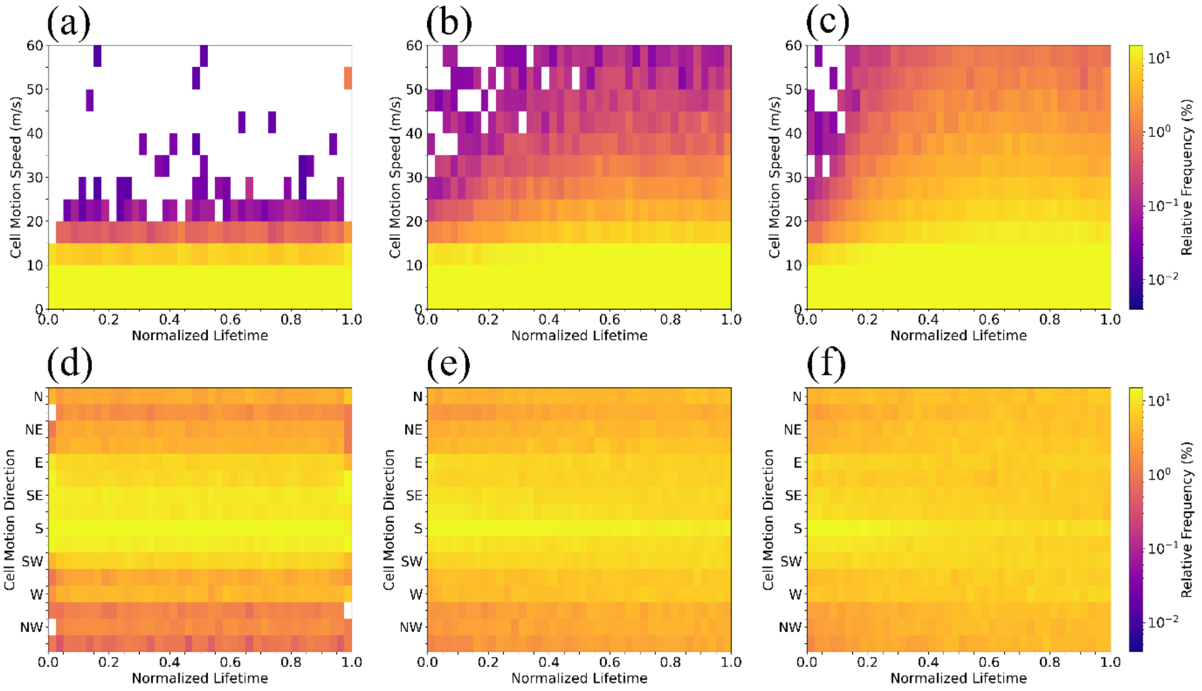

Figure 1.3: The normalized lifetime distributions of the bin count normalized cell motion speed (a, b, c) and cell motion direction (d, e, f) for all shallow (a, d), modest deep (b, e), and vigorous deep (c, f) convective cells.

1.3.2 Location and Diurnal Frequency of Initiation

Figure 1.4 shows the diurnal frequency of initiation times as a function of local time. All cell types have their peak in initiation in the late morning/early afternoon hours, which then sharply decreases as the day progresses. Overall, all types of convection in the Houston region preferentially initiate in the late morning/early afternoon. However, there is a slight difference in peak time. Shallow convection and vigorous deep convection show earlier peaks in initiation time – between 10:00 and 14:00 CDT – when compared to the peak for modest deep convection, which is shifted slightly later (between 12:00 and 15:00 CDT; Fig. 1.4). The outline differences are not statistically significant.

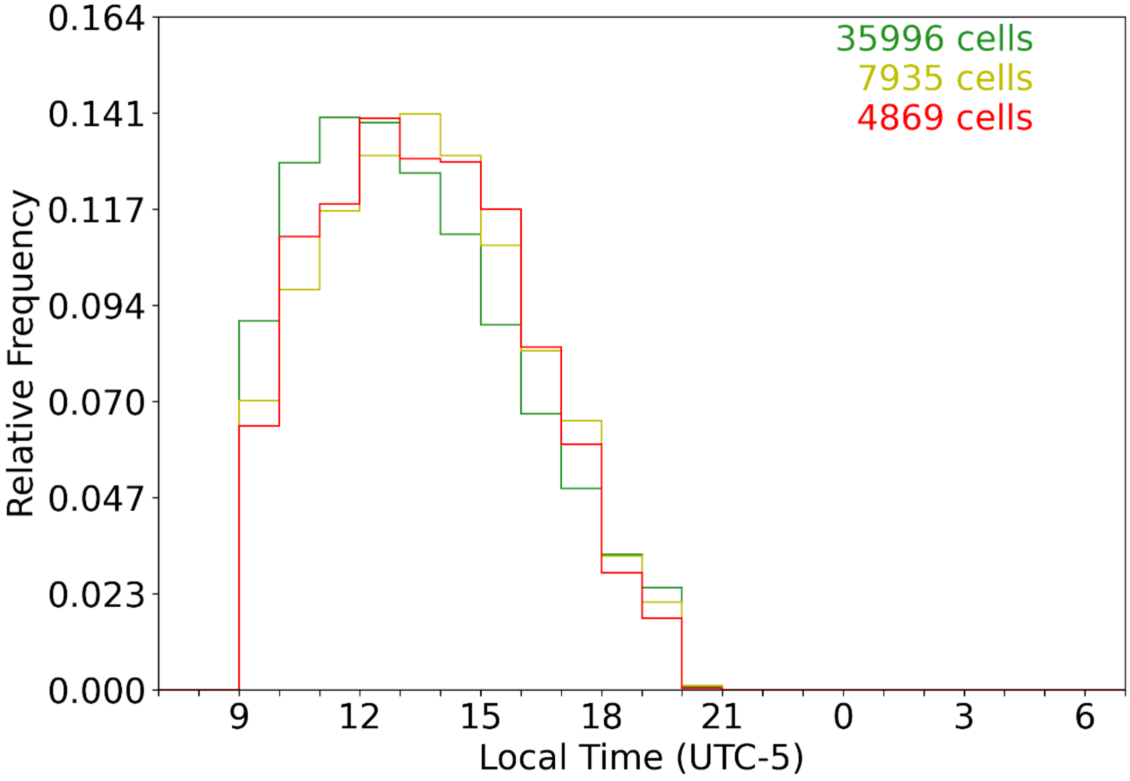

Figure 1.4: The frequency of initiation based on local time of day for (green) shallow convection, (yellow) modest deep convection, and (red) vigorous deep convection.

Figure 1.5 shows the initiation location for shallow (Fig. 1.5a,d,e), modest deep (Fig. 1.5b,e,h), and vigorous deep (Fig. 1.5c,f,i) convection. The three types all show a preference to initiate over land along the coastline to the southwest and northeast of Houston (within 100 km from the coast) with a local minimum in initiation over Galveston Bay (the large bay to the east of Houston), suggesting that a land-sea contrast, hence sea breeze, is a key factor for CI in this area. The inland propagation of the sea breeze can also be observed based on the cells' overall speed and direction of travel early in their lifetimes (Fig. 1.3). One feature of note is the obvious preference in shallow CI to the southwest of Houston (Fig. 1.5a,d,e). Another notable feature is that both moderate and vigorous deep convective cell types show a local maximum over the Houston metropolitan area, which is especially apparent in vigorous deep convective cases. The observed initiation maximum could be caused by the enhancement from aerosol loading and/or urban heating, but will need further examination in the future. There is an obvious inland shift in initiation location, that is most obvious for vigorous deep convection, from the 09:00-11:59 to 12:00-14:59 CDT period, further supporting the influence of the sea breeze on CI for all case types. The diurnal spatial shift in initiation location shows that the sea breeze is a key factor for CI along the coast. Figures 1.4 and 1.5 highlight that the early afternoon hours are the most preferable time for CI for all cell types, and observation that is consistent with previous studies (e.g., Park et al 2020).

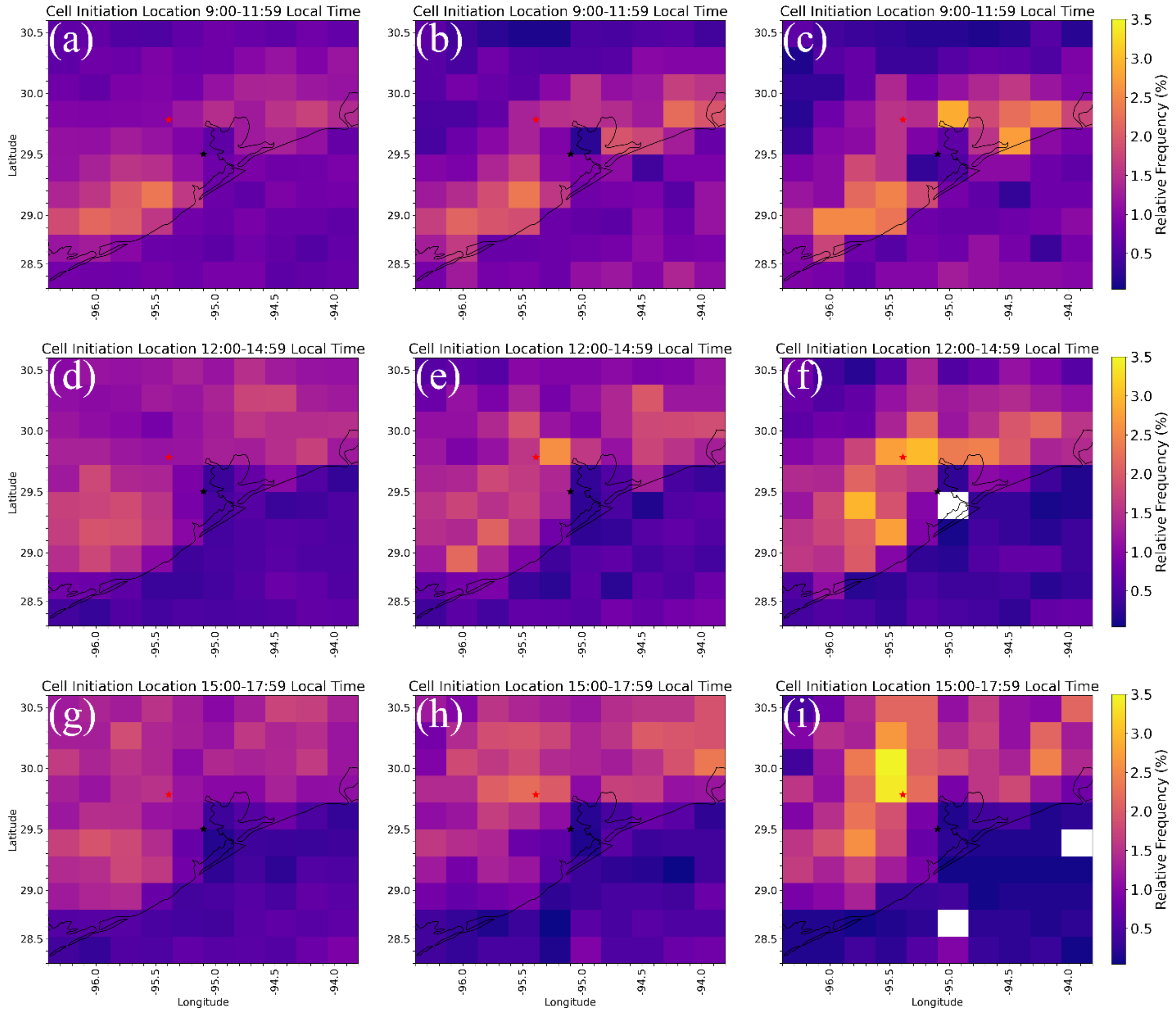

Figure 1.5: Maps showing the spatial distributions of initiation locations normalized by the number of cells that initiated during that period for the 3-hour periods 09:00 to 11:59 (a, b, c), 12:00 to 14:59 (d, e, f), and 15:00 to 17:59 (g, h, i), local time for shallow (a, d, g), modest deep (b, e, h), and vigorous deep (c, f, i) convection. The black (red) star in each plot denotes the location of KHGX (downtown Houston).

The domain maximum in shallow CI to the southwest of Houston is also apparent in all periods except 18:00-20:59 CDT (not shown), but modest and vigorous deep convective types do not visually show the same southwest initiation preference. Rather, the two deep convective types (especially vigorous deep convection) show maximums in initiation over the Houston metropolitan area in the mid-to-late afternoon. We further speculate that this may be the result of urban heating allowing parcels to reach their convective temperatures during this time, even on days where CAPE is high, but CIN elsewhere in the domain is too strong to allow for other convection to initiate. However, as stated previously, further research is necessary to elucidate what mechanism(s) is(are) responsible for this local initiation maximum in deep convection.

1.3.3 Diurnal Changes in Cell Characteristics

To assess the diurnal cycle of convective cells, we analyzed cell hour-by-hour basis characteristics for each scan for the duration of its life over the course of the day. Figure 1.6 shows the diurnal trends in the distributions of GOESBT, the height of cell maximum radar reflectivity (H_{dBZmax}), and the cell maximum radar reflectivity (dBZ_{max}) for all scans of all convective cases. For shallow cells, the GOESBT tends to be constant at around 285 K over time, and the majority of the cells have H_{dBZmax} values generally below 6 km. In contrast, the two deep convection types exhibit similar maximum frequencies of GOESBT before noon with a substantial shift of the maximum frequency to ~240 K for modest deep cells and ~220 K for the vigorous deep cells around noon, then taper off into the later evening and overnight hours. The frequency peak of H_{dBZmax} for the modest and vigorous convective types is found below 6 km before noon, similar to shallow cells, which then shifts to 6–10 km for modest deep cells and 9–13 km for the vigorous deep cells until ~18:00 CDT for modest deep cells and 23:00 CDT for vigorous deep cells, suggesting a production of significant amount of solid hydrometeors. ETH also shows the same change in characteristics as GOESBT and H_{dBZmax} (not shown), further supporting late morning/early afternoon initiation. There is little dependency of maximum reflectivity on time.

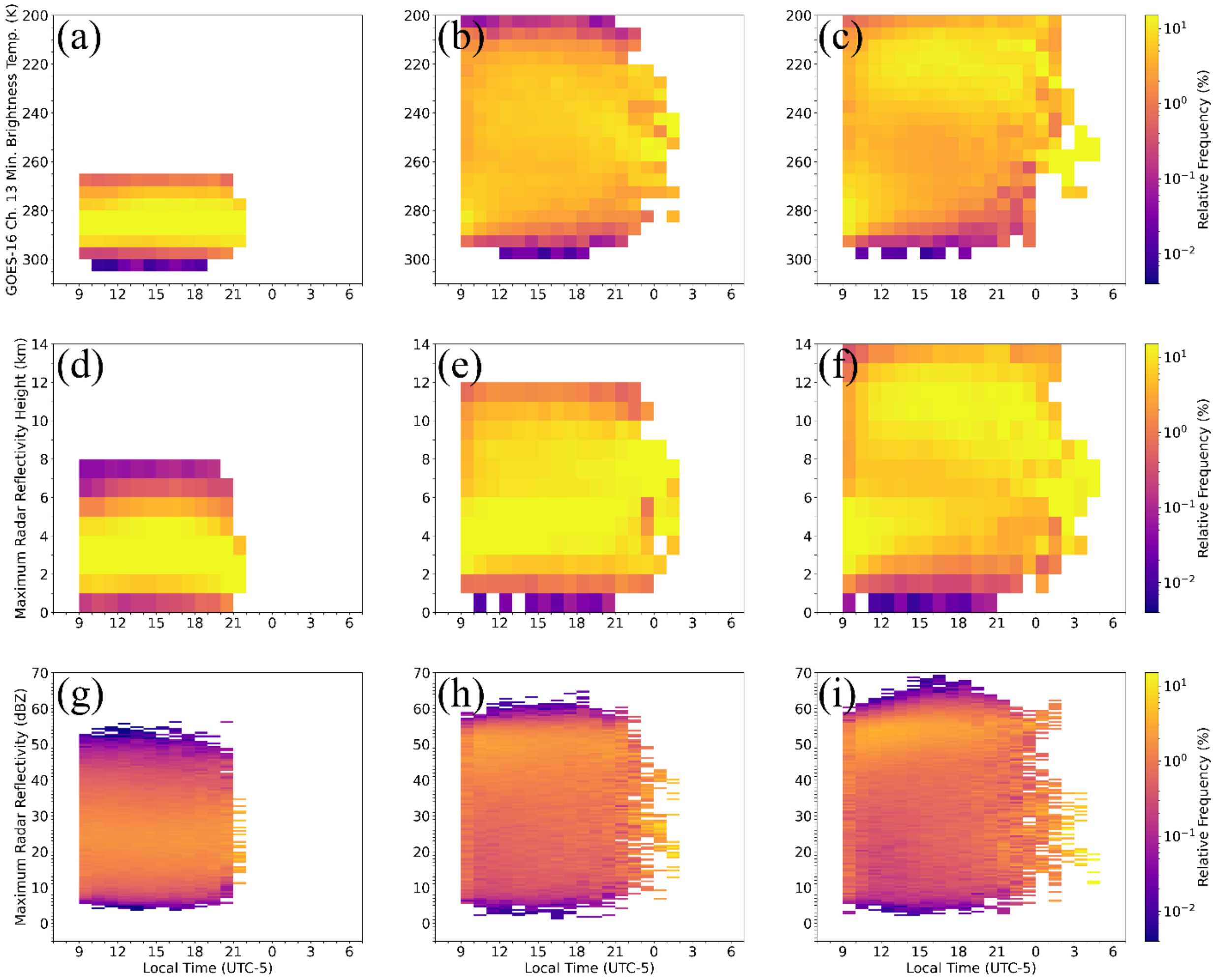

Figure 1.6: The time bin normalized distributions of GOESBT (a, b, c), H_{dBZmax} (d, e, f), and dBZ_{max}(g, h, i) over the course of a day for all scans over the lifetimes of shallow (a, d, g), modest deep (b, e, h), and vigorous deep (c, f, i) convection.

1.3.4 Analysis of Bulk Cell Type and Normalized Cell Lifetime Characteristics

Even though the peak in CI has been shown to occur in the late morning/early afternoon, and peak in intensity in the early-to-mid afternoon, there may be diurnal variability and differences in duration in cell lifetime that are unaccounted for. To observe how cells behave over the course of their lifetimes rather than the course of a given day, we have also analyzed cells by aggregating scans during specific periods of cell lifetimes, aggregating all scans of all cells of each type, and by normalizing each by its respective lifetime. Doing so allows for direct comparisons of case types, regardless of what time the cells initiated or how long they lasted.

The growth and decay of cells can be seen by analyzing the change in the distributions of dBZ_{max}, H_{dBZmax}, maximum VIL, GOESBT, and the average of the maximum radar reflectivity for all columns within a given cell (dBZ_{avg}). Shallow convective cells show overall low dBZ_{max} at low H_{dBZmax} over the course of entire cell lifetimes (Fig. 1.7). Cell growth and decay is apparent, as H_{dBZmax} and dBZ_{max} shift to overall higher values during the first half of cell lifetimes and then decrease back to a distribution that looks most similar to cell initiation at the end of their lifecycles. Modest and vigorous deep convection show clear signals of the formation (Fig. 1.7b,c), mature (Fig. 1.7e,f,h,i), and dissipation (Fig. 1.7k,l) phases. Early in their lifetimes, the cell types are dominated by low dBZ_{max} values at low H_{dBZmax}, which both increase considerably moving into their mature phases. An increasing trend is especially apparent in vigorous deep convection, where early in cell lifetimes, there is a clear signal of initiation and some cells that have begun to grow (based on the secondary maximum in high dBZ_{max} at high H_{dBZmax} values). As the cells continue to mature, we see that H_{dBZmax} remains high, but that dBZ_{max} begins to decrease, which is indicative of cells where the convective core has dissipated leaving “orphan anvils” (Hitschfeld 1960). However, H_{dBZmax} is slightly skewed by bright banding, as both modest and vigorous deep convection show unnatural looking discontinuities in their distributions ~6 km above radar level (ARL). The discontinuity features are especially apparent in Figure 1.7b,e.

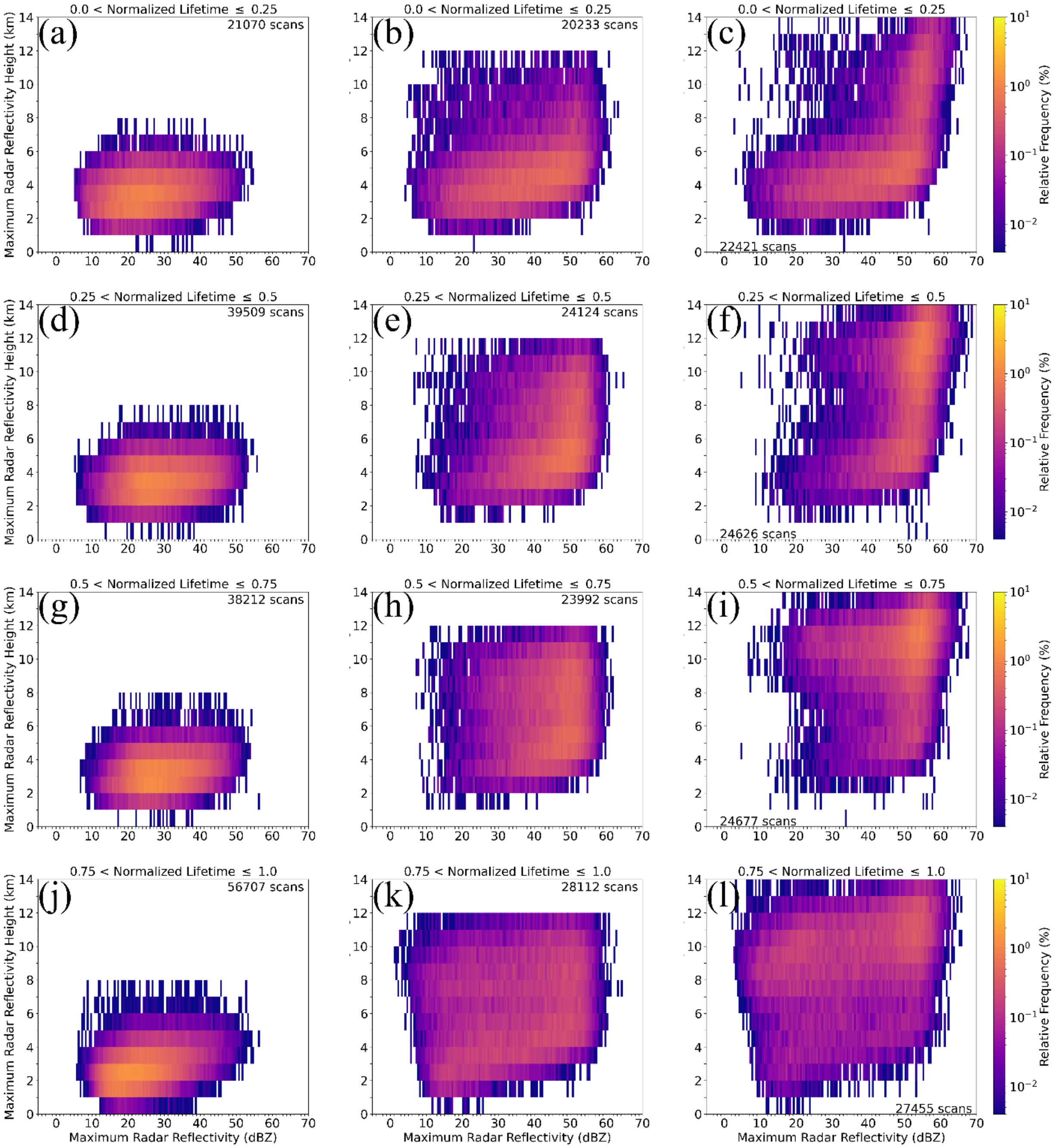

Figure 1.7: The distributions normalized by the number of scans considered for each cell lifetime segment of dBZ_{max} versus H_{dBZmax} for the first 25% (a, b, c), the second 25% (b, e, f), the third 25% (g, h, i), and the final 25% of cell lifetimes (j, k, l) for shallow (a, d, g, j), modest deep (b, e, h, i), and vigorous deep (c, f, i, l) convection.

Figure 1.8 supports that the feature seen in Figure 1.7 at ~6 km ARL is caused by the bright band, since there are no similar discontinuities in the distributions where GOESBT is warmer.

However, this is only one interpretation and the discontinuities shown in Figure 1.7 may rather be indicative of some other unobserved process unknown to us. As with Figure 1.7, Figure 1.8 clearly shows the initiation, growth, and decay of the cell types. Shallow convective cells remain at relatively warm GOESBT and low maximum VIL throughout their lives, whereas modest and vigorous deep convection show clear growth from warm GOESBT, low maximum VIL cells to cold GOESBT high maximum VIL cells. The rapid changes shown in Figs. 1.7 and 1.8 during the early stages of vigorous deep convective shows the quick vertical evolution of cells. Also shown in Fig. 1.7, is the dissipation phase, where GOESBT remains cold, but VIL drops off considerably. Such an evolution further supports the idea that this is the period when the convective cores have dissipated, leaving orphan anvils behind.

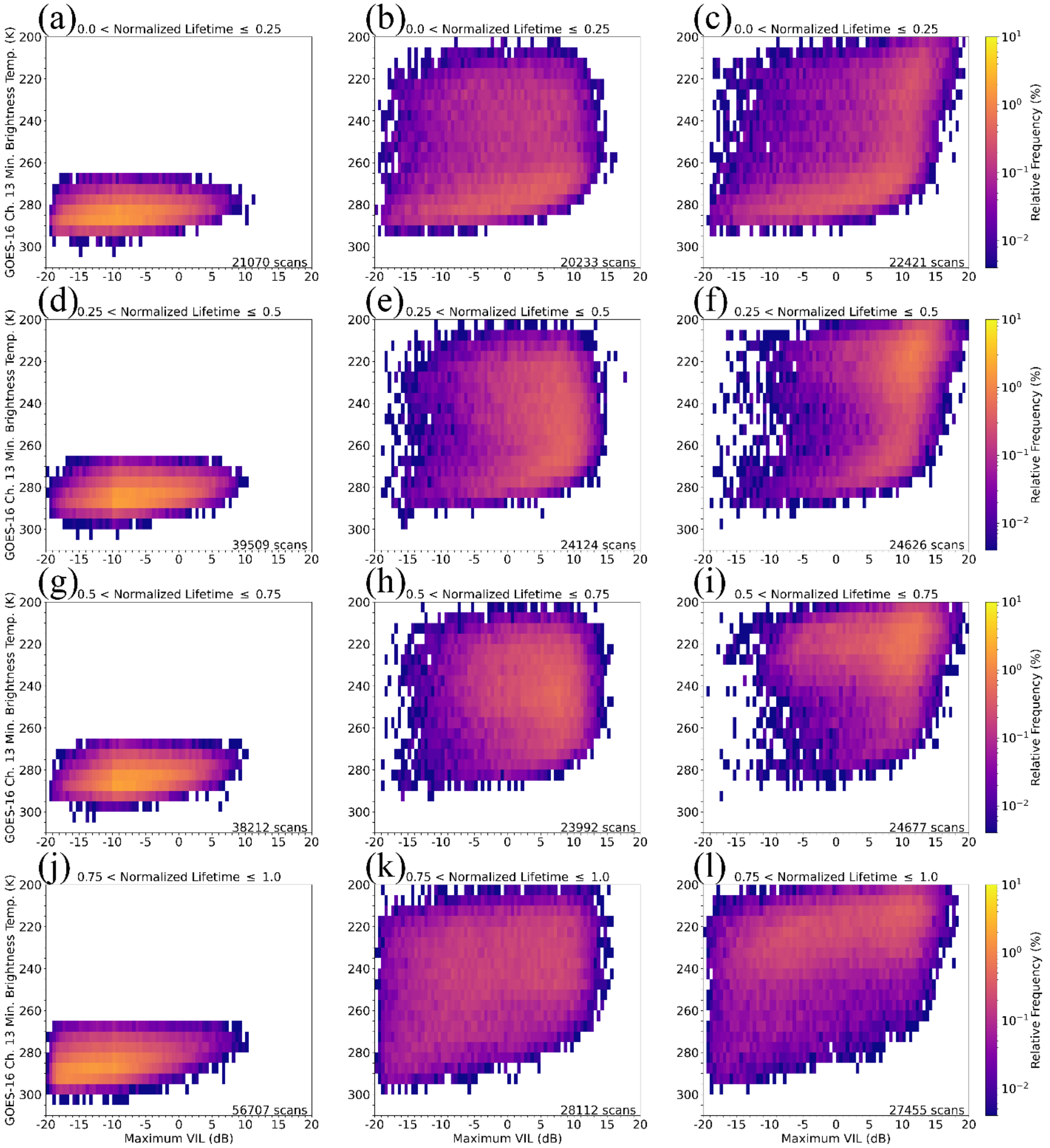

Figure 1.8: As in Fig. 1.7, but for maximum VIL versus GOESBT.

As stated previously, dBZ_{avg} is the average of the column Z_H maximums within a given cell and dBZ_{max} is the cell maximum Z_H for a given time. To investigate potential anvil generation, the distributions of dBZ_{avg} versus dBZ_{max} are analyzed (Fig. 1.9). During the anvil generation phase, we would expect cells to be at their most intense state, meaning they would have a high value of dBZ_{max}. We would also expect an increasingly large region of low Z_H high aloft in the storm to form. The region of low Z_H will skew dBZ_{avg} lower while dBZ_{max} will remain unaffected until the storm begins to dissipate. When comparing shallow and deep convection with this information in mind, the feature, apparent in deep convection, of low dBZ_{avg} and high dBZ_{max} could be interpreted as anvil generation. As with previous figures in this section, the anvil signatures are especially apparent in vigorous deep convective cells. Early in deep convective lifetimes, cells have not had enough time to grow to a state where anvil generation is possible (with the exception of the most intense cells). The vast majority of cells exist near the one-to-one line of dBZ_{avg} to dBZ_{max} with only a small subset of cells moving into the high dBZ_{max} and lower dBZ_{avg} indicative of cells growing and beginning to produce anvils (Fig. 1.9c). As cells move into the mature portion of their lifecycles, the low dBZ_{avg}/high dBZ_{max} region, where strong, anvil generating cells are present, becomes the dominant regime for them (Fig. 1.9f,i). As cells decay, the distribution maximum shifts back down near the one-to-one line (Fig. 1.9l), which would be suggestive of orphan anvils, given the analyses provided in the previous paragraphs. One feature of note in the vigorous deep convective cells during the dissipation phase is the secondary maximum in the high dBZ_{avg}/high dBZ_{max}. The secondary maximum represents the transition from the mature stage having the large dBZ_{max} in a deeper depth within the clouds to the later stage having lower dBZ_{max} during the normalized lifetime 0.75–1.0.

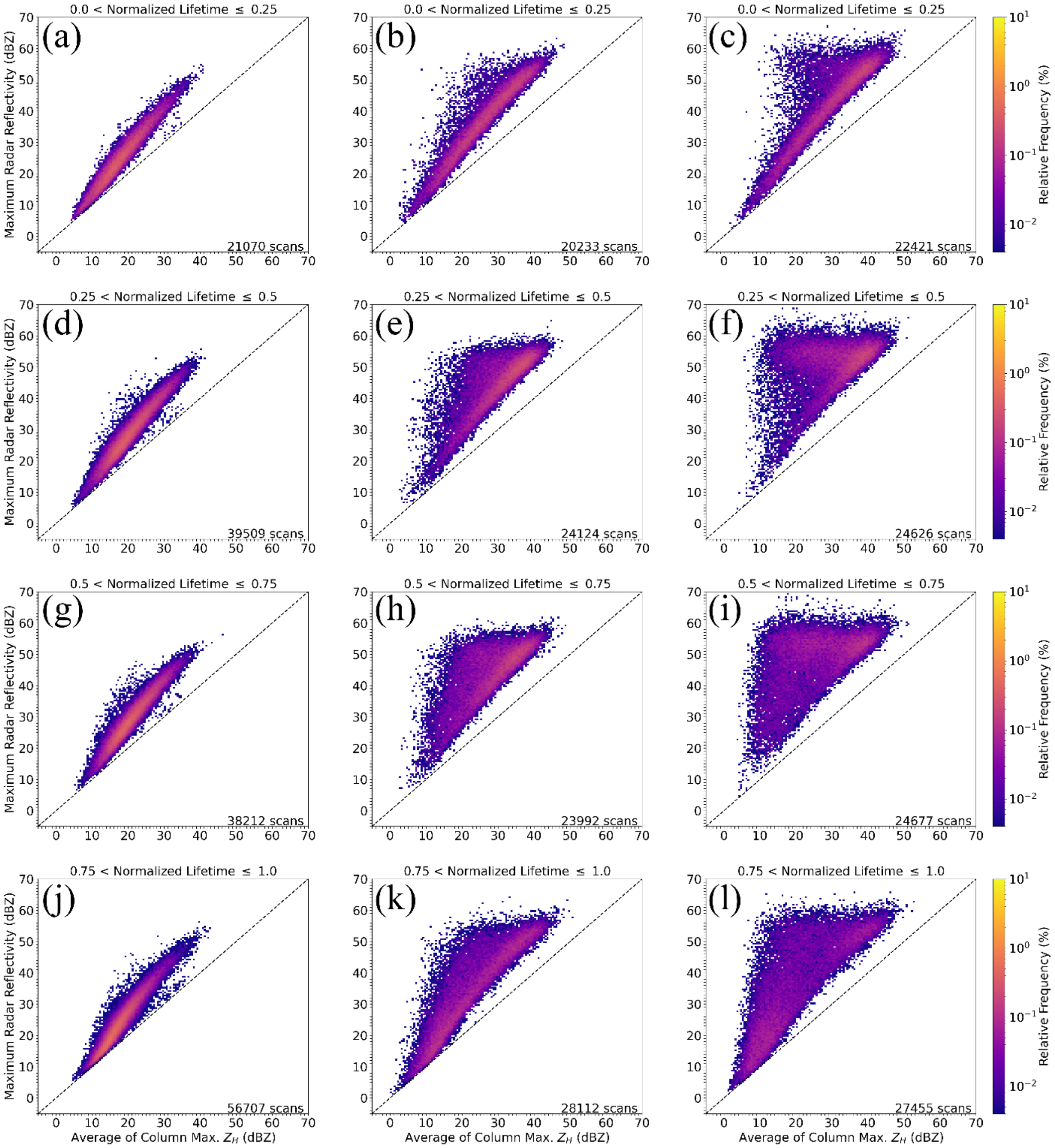

Figure 1.9: As in Fig. 1.7, but for dBZ_{avg} versus dBZ_{max}. The dashed line shows the one-to-one value of dBZ_{avg} and dBZ_{max}.

Shallow convective cells reach their maximum ETH during the first ~10% of their lifecycles, maintain this height until around 75%, and then gradually decrease in height until dissipation (Fig. 1.10a). Modest convective cells take substantially longer (~35-55% of the way through their lifecycles) to reach their maximum ETH and then sharply decrease in height during the last 15% (Fig. 1.10b). Vigorous convective cells, on the contrary, reach their maximum ETH quite quickly (within the first 15 to 35% of their life), maintain a tall echo top, and then gradually decrease in height to dissipation (Fig. 1.10c). The gradual decrease in ETH leading to dissipation is further indicative of convective anvils. In this case, we believe the ETH decrease further supports that we are observing convective core dissipation, thus leaving orphan anvils behind. Both H_{dBZmax} and dBZ_{max} show similar trends to ETH for all case types. Shallow convective cells reach their dBZ_{max} and H_{dBZmax} early in the cells' normalized lifetime (within the first 20-30%), maintain, and then gradually decay to dissipation (Fig. 1.10d,g). Modest convection shows a gradual increase in H_{dBZmax} that looks nearly identical to its maximum ETH; cells reach their H_{dBZmax} anywhere from 35 to 65% of the way through their lifetimes. However, dBZ_{max} is reached much earlier (within the first 20% of their lifecycle) than H_{dBZmax} (Fig. 1.10e,h). Vigorous deep convection reaches its H_{dBZmax} much sooner in its normalized lifetime (between 10 and 25% of their normalized lives), like ETH (Fig. 1.10f). As with modest deep convection, vigorous deep convection also reaches its dBZmax early in its lifecycle (within the first 20% of their normalized lifecycle) and maintains these values until about halfway through their lifecycles, when dissipation begins (Fig. 1.10i). One feature that is seen in dBZ_{max} and H_{dBZmax} for both modest and vigorous deep convection is the apparent bimodality later in cells lifecycles (>~0.4), when it appears that some cells maintain high values of dBZ_{max} and VIL (not shown) at the higher altitudes (~9 km) all the way up to dissipation (Fig. 1.10f,i). The bimodality is particularly apparent in the modest deep cells and is evidence that those with lower ETHs were dominated by warm phase precipitation processes similar to the shallow cells, as H_{dBZmax} was found below 6 km through the lifetime. However, we suspect that some of the bimodality in the late periods of modest and vigorous deep cell lifecycles is caused by cells being deemed “dissipated” despite continuing to persist for some time outside of the study domain. To mitigate the issue caused by cells that may enter or leave our domain while already ongoing, we removed cells that initiated or dissipated on the domain boundary. Despite the removal of cells that fit the outlined criteria, we still see bimodality in the deep convective distributions as seen in Fig. 1.10.

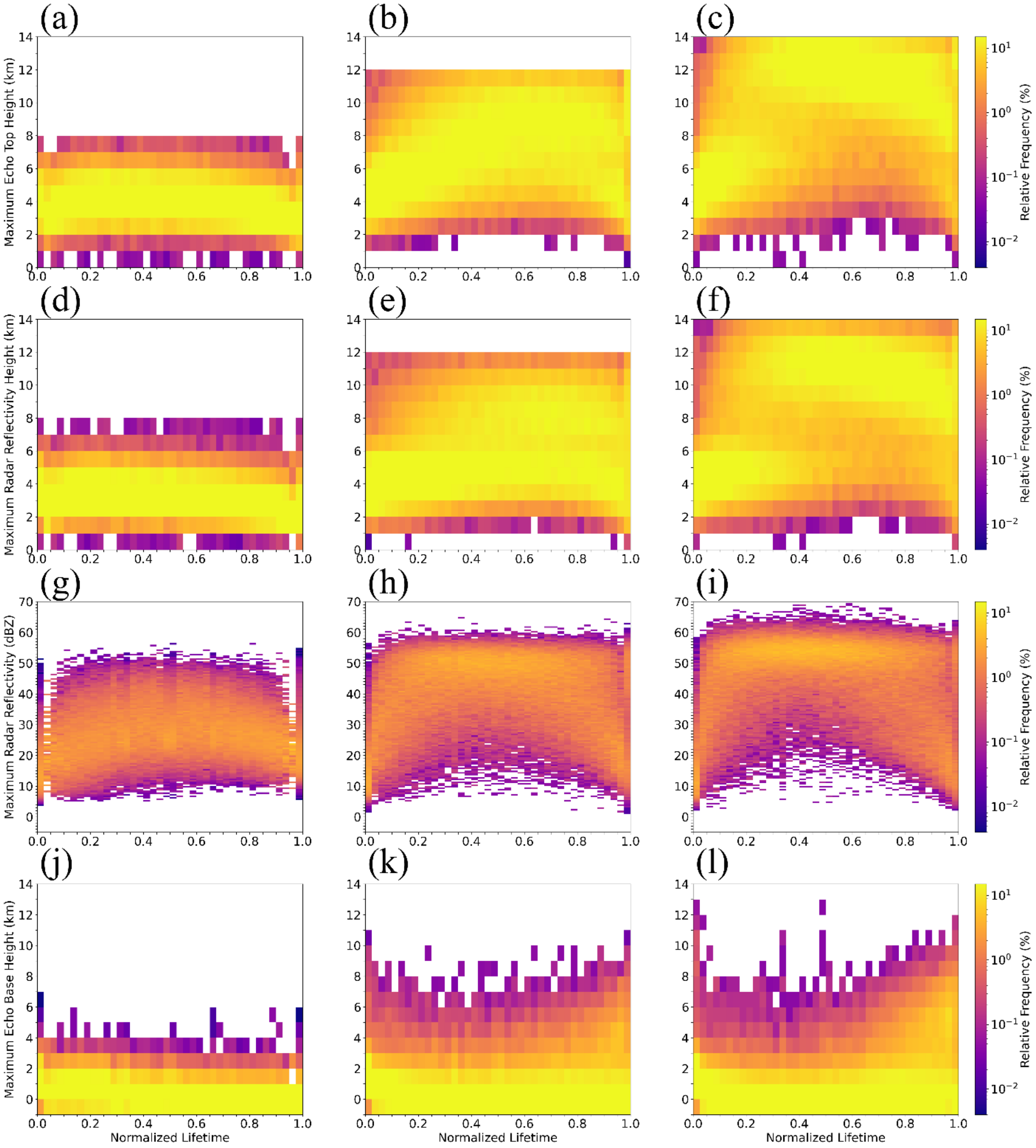

Figure 1.10: The bin normalized distributions for normalized lifetime evolutions of ETH (a, b, c), H_{dBZmax} (d, e, f), dBZ_{max} (g, h, i), and H_{EBase} (j, k, l) for shallow (a, d, g, j), modest deep (b, e, h, k), and vigorous deep (c, f, i, l) convection.

Cell echo base height (H_{EBase}) was determined using the maximum ETH minus the radar-derived echo profile depth to estimate the precipitation base of these cells. For shallow convection, H_{EBase} remains relatively flat for the duration of these cells, whereas it shows an increase in height during dissipation for modest and vigorous deep convective cells (Fig. 1.10j,k,l). This signature is especially apparent in the vigorous deep convective cells. This increase in H_{EBase}, in tandem with the minimal decrease in maximum ETH during dissipation of both types of deep convection (especially vigorous deep convection), reinforces the idea that we are observing the generation of orphan anvils. The bimodality here may also partially be caused by some cells leaving the domain during their mature phase, prior to dissipation despite the mitigation techniques we applied, but this is less certain than for the reasoning given for dBZ_{max}.

In an attempt to quantify vertical motion within vigorous deep convective cells, we approximated it three different ways. We used the maximum ETH, and H_{dBZmax} during each scan, and GOESBT at the time closest to radar scan time with the time between samples to calculate maximum ETH and H_{dBZmax} "ascent rates," as well as GOESBT "cloud top lapse rates." As shown in Figure 1.11, there are maximum ETH and H_{dBZmax} ascent signatures early and descent signatures late in the lives of these cells for all case types. GOESBT shows cooling during the same period where ascent is seen and warming during the same period where descent is seen in maximum ETH and H_{dBZmax}. The near identical timing and structure of derived ascent rates suggest that they may be good proxies for updraft intensity during the early parts of these cell. However, the later portions of these cells' lives are dominated by the tops or high upper portions of these features (Fig. 1.11) and most likely do not represent downdraft intensity during dissipation. We suspect that, in vigorous deep convective cases, we may be seeing orphan anvils falling out as virga since the descent signature occurs quite late in cells' normalized lifetimes after their H_{EBase} increases considerably. Maximum ETH and H_{dBZmax} descent rates and GOESBT warming rates match well late in these cells' lives, which further supports the idea that we may be observing anvil fall-out. Further analysis is necessary to validate the results presented herein. There is a hint of the anvil fall-out signature as well for modest deep convective cells, but it is not as obvious. To further assess the quality of these approximations, analyses outside the scope of this study will be needed. One caveat to consider with the presented ascent rate results is the increasing uncertainty in ETH and H_{dBZmax} with increasing range from KHGX. This uncertainty may account for the large spread always shown since we have large sample sizes for all case types. The large uncertainty for cells in the farthest portions of our domain muddle the results considerably. However, since the same signal is seen when looking at the GOESBT cloud top lapse rates, more credence is led to the above analyses.

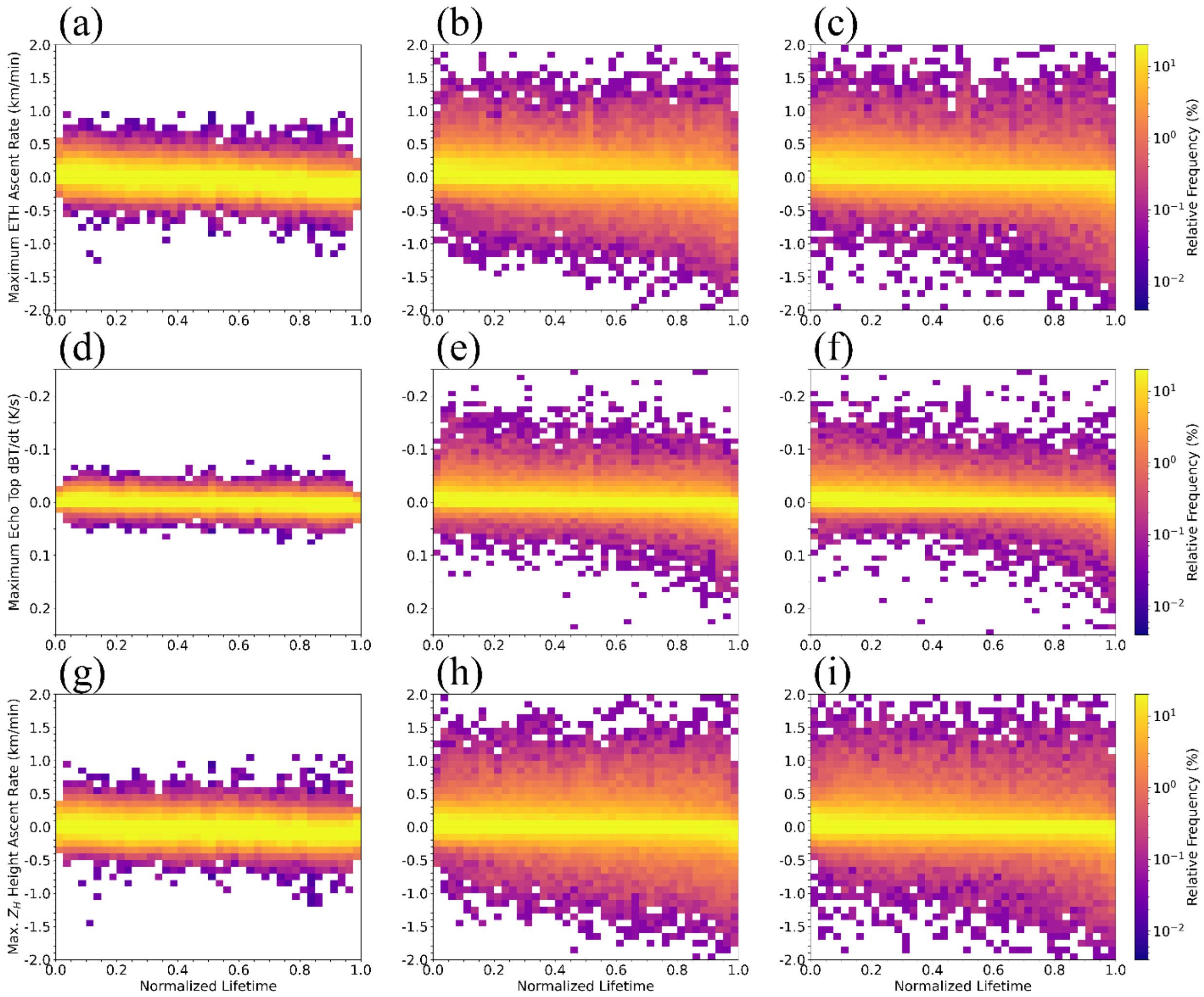

Figure 1.11: The bin normalized ETH (a, b, c), GOESBT (d, e, f), and H_{dBZmax} (g, h, i) based ascent rates for shallow (a, d, g), modest deep (b, e, h), and vigorous deep (c, f, i) convection. The dashed line denotes the zero-change line.

1.3.5 Near Storm Environment and Aerosol Effect Analyses

To elucidate any effects from the local meteorology where cells formed, HRRR data for the hour directly preceding cell initiation are extracted for the grid point where initiation occurs. The surface-based environment does not appear to play a role in differentiating whether cells become shallow or deep convective cells. All convective types initiated in environments where surface-based CAPE and CIN are similar overall. Storm relative helicity (SRH) and bulk shear are also similar overall. Deep convective cases formed in environments with slightly higher 0-1 km

SRH, but the distributions of 0-1 km and 0-3 km SRH, as well as 0-6 km bulk shear are similar (not shown).

When observing the composite soundings for the initiation locations for all convective case types, the temperature profiles and parcel paths are also nearly identical. Dew point, however, is drier by approximately 5ºC in the mid-to-upper levels for the initiation locations of shallow convective cells when compared to deep convective cells (Fig. 1.12). While there is substantial spread in the moisture profile in all case types, modest and vigorous deep convection moisture profiles appear essentially the same. The wind profiles also appear relatively similar between case types. Surface winds are slightly backed and veer with height to about 850 hPa, where they begin to back again (especially in shallow convective cases.) However, the magnitude of the differences in mean wind are quite small (on the order of 5 kts between 850 hPa and 600 hPa.) There are also apparent differences in upper-level winds, but again, are quite small in magnitude.

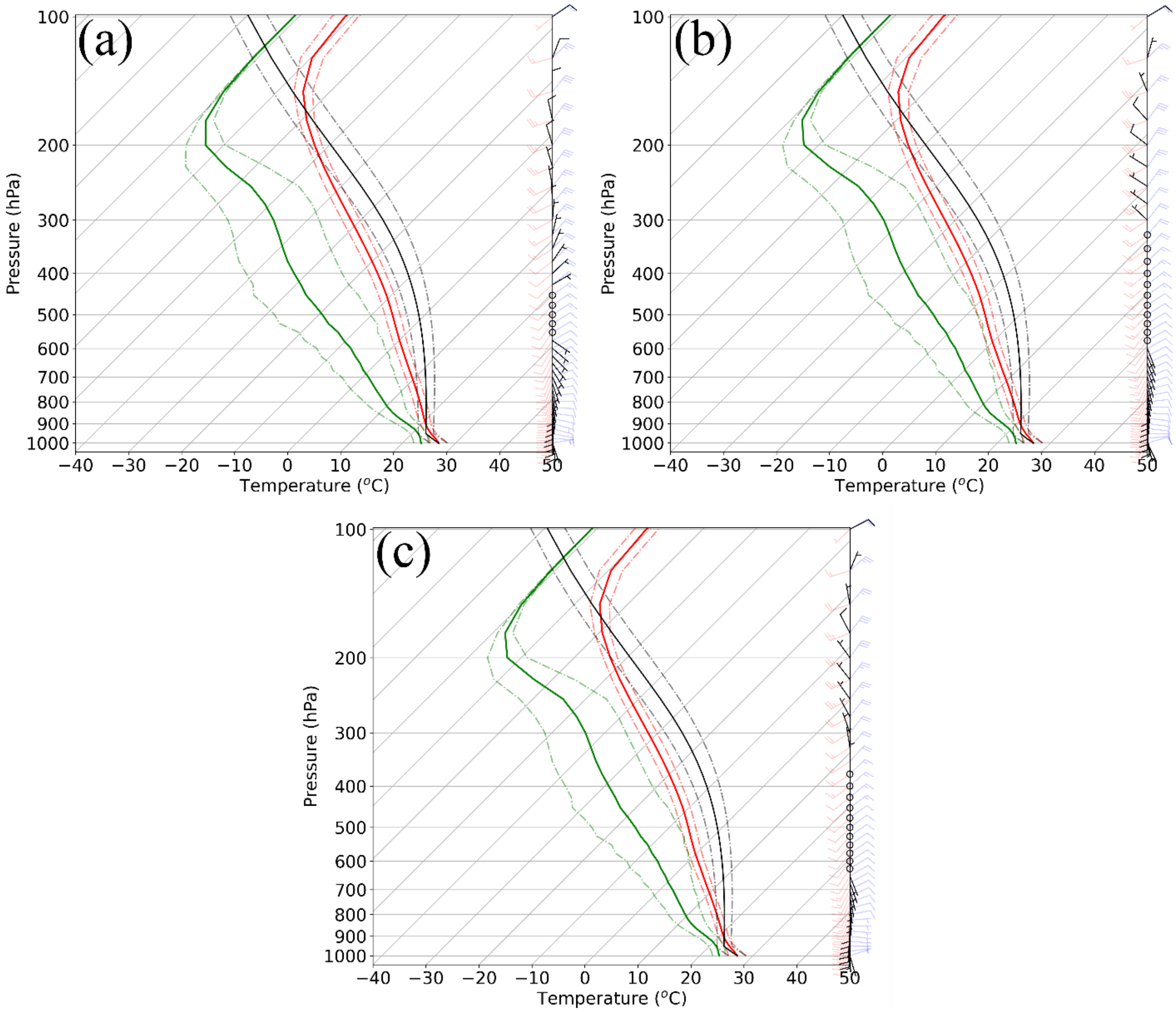

Figure 1.12: Composite HRRR soundings for the initiation location of shallow (a), modest deep (b), and vigorous deep (c) convection. The red, green, and black solid (dot-dashed) lines represent the mean (± one standard deviation) of temperature, dew point, and parcel path respectively. Black, red, and blue wind barbs represent the mean, plus one, and minus one standard deviation in knots.

In order to further parse out any differences in initiation environment, we select case days where the number of cells that initiated on a given day, for a given case type, surpassed the 95th percentile of daily cell initiation (273, 61, and 43 cells for shallow, modest deep, and vigorous deep convective cells respectively). The composite soundings for the initiation locations of the cell type that surpassed the 95th percentile of daily cell counts are shown in Figure 1.13. As with the soundings from Figure 1.12, the key difference between case types is that shallow convective initiation locations tend to have drier mid-to-upper-level dew points. Near surface winds are nearly the same with some apparent differences in mid and upper-level winds.

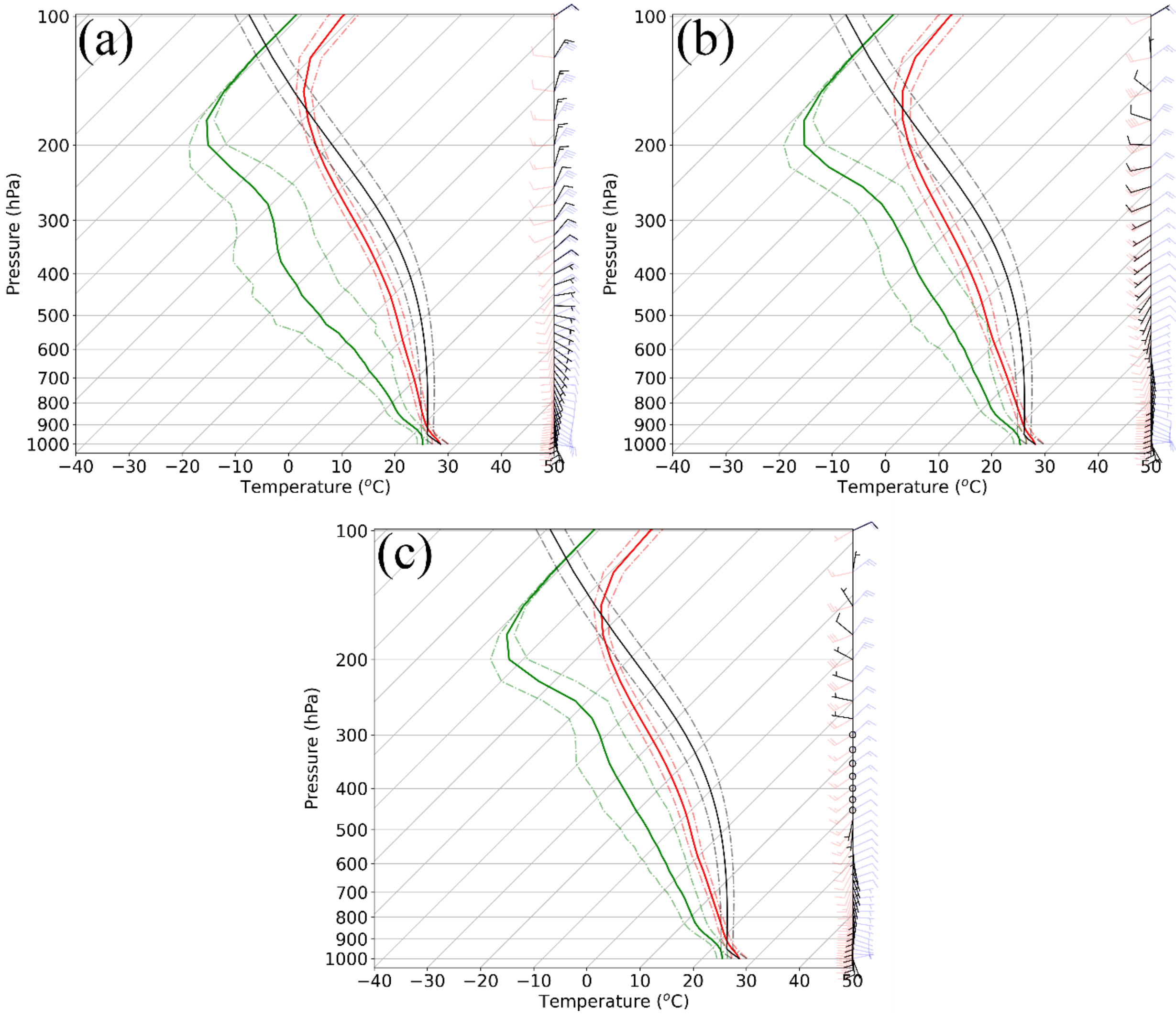

Figure 1.13: As in Fig. 1.12, but for days where the 95th percentile of daily cell count was surpassed for each case type.

Previously, we noted the discrepancy in initiation location of shallow convective cells that did not appear to be affecting deep convection. There is either some form of enhancement occurring to the southwest of the Houston metropolitan area or some form of suppression occurring to the northeast. One potential cause for this discrepancy could be the local meteorology in which these cells form. On days where shallow convective cells surpassed the 95th percentile of daily shallow convective cell initiations, we subdivided the domain to isolate the region to the southwest and northeast of Houston (Fig. 1.14a,b). The composite soundings for shallow convective cell initiation locations within our sub-domains are shown in Figures 1.14c and 1.14d. While the moisture profile to the southwest of Houston is marginally drier in the mid-to-upper levels, the composite soundings are essentially identical. One interpretation of the discrepancy between mid-to-upper level moisture is that drier air aloft tends to inhibit convective updrafts from growing into deep convection. The entrainment of drier air aloft would cause more evaporative cooling at the cloud top than a moister environment, leading to more negative buoyancy, and therefore limiting updraft intensity.

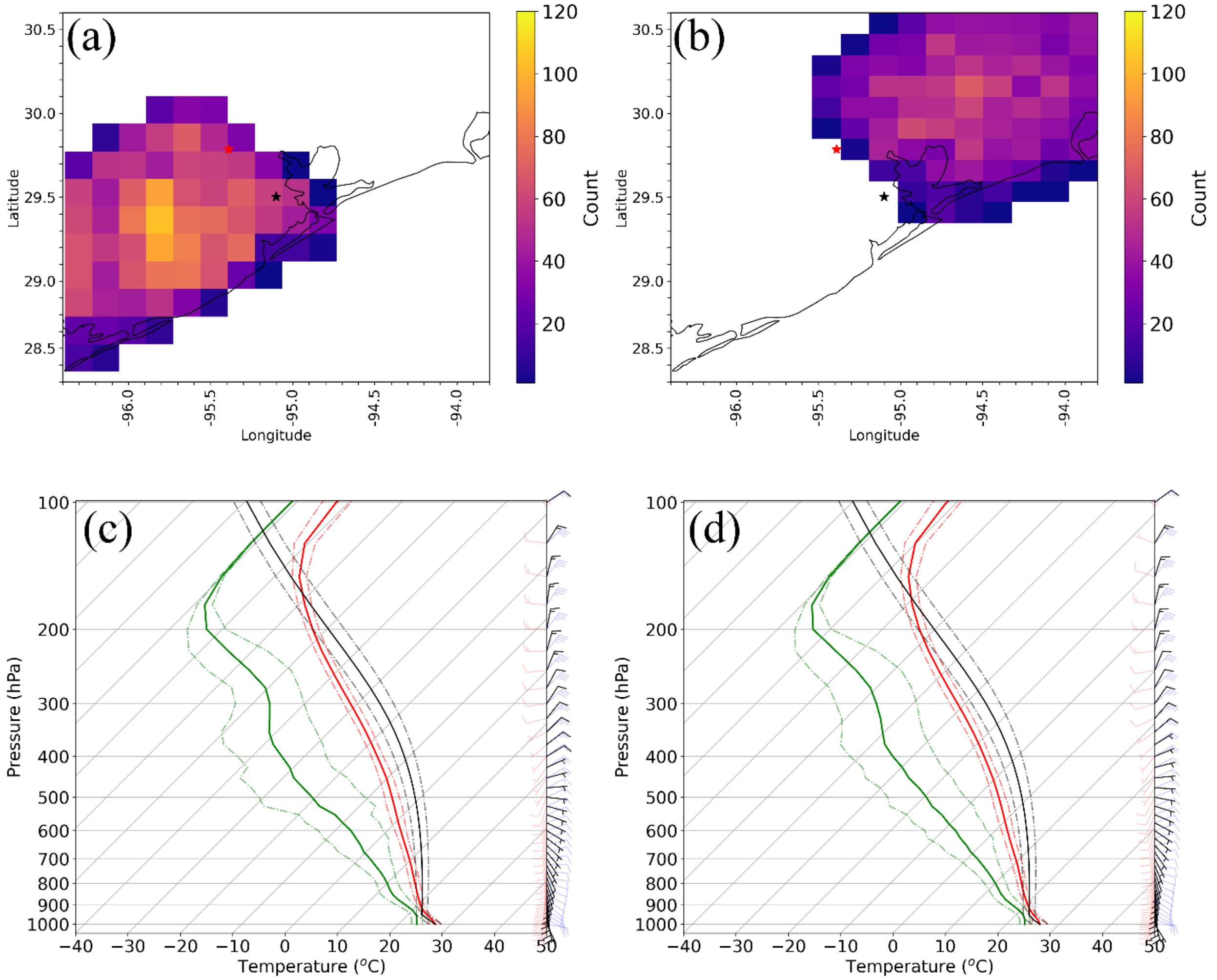

Figure 1.14: Subsets of the initiation locations for shallow convection to (a) the southwest and (b) the northeast of Houston on days where the 95th percentile of daily shallow convective cell counts was surpassed and the composite soundings for cells that initiated to the southwest (c) and northeast (d) of Houston. Sounding plot depictions are as in Fig. 1.12.

To compare with modest and vigorous deep convection, we computed the total number of cells that formed within each sub-domain and for both sub-domains combined, then normalized them by the area of each domain. For shallow convection, the southwest domain had a cell initiation of 0.2074 cells km^{-2}, the northeast domain had a cell initiation of 0.1764 cells km^{-2}, and the combined southwest and northeast domain showed a total of 0.1920 cells km^{-2}. Modest deep convective cells had a cell initiation of 0.0389 cells km^{-2} to the southwest, 0.0358 cells km^{-2} to the northeast, and 0.0373 cells km^{-2} combined. Vigorous deep convective cells had a cell initiation of 0.0331 cells km^{-2} to the southwest, 0.0265 cells km^{-2} to the northeast, and 0.0298 cells km^{-2} combined. Overall, more cells initiated in the southwest area than the northeast area. Area-normalized initiation counts show that there may be some slight differences in deep CI between the areas to the southwest and northeast of Houston. The area-normalized cell initiation results combined with the near identical soundings for shallow convection suggest that something other than local meteorology is affecting shallow CI.

One potential ingredient that may influence CI and has been a key point of debate in recent literature is aerosol loading. Aerosol particles in our study region range from natural particles, such as sea spray, to industrial pollutants from oil refineries and urban sources. However, no such dataset exists which is tracks individual aerosol species on the spatiotemporal scale needed for direct comparison with MCIT output. As such, we used temporal averages of GOES-16 AOD at the locations of cell initiation for the 30 minutes prior to MCIT detected initiation. We analyzed these data for regions to the southwest and northeast of Houston; the same as Fig. 1.14a,b. The analyses of AOD for shallow and modest deep (Fig. 1.15a,b) cells at the locations of their initiation show essentially identical distributions from southwest to northeast; the primary difference being that both shallow and modest deep cells exhibit a longer tail toward higher AOD values to the southwest. Median (mean) AOD for shallow convective cell initiation locations were 0.338 (0.400) to the southwest and 0.335 (0.366) to the northeast, and 0.366 (0.453) to the southwest and 0.346 (0.384) to the northeast for modest deep convection. Considering the substantial difference in initiation location for shallow convection and nearly identical initiation AOD distributions, we interpret that bulk AOD does not play an important role in controlling cell initiation. However, the lack of an obvious relationship between initiation location and bulk AOD does not mean that aerosol particles play no role as a control on cell initiation. Rather, it may be specific species of aerosol particles that are more or less important to convective processes. Vigorous deep convective cells, however, do show differing distributions from southwest to northeast (Fig. 1.15c). As with shallow and modest deep convection, vigorous deep convection also exhibits a longer tail extending to higher values of AOD to the southwest. The initiation locations for vigorous deep convective cells tend to have marginally higher AOD values to the southwest. The median (mean) of the AOD distributions for vigorous deep convective cell initiation locations was 0.428 (0.513) to the southwest and 0.373 (0.396) to the northeast. However, the differences in distributions are not statistically significant. From the previous area-normalized cell initiation, we speculate that the marginally higher values of AOD and rates of cell initiation to the southwest in vigorous deep convection suggest that aerosol loading may indeed factor into vigorous deep CI, but that more marginal convective cells are either more dependent on specific species of aerosol particles rather than overall aerosol loading or are not as affected by aerosol loading overall.

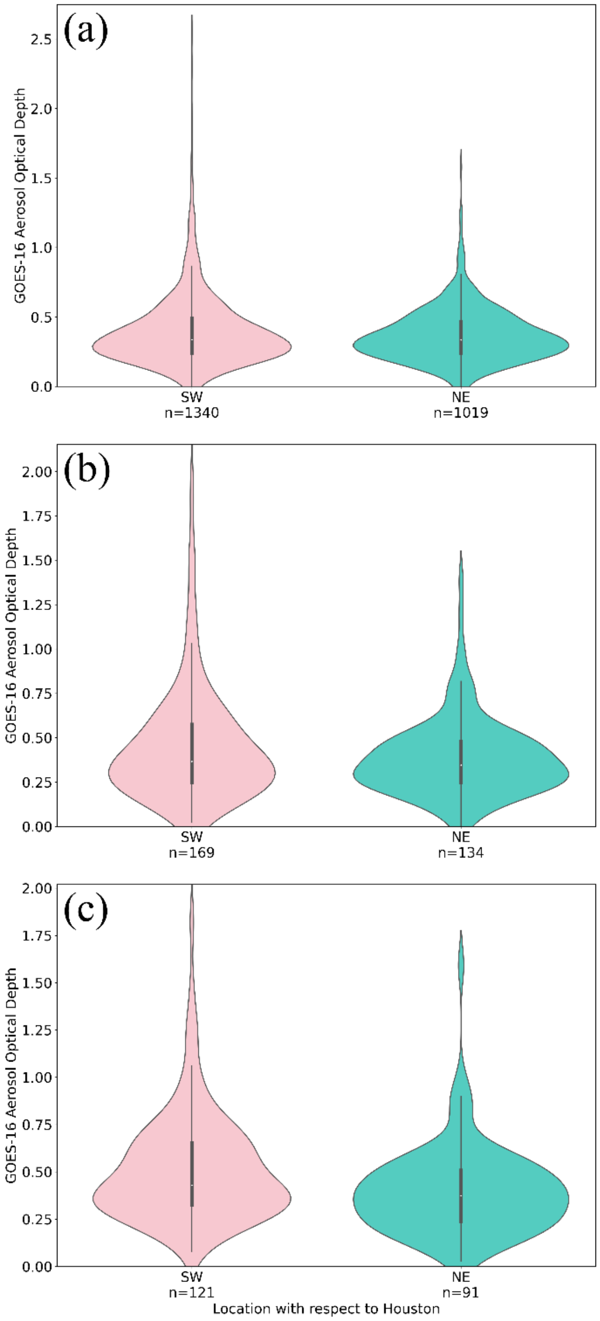

Figure 1.15: Violin plots depicting the distributions of the average of the 30-minute AOD values for the period prior to cell initiation to the southwest (red; same region as Fig. 1.14a) and northeast (blue; same region as Fig. 1.14b) of Houston for (a) shallow, (b) modest deep, and (c) vigorous deep convective cells. The number n under each violin plot corresponds to the number of cells considered for each distribution.

1.3.6 Threshold Sensitivity Analysis

To assess the sensitivity of the results in this study, the thresholds were varied individually and simultaneously by ±5% from the values presented in Table 1.1. The number of cells selected in each sensitivity test were recorded and plots were qualitatively analyzed to investigate substantial differences as these variables were adjusted. Table 1.2 shows the number of cells selected for each variable adjusted. Figure 1.16 shows the visual differences of the distributions based on changes in the most sensitive thresholds.

Shallow Convection				
	-5%		+5%	
	n	% change	n	% change
All Thresholds Simultaneously	41689	15.82	17855	-50.40
Lifetime Max. Area	35018	-2.72	36851	2.38
Lifetime Min. GOESBT	42038	16.79	18369	-48.97
Lifetime Max. ERatio	36047	0.14	35911	-0.24
Lifetime Max. ETH	35845	-0.42	36090	0.26
Lifetime Max. VIL	36906	2.53	35055	-2.61
Modest Deep Convection				
	-5%		+5%	
	n	% change	n	% change
All Thresholds Simultaneously	4993	-37.08	10168	28.14
Lifetime Min. GOESBT	5774	-27.23	9871	24.40
Lifetime Max. ERatio	7956	0.26	7906	-0.37
Lifetime Max. ETH (Lower Bound)	8566	7.95	7312	-7.85

Lifetime Max. ETH (Upper Bound)	6526	-17.76	9247	16.53
Lifetime Max. VIL	7990	0.69	7879	-0.71
Vigorous Deep Convection				
	-5%		+5%	
	n	% change	n	% change
All Thresholds Simultaneously	5933	21.85	3599	-26.08
Lifetime Min. GOESBT	4684	-3.80	4975	2.18
Lifetime Max. ERatio	4873	0.08	4863	-0.12
Lifetime Max. ETH	6278	28.94	3557	-26.95
Lifetime Max. VIL	4877	0.16	4862	-0.14

Table 1.2: A table showing the sensitivity of cell selection based on ±5% adjustments of a given variable. The number n represents the number of cells selected after the threshold adjustments were applied. Values for the percent change in the number of cells selected colored in green, yellow, and red denote cells with percent changes ≤ ±10%, ≤ ±20% and > ±20% respectively.

The number of shallow convective cases varied more for lifetime minimum GOESBT than any other variable. The number of cases increased by 16.79% for a five percent reduction in the GOESBT threshold (from 268.0 K to 254.6 K) and decreased by 48.97% for a five percent increase in the same threshold (from 268.0 K to 281.4 K). The visual differences in the distributions of cases are shown in Figure 1.16a,b,c. As shown, the visual differences in the distributions are caused by the addition or removal of colder topped shallow convection (Fig. 1.16c). The overall shape of the distribution does not change otherwise. Increasing GOESBT only removes the more "intense" shallow convective cells that have colder GOESBT values during their lifetimes.

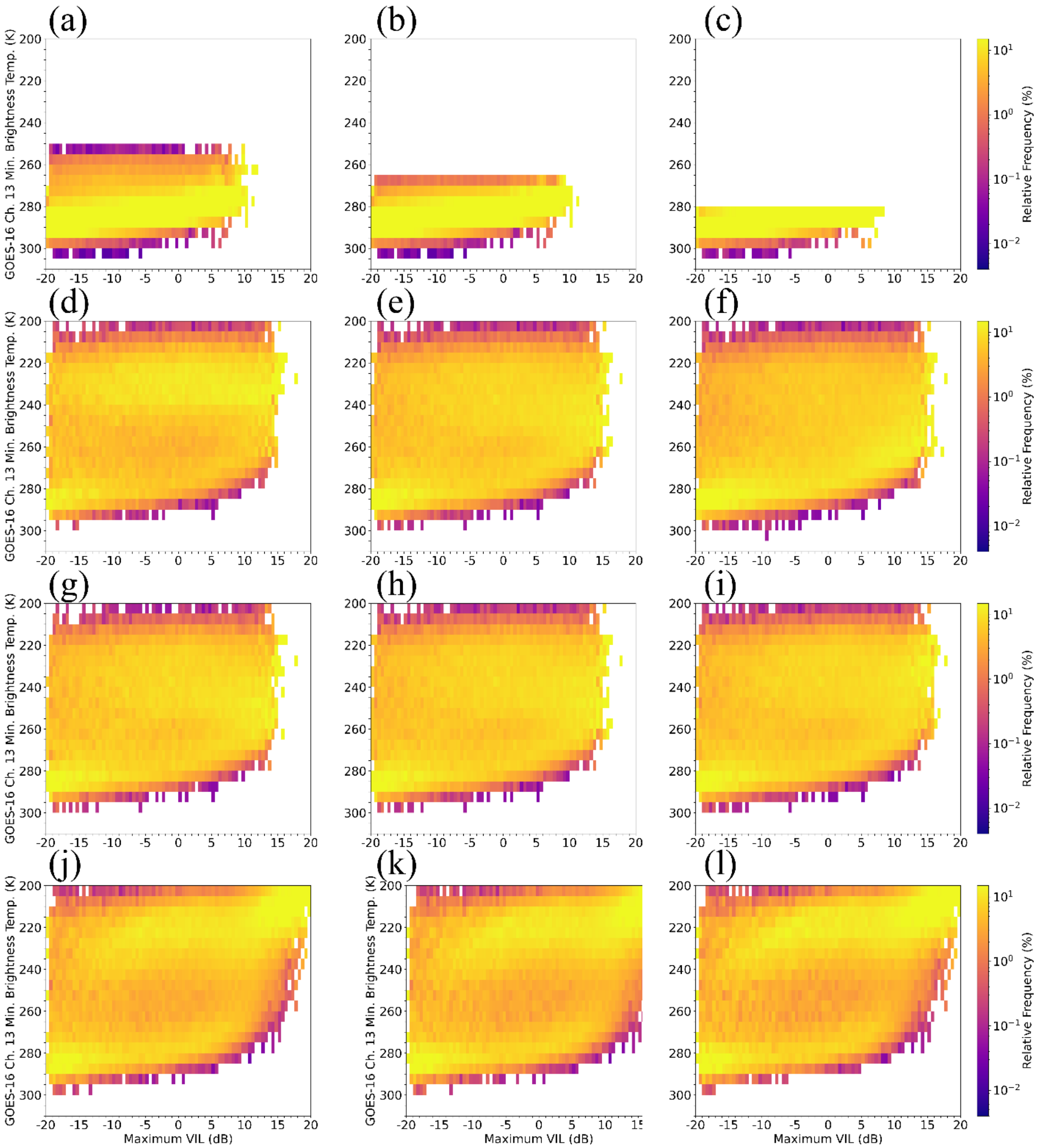

Figure 1.16: The lifetime distributions of GOESBT versus maximum VIL to illustrate threshold sensitivity for the most highly sensitive variables shown in Table 1.1. The baseline (no change) distributions are shown in (a, d, g, j), 5% decrease is shown in (b, e, h, k) and 5% increase is shown in (c, f, i, l) for shallow convection GOESBT sensitivity (a,b,c), modest deep convection GOESBT sensitivity (d, e, f), modest deep convection upper bound ERatio sensitivity (g, h, i) and vigorous deep convection ETH sensitivity (j, k, l).

Like the shallow convective cases, the number of modest deep convection cases varied most with changes in lifetime minimum GOESBT. There was a 27.23% reduction in cases with a five percent decrease in GOESBT (250.0 K to 237.5 K). A colder GOESBT threshold removes the cells with warmer cloud tops, leaving an upper bound of more intense modest deep convective cases (Fig. 1.16e). There was also a 24.40% increase in cases with a five percent increase in lifetime minimum GOESBT (250.0 K to 262.5 K). The addition of warmer, lower intensity convective cells is clearly shown (Fig. 1.16f). The modest convective cells also varied by more than 10% for the upper bound of the lifetime maximum ETH, but there were no visible changes in distributions of these variable, only a reduction/increase in the number of cases (Fig. 1.16g,h,i).

Vigorous convection varied most by lifetime maximum ETH. The number of cases increased by 28.94% for a five percent decrease in maximum ETH (12 km to 11.4 km) and decreased by 26.95% for a five percent increase in maximum ETH (12 km to 12.6 km). The variability in maximum ETH is shown in Figure 1.16j,k,l and behaves similarly to how the sensitivity in maximum ETH affects modest deep convection. Adjusting the ETH threshold only appears to reduce or increase the number of cases and not change the shape of the distribution.

1.4 Summary and Discussion

The climatological characteristics of convective cell evolution and their diurnal cycles were analyzed using the NWS KHGX WSR-88D from Houston, Texas for the warm season months (June to September) from 2018 and 2021 and a modified version of the MCIT algorithm. In total, our study analyzed 48,800 convective cells (35,995 shallow cells for 142,923 volume scans, 7,935 modest deep cells for 92,798 volume scans, and 4,869 vigorous deep cells for 95,219 volume scans). Analysis of the presented case types together allowed for the direct comparison of cell characteristics and the environments in which they formed. The key findings from the study are:

1. CI for all cell types occurs most frequently in the late morning/early afternoon over land, consistent with the inland incursion of the sea breeze front.
2. There is a spatial variability in CI for shallow, modest, and vigorous deep convective cells, suggesting some effects of aerosol loading and/or urban heating. The spatial variability in CI is particularly clear for shallow cells where cells appear to preferentially initiate to the southwest of Houston. Higher AOD values tend to be present to the southwest of Houston, which is most easily observed when looking at the vigorous deep CI AOD distributions. While not statistically significant, the regional differences in AOD suggest that aerosol loading may have some effect on deep CI. The initiation biases do not appear to be related to overall aerosol loading based on the pre-CI AOD analysis with the exception of vigorous deep cells. Further analysis using high spatiotemporal aerosol and urban heat data will be needed.
3. The CI location bias for shallow cells was coincident with slightly drier mid-to-upper-level moisture to the southwest of Houston, based on the HRRR reanalysis

data. The deep convection categories do not appear to be related to the local meteorology at the point of initiation based on the HRRR reanalysis data. The surface-based CAPE and CIN do not show significant relations with CI.

4. The modest and vigorous deep convective cells particularly deepen in the afternoon/evening (12:00-21:00 CDT) as the frequency peak of their heights of maximum reflectivity increase to 11 km and that of the brightness temperature decrease to 220 K. The shallow cells do not have clear diurnal variability in those parameters and remain relatively consistent throughout the observed time.
5. The cell evolution is well represented by relationships between the following cell properties:
    1) The height and value of the maximum radar reflectivity: The developing stage (cell lifetime normalized by cell duration < 0.75) is well represented by an exponential curve as the H_{dBZmax} gradually increases from around 2 to 4 km with a maximum reflectivity of ~50 dBZ, which then dramatically increases to a height of 12 km for dBZ_{max} values of 50-60 dBZ. The coincident increases in dBZ_{max} and H_{dBZmax} occur in the early stage of cell lifetime (normalized lifetime < 0.5). The dissipation stage is represented by a wide distribution of the maximum reflectivity at a high altitude (~10 km) suggesting anvil development and convective core dissipation.
    2) The brightness temperature (hence echo top height) and the maximum VIL: The developing stage (normalized lifetime < 0.75) is well represented by an exponential curve as the brightness temperature gradually decreases from

290 to 260 K from the maximum VIL until 10 dB then dramatically decreases to 210 K for VIL > 10 dB.

3) The maximum reflectivity and columnar average reflectivity: As the cells begin to develop for all case types, these two variables remain near the one-to-one line. However, as deep convective cells (especially vigorous deep convective cells) reach the middle phases of their lifecycles (0.25 < normalized lifetime ≤ 0.75), an obvious extension of high dBZ_{max}/low dBZ_{avg} becomes apparent. The extension of the distribution during this period further supports the development of anvils. In the remaining 25% of vigorous deep convective cell lifetimes, the distribution of dBZ_{max}/dBZ_{avg} shifts to low values for both, suggesting convective core dissipation leaving only orphan anvils behind.

6. The ETH ascent rate is slightly more positive (0.3 km/min) in the early stage (normalized lifetime < 0.4) and negative for the later stage (normalized lifetime > 0.8) for deep convective cells. Early in these cells' lives, the cell tops grow vertically as they intensify and the rates at which they ascent should be close to the actual updraft intensity. Late in the cells' lives, H_{dBZmax} remains high aloft as it appears that H_{dBZmax} remains in the anvil portion of the storm after it reaches maturity. These descent rates are likely to be representative of orphan anvils falling out as virga.

Based on the findings in our study, the analysis techniques presented can identify individual features within convective cells. Further parsing of MCIT output data may allow for the tracking of individual features within cells, such as tracking cores and anvils separately and being able to analyze their behaviors over their lives. Polarimetric variables can also be added, as in Hu et al. (2019a,b), for automated tracking of features such as differential reflectivity columns and arcs. The convective cells considered in here only constitute about 3% of the features tracked during the climatology period and were selected based on the empirically derived thresholds in Table 1. Some of the features we excluded by using the outlined thresholds are non-meteorological in nature, but others include high clouds and large precipitation shields. Different empirically derived thresholds can be developed to isolate those and other features from the full dataset and used to create large climatologies of various features of interest. A parallax displacement was not corrected in the present analysis. The parallax correction should be applied in combination with analyses of satellite and ground-based radar data in future works to obtain better estimates of the relationship between the satellite and ground-based radar data. The analysis techniques presented herein can also be applied to the cloud resolving model simulations using radar simulator and cell tracking techniques (e.g., Oue et al. 2022). Studies utilizing cloud resolving models with radar simulators will aid in better evaluating simulation results to understand isolated convective cell formation and evolution mechanisms, including effects of environmental factors such as aerosols that observational data alone cannot address. Some mechanisms that may affect CI have been discussed here, such as aerosol loading and urban heating, but have not been explored in-depth. Such mechanisms may be of considerable importance in determining what processes are most crucial to convective growth, maintenance, and decay.

Chapter 2

Bulk Analysis of Radar-Derived Mesocyclone Intensity and Transience Preceding Supercell Tornadogenesis and Tornadogenesis Failure

2.1 Introduction

Another unsettled research question with respect to convection, substantially different from the questions outlined in Chapter 1, but still one that would benefit greatly from climatological analyses, involves supercell tornadogenesis. A complete understanding of the processes leading to supercell tornadogenesis (“G”) (or its failure (“F”)) remain a relative mystery in many aspects. Previous observational studies have investigated contributions from the surface and near-surface thermodynamics (e.g., Markowski et al. 2002; Grzych et al. 2007), the low-level microphysics (e.g., Kumjian and Ryzhkov 2008; Kumjian 2011; French et al. 2015; Tuftedal et al. 2021 (T21 hereafter)), and the low-level kinematics (e.g., Trapp 1999; Trapp et al. 2005; Kingfield and LaDue 2015; Sessa and Trapp 2020; Peters et al. 2023) in supercells. All of the above are likely to have some influence on tornado production and peak intensity, but the plethora of processes involved in the production and maintenance of tornadoes drastically complicates direct attribution to one characteristic over another.

One part of the tornadogenesis process that has received relatively little *observational* attention: the development and maintenance of low-level mesocyclones (LLMs). Arguably, the defining feature of a supercell is its cyclonically rotating updraft, the midlevel (i.e., 3–6 km above ground level (AGL)) mesocyclone (Doswell and Burgess 1993). The midlevel mesocyclone is known to form owing to the tilting and stretching of horizontal vorticity generated through ingestion of air with sufficient amounts of vertical wind shear and streamwise vorticity (Davies-Jones 1984). However, for tornadogenesis to occur, rotation is needed near the surface in addition to storm midlevels. A key intermediate step in the production of a tornado is the development of a *low-level* (i.e., 1–3 km AGL) mesocyclone (e.g., Wicker and Wilhelmson 1995; Trapp et al. 2005). It is thought that additional processes, namely the baroclinic generation of horizontal vorticity owing to the presence of buoyancy gradients, are needed to generate rotation for a LLM (e.g., Rotunno and Klemp 1985; Straka et al. 2007; Markowski et al. 2008; Dahl et al. 2014). However, Peters et al. (2023) recently suggested that barotropic vorticity from the environment may be a large contributor to LLM intensity. Roberts and Xue 2017 also found large barotropic contributions to LLM vorticity, but only when frictional effects were applied to the environmental background wind only and not the full wind. Their environmental wind only simulation failed to produce an intense LLM when compared to the full wind experiment. From there, regardless of vorticity source, strong dynamic lifting partially induced by low-level rotation (Markowski and Richardson 2014) and attendant low-level convergence may act to further stretch vertical vorticity to tornadic levels. Given the aforementioned processes, to go from the penultimate to final step is not an instantaneous process. *Therefore, it stands to reason that the duration over which low-level rotation is present and dynamically-driven updrafts are supported may also be important for tornado formation.*

Kinematic characteristics and changes at low levels in tornadic supercells are a common tornado research topic. For instance, Trapp (2005) analyzed WSR-88D data with the mesocyclone detection algorithm to assess the prevalence of mesocyclones associated with tornadoes. They found that the lower the level of mesocyclone detection, the higher the probability of that mesocyclone being associated with a tornado (i.e., only 15% of their "midaltitude" mesocyclones were tornadic, but 46% of mesocyclones detected at or below 250 m ARL were tornadic). However, they did not assess the intensity of these mesocyclones, nor did they assess how that intensity changed over the periods approaching tornadogenesis or tornadogenesis failure. They also did not attempt to make any distinction between the characteristics of tornadic and non-tornadic mesocyclone characteristics.

Markowski et al. (2011) investigated the full three-dimensional wind fields of three non-tornadic supercells from Doppler on Wheels mobile radars to assess LLM characteristics. Their findings showed that, from the three cases considered, air parcels which passed through the LLM did not rise as high as has been seen in tornadic cases in other studies. The LLMs studied also tended to have overall weaker circulations. However, they mention that using only three non-tornadic cases prevents generalization. Their study suggests that there may be inherent differences in tornadic and non-tornadic LLMs and differences in their vertical perturbation pressure gradient force (VPPGF) owing to the lack of vertical displacement of the air parcels which enter the LLM.

Highly idealized simulations of supercell tornadogenesis were performed in Fischer and Dahl (2020), using Cloud Model 1 (CM1) to identify the effects of low-level updraft and cold pool characteristics on tornadogenesis. Their study showed that, while both characteristics analyzed are active contributors to tornado potential. A sharp divide in tornadic potential with small changes in cold pool intensity (by varying heat source/sink magnitude) was noted and they also show that increasing low-level updraft intensity increases tornadic potential. However, neither low-level updraft or cold pool characteristics were solely responsible for changes in tornadic potential, and rather a combination of the two is needed.

When investigating a model ensemble, Markowski (2020) found that differences between weakly and significantly tornadic storms were not explained by differences in low-level updraft strength, outflow buoyancy, or circulation. In fact, the author posits that, based on current knowledge, prediction of stronger rotation in some weakly tornadic cases than in some of the significantly tornadic cases would have been justified, highlighting our lack of knowledge of some key difference between supercells with tornadoes of different intensities (Fig. 2.1).

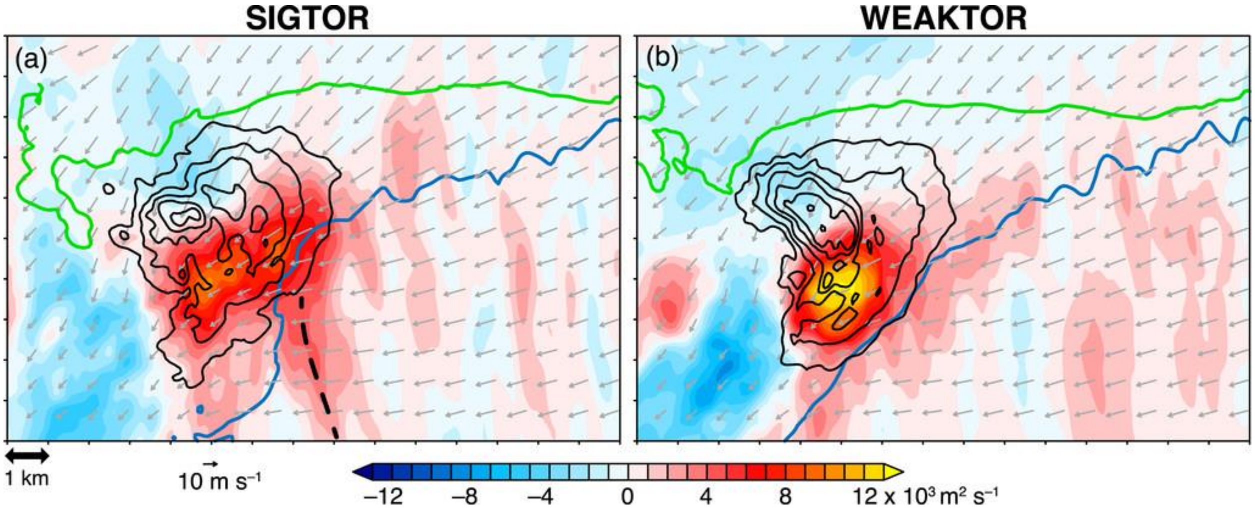

Figure 2.1: The ensemble mean circulations at the lowest grid level studied in Markowski (2020). The black contours denote vertical velocity and the dashed line in (a) shows a ribbon of higher circulation air discussed in their section 3b.

Sessa and Trapp (2020) analyzed 102 tornadic events and found that low-level mesocyclone *intensity* is not well correlated with tornado intensity (Fig. 2.2a). The authors did find that *mesocyclone width* in pre-tornadic storms is highly correlated with the enhanced Fujita scale (EF; Edwards et al. 2013) rating for the eventual tornado (Fig. 2.2b). Again, however, as with many studies on tornadoes, non-tornadic cases were not included in the analyses therein. While the study addresses the pre-tornadic period, they do not provide investigation into the time series of mesocyclone intensity or mesocyclone width during their investigation period. All analyses presented therein are with respect to either mean or maximum value of a given characteristic for the entire pre-tornadic period.

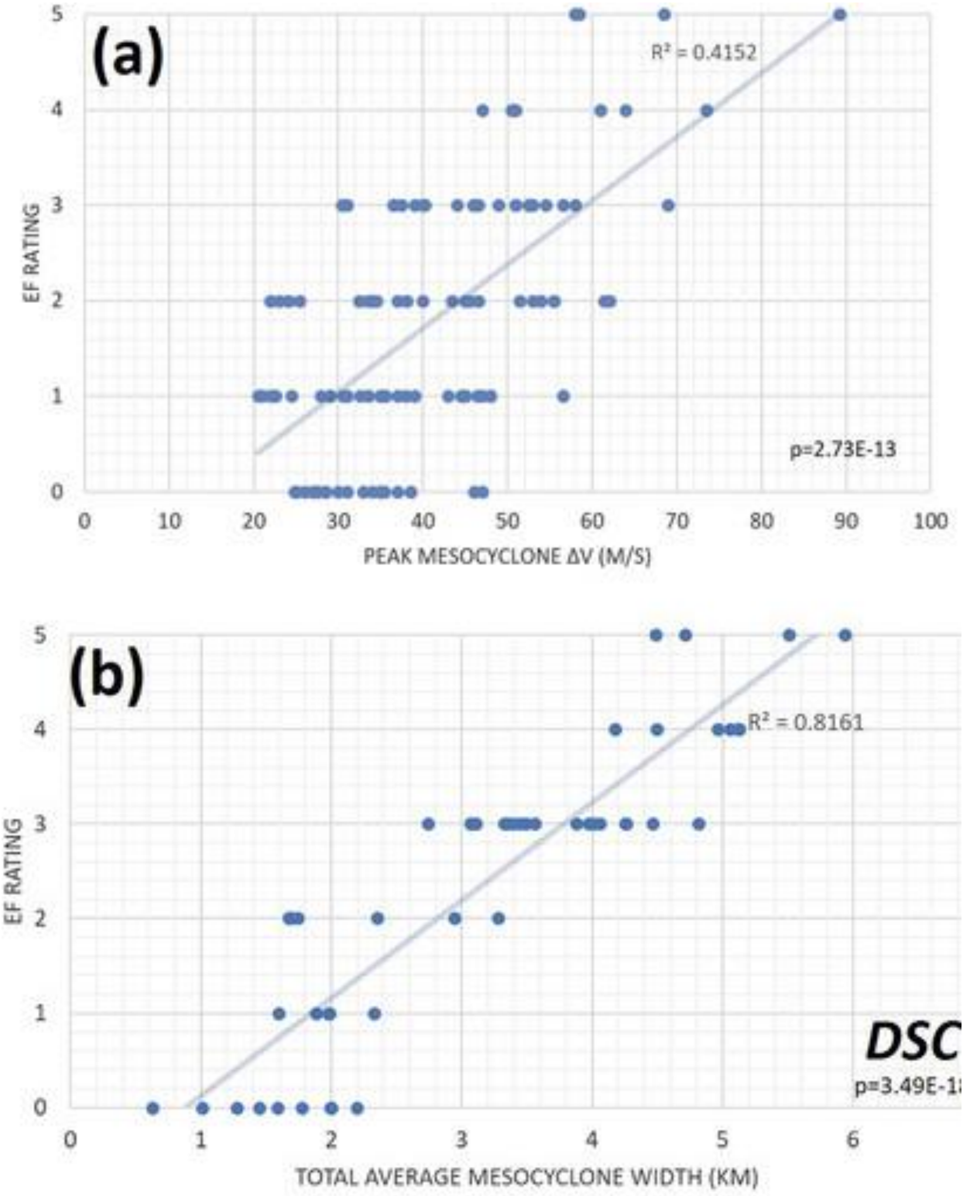

Figure 2.2: Scatterplots with regression lines from Sessa and Trapp (2020) showing the (a; from their Figure 14) peak mesocyclone velocity change (a proxy for mesocyclone intensity) versus EF scale rating for all cases, and (b; from their Figure 3) total average mesocyclone width versus EF scale rating for discrete supercells only.

More recently, Peters et al. (2023) showed that mesocyclone radius was correlated with several low-level dynamic quantities, such as horizontal streamwise vorticity, associated with stronger tornado-like vortices. The authors varied low-level storm-relative flow and horizontal streamwise vorticity in large eddy simulations to parse out differences in behavior of the low-level mesocyclone based on changes in kinematics. They show that streamwise vorticity, not storm-relative flow, acts as the primary regulation on LLM characteristics and, therefore, is barotropic in nature. The results from Peters et al. (2023) somewhat counter the results from Roberts and Xue (2017). Roberts and Xue 2017 showed that LLM circulation budgets were primarily barotropic only when frictional effects are applied to only the background environmental wind and were much weaker than LLMs generated with frictional effects applied to the full wind field. As with Sessa and Trapp (2020), Roberts and Xue (2017) and Peters et al. (2023) also did not examine non-tornadic cases.

Other recent studies have attempted to address differences between tornadic and non-tornadic mesocyclones using model-based studies. Coffer and Parker (2017) used CM1 initialized with composite soundings from the Verifications of the Origins of Rotation in Tornadoes Experiment 2 (VORTEX2; Wurman et al. 2012) found tornadic supercells form much stronger low-level updrafts than their non-tornadic counterparts, despite having similar rear-flank downdraft buoyancies. The main reason they state for the difference in updraft intensity due to differences in the VPPGF.

Coffer et al. (2023) used CM1 to investigate the role that environmental and baroclinically generated streamwise vorticity plays in supercell LLMs over their respective lifecycles. They found that a large majority (more than 90%) of LLM vertical vorticity for both case types can be attributed to the horizontal vorticity present in the environment and not from baroclinically generation horizontal vorticity from the forward flank. Results similar to those presented therein can be found in Coffer et al. (2017), where they find that LLM maintenance is linked primarily to environmental streamwise vorticity. Both results from Coffer et al. (2017) and Coffer et al. (2023) suggest that the NSE may be a far more important source of horizontal vorticity and speculate that large amounts of baroclinically generated forward flank horizontal vorticity may in fact be detrimental to low-level mesocyclone and tornado development because of the enhanced negative buoyancy found in forward flank air. They counter that the ingestion of forward flank horizontal vorticity seen in previous studies may rather be a "*symptom*" of the dynamic lifting caused the intensifying rotation of a strengthening low-level mesocyclone rather than a contributing factor to tornadogenesis. However, the results presented therein are opposite to what has been found in previous modeling and observational studies (e.g., Rotunno and Klemp 1985; Davies-Jones and Brooks 1993; Markowski et al. 2008, 2012; Beck and Weiss 2013; Dahl et al. 2014; Parker and Dahl 2015; Marquis et al. 2016), where the primary driver of near-ground rotation was baroclinic in nature. In fact, Markowski et al. (2012) states that, as LLM intensity increased in the case study they examined, the air parcels within the LLM became increasingly dominated by parcels that originated from outflow air.

One potential problem with some of the idealized model simulations in recent works is because of the use of a free-slip boundary condition. Several other recent studies (e.g., Schenkman et al. 2014; Schenkman et al. 2016; Markowski 2016; Mashiko 2016; Roberts and Xue 2017; Roberts et al. 2016, 2020; Boyer and Dahl 2020; Tao and Tamura 2020) have shown the importance of the frictional generation of horizontal vorticity which contribute to a supercell's overall vorticity budget. Free-slip boundaries are unable to generate vorticity via frictional effects. Therefore, the lack of frictional effects in free-slip models may generate vorticity budgets that are not representative of real-world processes and may skew the results of those studies in an unrealistic way.

A key motivator for this work is that LLMs are often not obvious features at low levels in radar data of supercells. For example, some high-resolution studies have provided evidence that LLMs can have rapidly-evolving lifecycles and may form or dissipate over short (sometimes on the order of sub-minute) time scales (e.g., Skinner et al. 2014), and behave as essentially *transient* features (Fig. 2.3). Given the aforementioned importance of dynamic lifting induced by low-level rotation, it stands to reason that the *duration over which a LLM continuously persists may be important in establishing a sufficiently long period of updraft enhancement to tilt and stretch vertical vorticity to tornadic levels*.

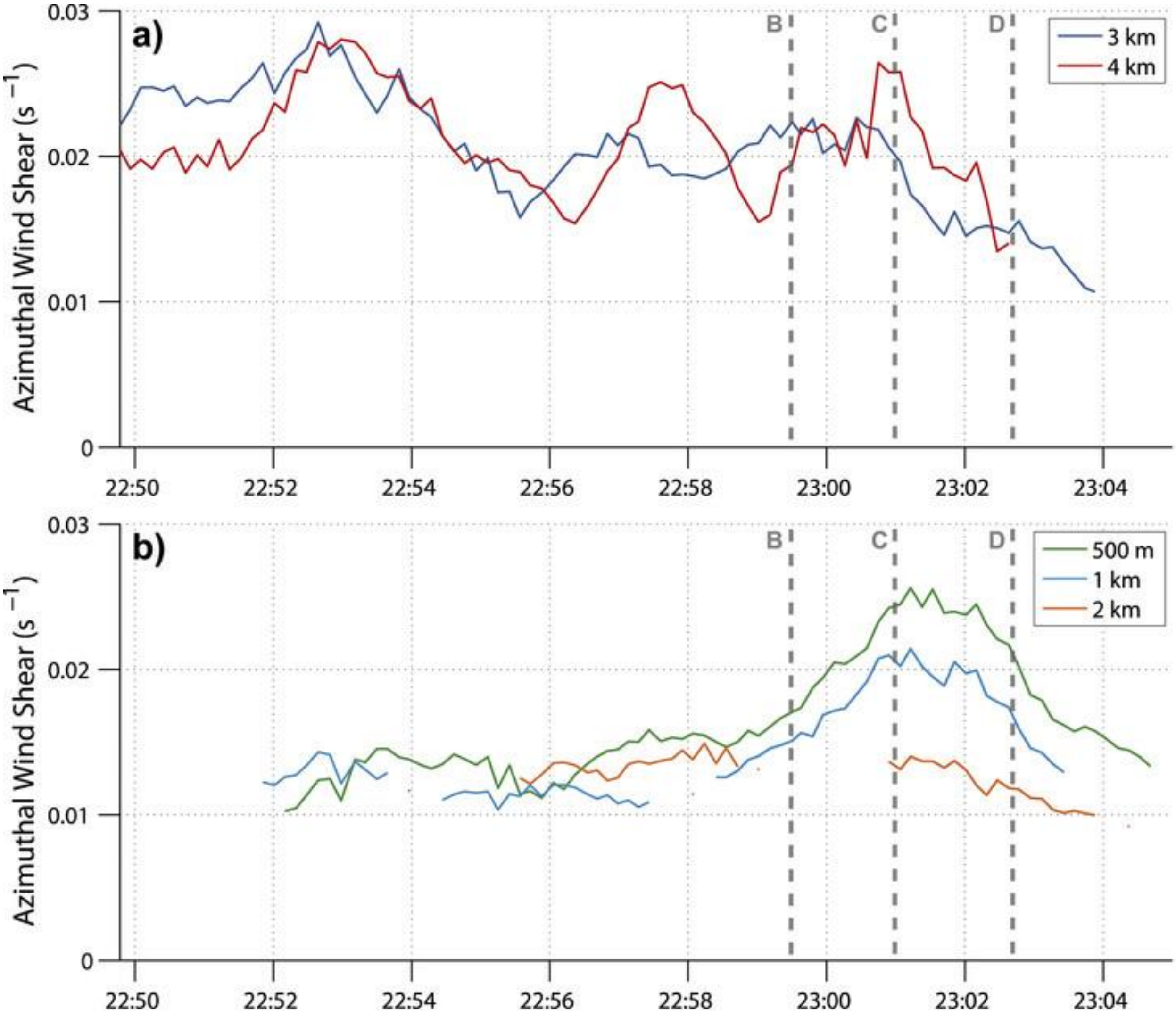

Figure 2.3: Time series data from Skinner et al. (2014) of AzShear at various grid levels ((a), 3 and 4 km, and (b) 500 m, 1 km, and 2 km) within a non-tornadic supercell recorded on 10 May 2010 by the MWR-05XP mobile phased-array. The gaps in data show times when the maximum AzShear was not associated with either the LLM or MLM. The vertical dashed lined B, C, and D denote times when the TTUKa-2 mobile radar observed internal RFD surges.

Another characteristic of mesocyclones and tornadoes that has received some attention is the tilt or displacement of the low and midlevel mesocyclones. Observational and modeling studies have investigated tornado and mesocyclone tilt, as it is thought that an increasingly tilted tornado or updraft can be detrimental to tornado or supercell intensity. Observationally, French et al. (2014) looked at the inclination angle of the TVSs for two tornadic supercells using three different heights AGL during ongoing tornadoes and found that the TVS became more tilted as the storms approached the time of tornado dissipation. French and Kingfield (2019) revisited TVS inclination angle for low-levels (~2–3 km ARL) during the time approaching tornado dissipation. Their results showed that, for 36 cases, there was no obvious trend in inclination in the time approaching tornado dissipation.

Two modeling studies (Guarriello et al. 2018 and Brown and Nowotarski 2019) investigated changes in mesocyclone separation distance, defined as the distance between the maximum of the near-surface circulation and the 1–6 km updraft helicity maximum, by varying NSE characteristics. Guarriello et al. (2018) found that small changes in the low-level wind profile have substantial effects on mesocyclone separation distance and an inverse relationship between mesocyclone separation distance and near-surface vorticity. They also state that decreasing mesocyclone separation distance tends to lead the increase in near-surface vorticity, but that the intensity of their proxy for the midlevel mesocyclone (MLM) showed no obvious role in strengthening the near-surface vertical vorticity, suggesting that, while a more tilted mesocyclone may indeed be detrimental to tornadic intensity, it does not appear to have an effect on MLM intensity.

Brown and Nowotarski (2019) used the same mesocyclone separation distance as Guarriello et al. (2018) and an additional metric that they refer to as the “average mesocyclone separation” to mute the rapid variations in mesocyclone separation distance. They analyzed how changes in near-surface thermodynamics may affect mesocyclone separation distance and near-surface vorticity. Their study also showed that increasing LCL height tended to push the near-surface circulation ahead of the MLM, as more negatively buoyant outflow would act to more quickly advect near-surface circulation. They also found the same inverse relationship between mesocyclone separation distance and near-surface vorticity as Guarriello et al. (2018). They mention that a large VPPGF is found under MLMs in their simulations prior to the maximum in low-level vorticity, but that the area of VPPGF needs to be approximately aligned with an area of near-surface vorticity for adequate vortex tilting and stretching to occur to generate strong near-surface vertical vorticity.

Direct climatological comparisons of the *temporal evolution* of intensity and *transience* of low-level rotation in supercells during the time prior to tornadogenesis and tornadogenesis failure has not been performed. Are low-level mesocyclones transient? Are they required to be present for a certain period of time before tornado formation is supported? Are their lifecycles different in tornadic vs. non-tornadic supercells? These are basic questions that have not been examined observationally. The next part of this study will address the need for pre-tornadic/non-tornadic climatological datasets of supercell mesocyclone rotation by analyzing NWS WSR-88D data.

Objective 2: Conduct a five-year (2013–2017) climatology of the temporal evolution of LLMs for tornadic supercells prior to tornadogenesis and for non-tornadic supercells prior to *each cell's maximum 0–1 km AzShear to investigate the necessity and transience of these features between case types.*

- Are LLMs transient features? If so, how transient are they? Are they more transient in one case type?
- Is the temporal evolution of LLMs different prior to tornadogenesis and tornadogenesis failure?
    - Hypothesis: LLMs are transient, especially early in the 60-minute period. They become less transient earlier as the time of tornadogenesis draws nearer when compared to the time approaching tornadogenesis failure.
- Is there a certain amount of time necessary for a LLM to be present for tornadogenesis to occur?
- Does the amount of time the LLM is present prior to tornadogenesis have any relationship with tornado intensity?
- Does mesocyclone tilt or the separation distance between the MLM and LLM play any role in differentiating between tornadic and non-tornadic supercells prior to G/F?
- How does the NSE affect LLM intensity and transience? Is it the same for both case types?

2.2 Data and Methods

2.2.1 Case Selection

We use a radar-based climatology of supercells across the contiguous United States (Fig. 2.4) drawn from the WSR-88D radar network to assess changes in LLM and MLM AzShear for the hour period prior to G/F. The initial dataset of 62 non-tornadic and 68 tornadic cells used in T21 were analyzed. The cases were drawn from a Storm Prediction Center (SPC) convective mode database from 2015 for non-tornadic cases and from 2013-2017 for tornadic cases. The analyzed storms do not contain splits or mergers and had discrete hook echoes to mitigate complicating processes like mergers within the already complex tornadogenesis process. Strict case selection allows for more direct attribution of physical processes to internal storm dynamics rather than from the effects of external factors.

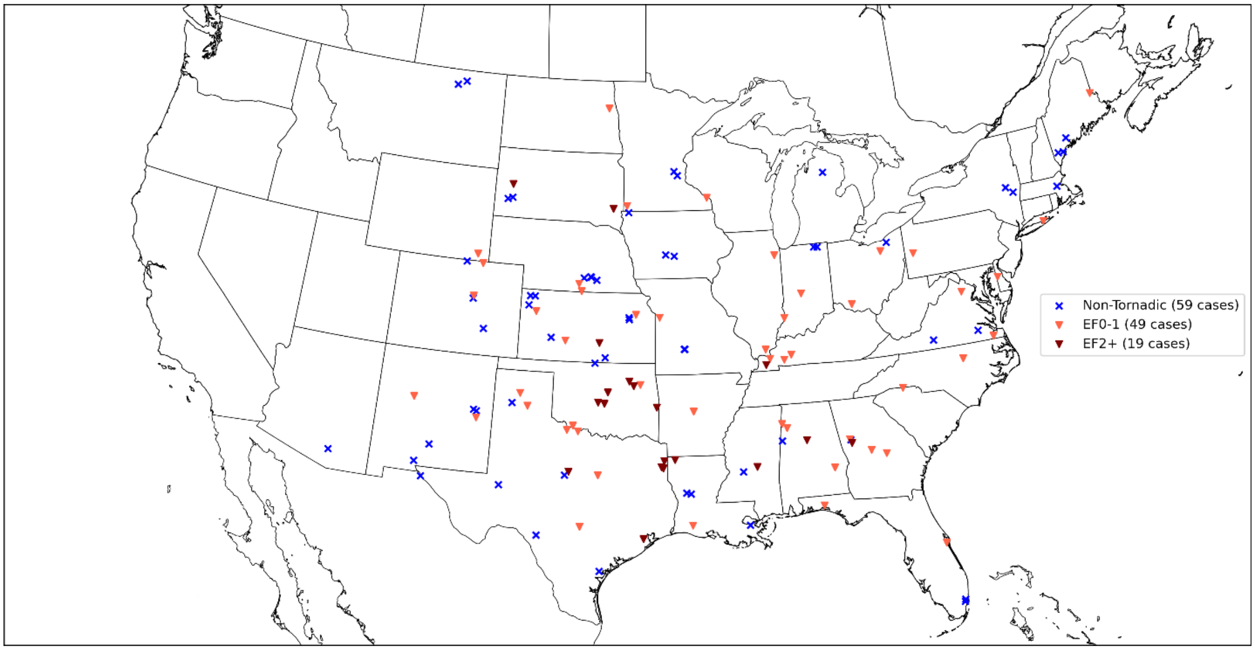

Figure 2.4: A map of the contiguous United States showing the locations of G/F for non-tornadic (blue Xs), weakly tornadic (light red triangle), and strongly tornadic (dark red triangle) investigated.

As in T21, if a given supercell spawned several tornadoes, the first in the series was used as the time of G and subsequent tornadoes were not considered. The time of G was determined by the time of the first tornado report or the first radar volume with an apparent tornadic debris signature (Ryzhkov et al. 2005), whichever occurred first. The enhanced Fujita scale (EF; Edwards et al. 2013) rating of the (first) tornado a given supercell spawned was used to further split the tornadic dataset into two case types; strongly tornadic (EF2–4) and weakly tornadic (EF0–1). The tornado intensity breakdown is 49 (36 EF0 and 13 EF1) weakly tornadic cases and 19 (13 EF2, 4 EF3, and 2 EF4) strongly tornadic cases used for analysis.

Three non-tornadic cases which did not have radar data available for the full hour were removed, leaving a total of 59 non-tornadic supercells for this study. The time of F was determined to be the time at which the supercell lifetime maximum low-level AzShear occurred. While 0–500 m AzShear was investigated herein, cases that were near the edge of the 60 km range restriction when their maximum AzShear occurred may be too far from the radar for the 0.5º elevation scan to be within 500 m AGL. For that reason, the 0–1 km AzShear value was used to assess the time of F, so that the volume scan during which the supercell lifetime maximum 0–1 km AzShear occurred is designated as F (as done in T21).

2.2.2 AzShear Calculation

To assess the rotational intensity of mesocyclones, we used azimuthal shear (AzShear) as it is a proxy for rotational intensity. AzShear is a measure of the change in Doppler velocity over the change in azimuth (i.e., the horizontal wind shear from one radar beam to the next). As such, AzShear provides a measure of mesocyclone intensity from a single radar, rather than requiring multi-radar/multi-sensor observations to calculate a full wind field. We used Doppler velocity data from a given WSR-88D volume scan to calculate AzShear for four different low-level layer depths (0–500 m, 0–1 km, 0–2 km, and 0–3 km; the LLMs in this study), and one midlevel layer (3–6 km; the MLMs in this study). The height of a given radar beam is approximated using topographical information about the region surrounding a given WSR-88D to provide the beam height AGL. Anomalous beam refraction from atmospheric effects is not accounted for in the beam height estimates. AzShear fields for a given elevation angle are calculated in polar space using the local, least squares derivative approach discussed in Mahalik et al. (2019). AzShear data are then converted to a cartesian grid of a certain spacing (i.e., 0.005º by 0.005º). The maximum value of AzShear for a given grid cell is determined to be the maximum AzShear from all elevation angles that intersect that cell. Shallower layer depth, or higher grid resolution, allows for fewer possible tilts to transect a given layer depth for use in determining the maximum AzShear of each grid cell, thus reducing the sample size for a given layer, but increasing the vertical resolution of AzShear or vice versa.

2.2.3 Climatological Analyses

Throughout the literature, the rotational intensity of varying low-level depths has been suggested as important to tornadogenesis. We chose to investigate the maximum AzShear as a proxy for rotational intensity for the four different LLM depths and the MLM depths in this study. The maximum AzShear approximately collocated with the velocity couplet in that layer were recorded for each volume for the 60-minute period prior to G/F. The hour-long periods were then sub-divided into six 10-minute sub-periods to obtain the distributions of a given layer’s AzShear from all volume scans within the sub-periods. The bulk distribution statistics, and time-normalized change distributions, of LLMs and MLMs during the sub-periods were analyzed and compared across case types. Time-normalized changes between 10-minute sub-periods were calculated by determining the mean AzShear and mean scan time during a given sub-period, for a given case, and then taking the difference of these sub-period mean values, and adjusting the value by calculating the time between sub-period means and linearly adjusting the value to 10 minutes using

$$\Delta x_{norm} = \frac{\big(x(t) - x(t-1)\big) \cdot \Delta s_{norm}}{\Delta s_{actual}} \tag{1}$$

as in T21, where Δx_{norm} is the linearly time-normalized change, $x(t)$ is the sub-period mean value of a given variable, $x(t-1)$ is the mean value of the same variable at one sub-period previous, Δs_{norm} is the normalization time (10 minutes) in seconds to linearly adjust values such that their time between mean scan times is that normalized time, and Δs_{actual} is the time in seconds between the two sub-period mean scan times.

To assess mesocyclone transience, we implemented a minimum AzShear threshold of 0.005 s^{-1} to define a mesocyclone based on Burgess et al. (1979). Any volumes where the AzShear was below 0.005 s^{-1}, a mesocyclone was denoted as not present. The transience information was then used to determine the amount of time a mesocyclone was continuously present prior to G/F to investigate any differences in the duration that LLMs or MLMs are present between case types.

We also looked at the distance and direction from the location of the MLM to the location of the LLM, with respect to mean storm motion. The mean storm motions were calculated using the mean of the directions of travel of the LLM and MLM combined over the 60-minute investigation period. The distance and direction from the MLM to the LLM are calculated using the latitude and longitude points of the locations of the maximum AzShear in the LLM and MLM. The directions between them are then rotated with respect to storm motion before performing bulk analyses of the 10-minute sub-periods. Advection correction for the time between the low-level and midlevel data has not been performed as WDSS-II only provides a single volume time, not individual elevation scan times. The lack of advection correction does introduce large errors in this analysis that are not accounted for herein.

The inclination angle from the vertical between the LLM and MLM was also examined. However, these inclination angles contain large errors because of poor precision in LLM and, in particular, the MLM peak AzShear heights. While we were able to determine whether the maximum AzShear occurred between the 0–500 m, 500 m–1 km, 1–2 km, or 2–3 km layers for the LLM, we cannot tell where within the 3–6 km layer the maximum MLM AzShear was observed. To estimate the inclination angle, we used the middle point in the MLM (4.5 km) and the midpoint of the layer where the maximum LLM occurred (i.e., 250 m, 750 m, 1.5 km, or 2.5 km) as the vertical component and the horizontal separation distance calculated from the latitude and longitude points mentioned previously. Inclination angle also has not been corrected for advection for the same reason specified prior and adds even further error to the inclination angle results presented.

2.2.4 Near Storm Environment Analysis

In order to elucidate any effects of NSE characteristics on mesocyclone intensity and transience, we used Rapid Refresh model (RAP; Benjamin et al. 2016) data to approximate the NSE that each cell existed in. NSE characteristics were recorded for the nearest grid point in the inflow region of each supercell for the analysis hour directly preceding the time of the volume scan considered (i.e., a volume scan at 23:20 or 23:40 UTC would use the 23:00 UTC RAP analysis) and then averaged over the hour period. NSE characteristics studied include 0–500 m storm relative helicity (SRH), 0–1 km SRH, 0–2 km SRH, 0–3 km SRH, surface-based convective available potential energy (CAPE), most unstable (MU) CAPE, 0–3 km MUCAPE, surface-based convective inhibition (CIN), surface-based lifting condensation level (LCL), and 0–6 km shear vector magnitude.

2.2.5 Statistical Analyses

Since the distributions analyzed in this study may vary substantially from one time to the next or from one case type to another, we used nonparametric statistical tests to determine significance. A nonparametric approach allows for testing significance without assuming a specific distribution which may be dramatically different from the observed distributions. We used a combination of the Kruskal-Wallis test (Kruskal and Wallis 1952) and post-hoc Dunn's test (Dunn 1964) with "Bonferroni" p-value correction to determine significant differences between case types within the 10-minute sub-periods and between case type mean NSE characteristics. The Kruskal-Wallis test is a nonparametric analog of the one-way ANOVA and is used for statistical significance among a group of variables while the post-hoc Dunn's test determines which variables are significantly different from which. Instances where the Kruskal-Wallis p-value was less than or equal to 0.05 were then assessed by the post-hoc Dunn's test. Bonferroni correction was applied as it is the most conservative method of p-value adjustment available for use in the Dunn's test and helps mitigate false positives more than other p-value adjustment methods available for this test. Wilcoxon signed-rank tests (Wilcoxon 1945), another type of nonparametric statistical test, were performed including the use of zero differences (Pratt 1959) to check for significant changes in a specific case type's distribution from one sub-period to the next. To assess significant relationships between the NSE and mesocyclone characteristics, we used the nonparametric Theil-Sen Estimator regression approach (Theil 1950; Sen 1968). This approach is insensitive to outliers and should give a better idea of the nature of the bulk relationships, if any, between NSE and mesocyclone characteristics.

2.3 **Results**

2.3.1 Low-Level Mesocyclone Azimuthal Shear Analysis

We evaluated four separate layers (0–500 m, 0–1 km, 0–2 km, and 0–3 km AGL) to investigate bulk LLM behavior during the hour period prior to G/F in 10-minute sub-periods (Fig. 2.5). For all layers, at all times, non-tornadic cases exhibit lower maximum AzShear values than either of the tornadic case types, and non-tornadic cases are significantly different from both tornadic subsets at most times prior to G/F. Both weakly and strongly tornadic maximum AzShear distributions show the most difference from non-tornadic cases in the 0–1 km AGL layer, where they are significantly different at the 95% confidence level for every 10-minute sub-period. However, when comparing the weakly and strongly tornadic cases, significant differences between the case types do not appear until the last 10-minute sub-period for all layers (i.e., the last 10-minute period before G). Statistical differences are most apparent (99% significance level) in the 0–2 km and 0–3 km layers.

While not significant, strongly tornadic AzShear distributions do exhibit more separation with weakly tornadic cases in the 0–3 km layer starting in the 40-to-30-minute sub-period and increasing in separation with each successive time step (Fig. 2.5d). There is considerable overlap of strongly and weakly tornadic AzShear values for all other layers until the sub-period immediately prior to G. The overlap in strongly and weakly tornadic AzShear values becomes increasingly pronounced when observing smaller and smaller layers. For example, the 0–500 m layer shows essentially no distinction between the two tornadic case types until the 10-minute period immediately prior to G (Fig. 2.5a). We interpret the time lags of differences in LLM intensity between the three case types as evidence that something dynamically important to the tornado formation and intensification process occurs first higher in a given supercell and the lower layers follow. Figure 2.6 provides example scans of Z_H and 0–1 km AzShear for G/F-~15 minutes and G/F-~5 minutes for strongly, weakly, and non-tornadic supercells.

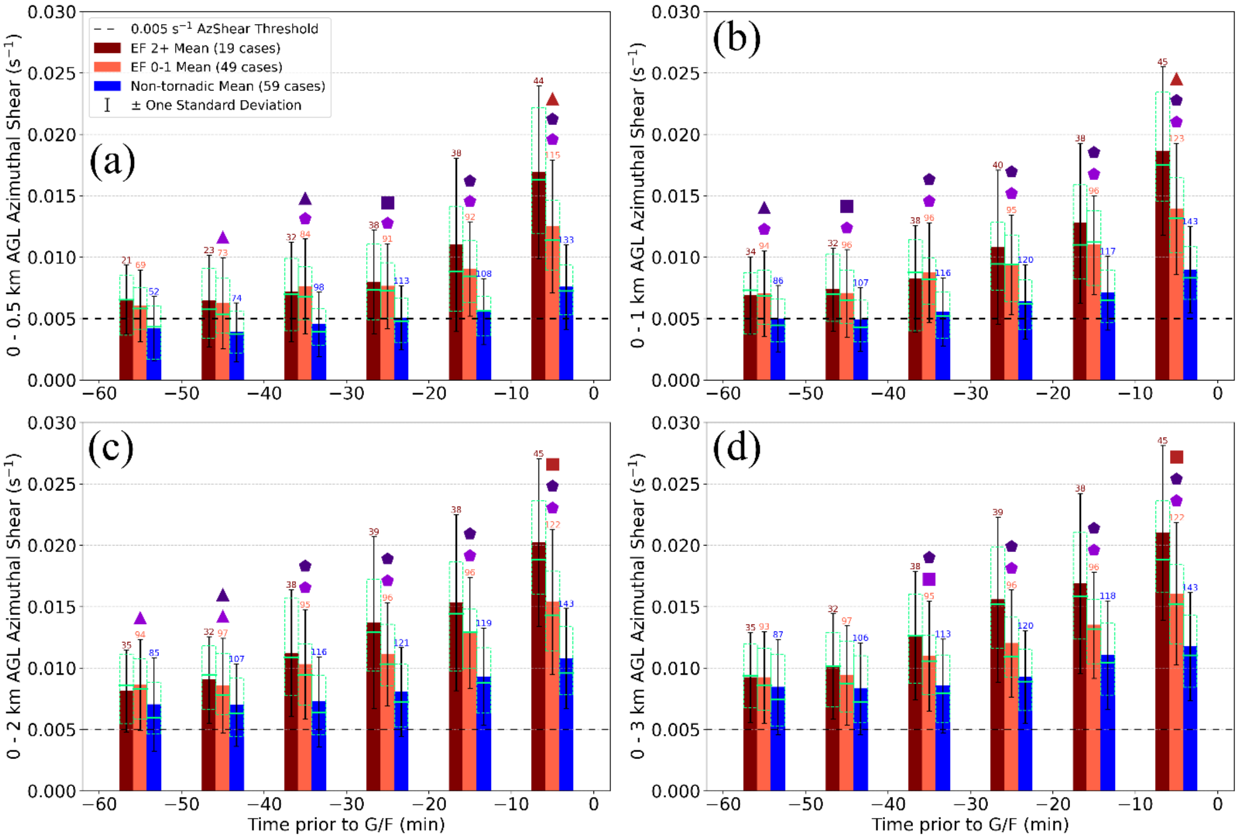

Figure 2.5: Maximum AzShear statistics for size 10-minute sub-periods in the (a) 0–500 m, (b) 0–1 km, (c) 0–2 km, and (d) 0–3 km AGL layers for strongly tornadic (dark red), weakly tornadic (light red), and non-tornadic (blue) cases. The colored number above each standard deviation line denotes the number of volume scans considered for a given case type during a given sub-period. The shapes above the weakly tornadic volume scan number denotes statistical significance at 95% (triangle), 99% (square), and 99.9% (pentagon) levels. Shapes colored in red, dark purple, and light purple indicate significant differences between strongly and weakly tornadic, strongly and non-tornadic, and weakly and non-tornadic distributions, respectively. The dashed bright green boxes overlapping each individual bar show the boxplots for each sub-period distribution for each case type. The black dashed line shows the AzShear threshold used to investigate LLM transience.

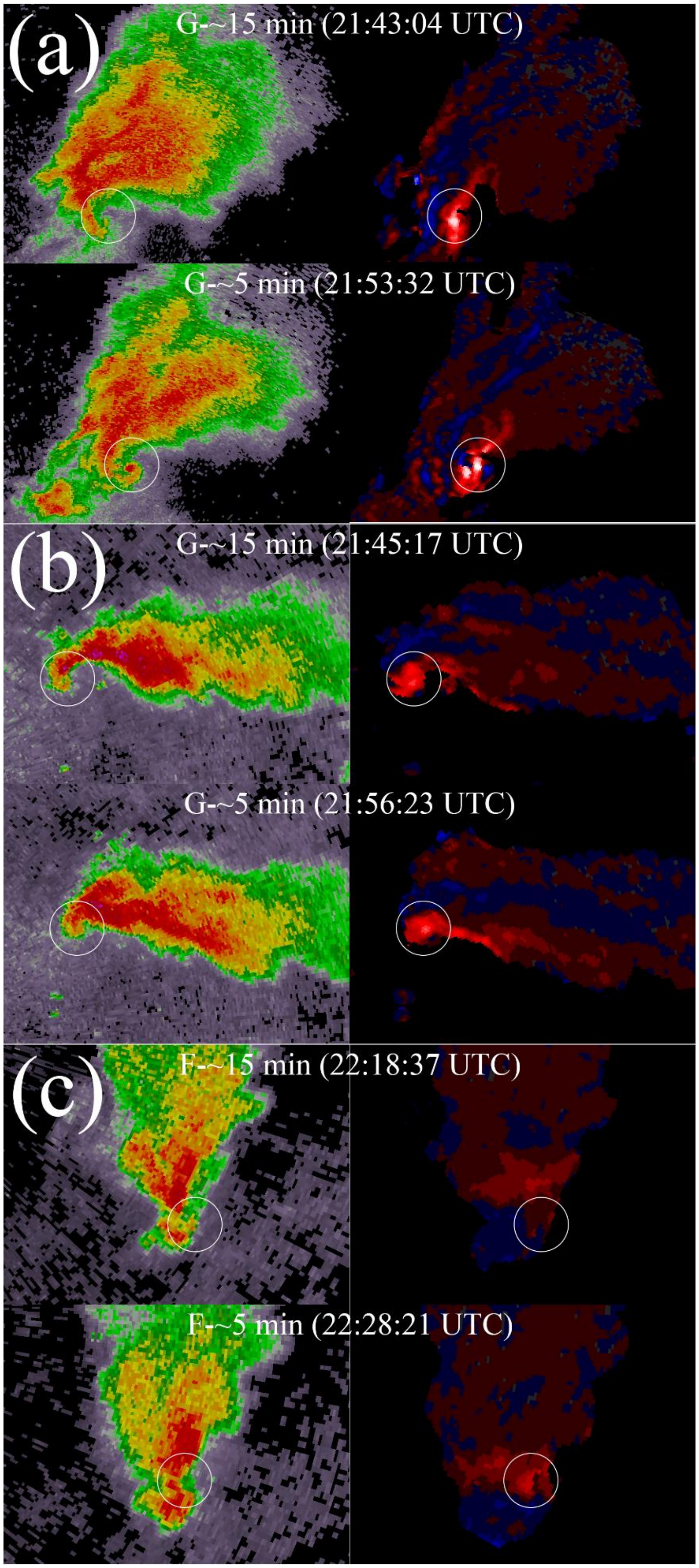
(a)
G-~15 min (21:43:04 UTC)
G-~5 min (21:53:32 UTC)
(b)
G-~15 min (21:45:17 UTC)
G-~5 min (21:56:23 UTC)
(c)
F-~15 min (22:18:37 UTC)
F-~5 min (22:28:21 UTC)

Figure 2.6: Example cases that show 0.5º tilt Z_H (right) and 0–1km AzShear (left) for (a) a strongly tornadic (EF-3) case from the KTLX WSR-88D on 19 May 2014, (b) a weakly tornadic (EF-1) case from the KFSD WSR-88D on 05 June 2014, and (c) a non-tornadic case from the KFSD WSR-88D on 25 May 2015. The top Z_H and AzShear sub-panels of each lettered panel represent data from ~15 minutes prior to G/F and the bottom sub-panels represent data from ~5 minutes prior to G/F. The white circles in each plot enclose the location of 0–1 km AzShear used from each time step.

When observing the time-normalized-change distributions of each case type, all types exhibit a general increase in AzShear from one time to the next for all layers with few exceptions (Fig. 2.7). The only mean decrease occurs in non-tornadic cases, between the two earliest periods (straddling "-50;" i.e., the 10-minute normalized change between the 60-to-50 and 50-to-40-minute sub-periods), in the lowest level AzShear and was not significantly different from zero (Fig. 2.7a). The difference between these same sub-periods shows little change in weakly tornadic cases and significant increases in all strongly tornadic layers considered. Significant increases in maximum AzShear are more prevalent between the 50-to-40- and 40-to-30-minute sub-periods for all case types. However, while non-tornadic cases exhibit significant increases in maximum AzShear, the increases are small, even when nearing the time of F, in all layers. Weakly tornadic cases exhibit changes from one sub-period to the next that sometimes resemble the strongly tornadic changes and other times resemble non-tornadic changes. Overall, weakly tornadic AzShear change distributions more closely resemble the changes shown in non-tornadic cases, especially with increasingly deep layers (Figs. 2.7c,d). Strongly tornadic cases show the largest overall increases for nearly all sub-periods for all layers analyzed. The only exceptions appear in lower levels between the 50-to-40- and 40-to-30-minute sub-periods, when weakly tornadic cases show an AzShear increase greater than that in the tornadic cases (Figs. 2.7a,b).

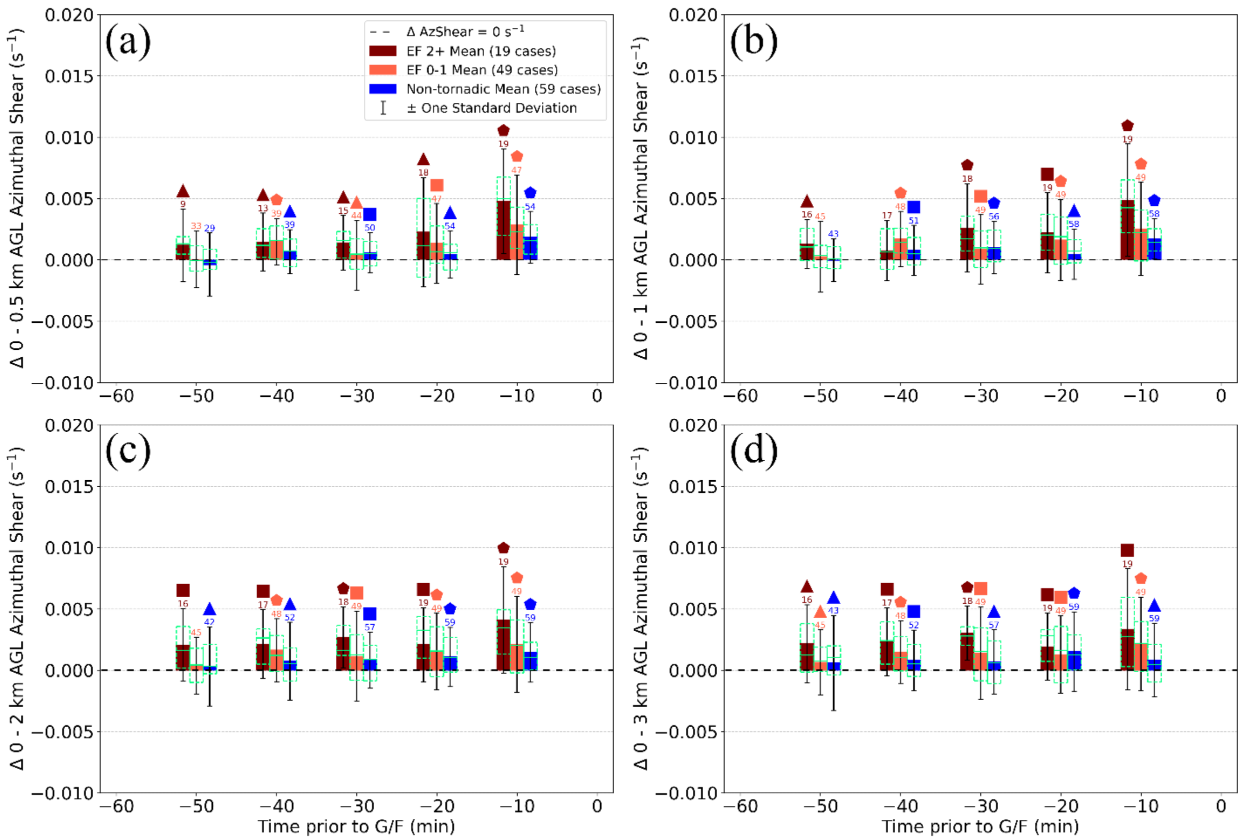

Figure 2.7: The change in AzShear distribution from one sub-period to the next (i.e. the plots straddling "-50" represent the change from the 60-to-50 to the 50-to-40-minute sub-period) for the (a) 0–500 m, (b) 0–1 km, (c) 0–2 km, and (d) 0–3 km AGL layers for strongly tornadic (dark red), weakly tornadic (light red), and non-tornadic (blue) cases. The shapes represent the same statistical significance values outlined in Figure 2.5. The bright green boxes overlaying each bar are also as in Figure 2.5. The shapes are centered over their respective case type and the colors correspond to the given case type that exhibits changes significantly different from zero. The colored number above each standard deviation line denotes the number of AzShear change values considered per case type, per bin.

As discussed previously, past studies have not focused on the transience of supercell LLMs and their relationship to tornado formation. To investigate LLM transience, we used the same AzShear threshold of 0.005 s^{-1}; LLMs were considered present when their maximum AzShear value met or exceeded this threshold and not present when below it. Observing the distributions shown in Figure 2.5 gives some sense of this transience. For all case types, rotation above the AzShear threshold is far more likely with increasingly deeper layers (i.e., AzShear values in the deepest layers of the low-levels investigated become more intense earlier in the hour observation period than in the thinner, nearer-to-the-surface low-level layers). Non-tornadic cases are the most transient at low levels, especially at earlier and earlier sub-periods.

In order to elucidate transience further, we looked at the continuous duration where a given layer's AzShear met or exceeded the 0.005 s^{-1} threshold to see if tornadic LLMs tended to be present continuously longer than non-tornadic LLMs (Fig. 2.8). For all but the 0–3 km layer, both tornadic case types had rotation continuously at or above our AzShear threshold for longer than non-tornadic cases. In the lowest layer, both strongly and weakly tornadic cases exhibit significant differences from non-tornadic cases, but have nearly identical mean and median durations with one another (Fig. 2.8a). Weakly tornadic cases are also significantly different from non-tornadic cases for the 0–1 km and 0–2 km layer, but strongly tornadic cases are not, despite visual separation between the distributions. On average, tornadic LLMs exist continuously for longer than non-tornadic LLMs.

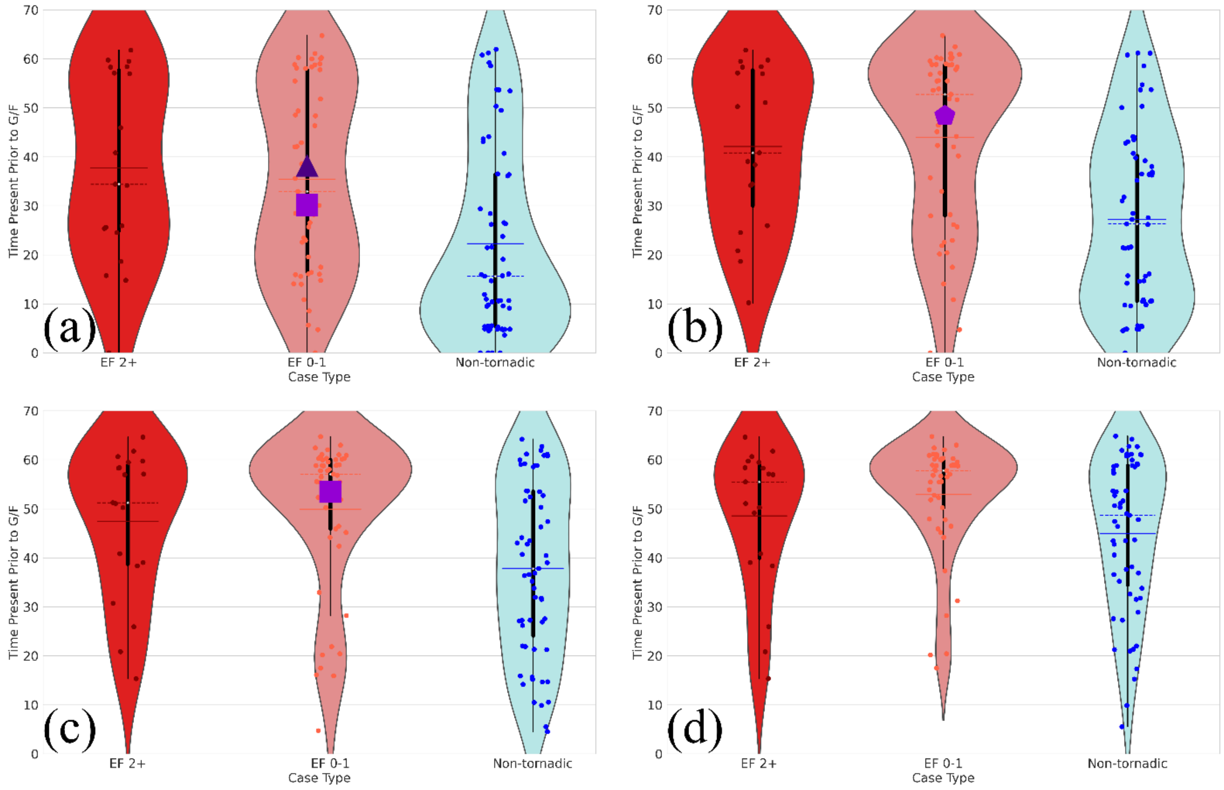

Figure 2.8: Violin plots of the continuous duration in which a strongly tornadic (dark red), weakly tornadic (light red), and non-tornadic (blue) case's AzShear met or exceeded the threshold of 0.005 s^{-1} for (a) 0–500 m, (b) 0–1 km, (c) 0–2 km, and (d) 0–3 km AGL layer. The shapes, and their respective colors, present on top of some EF 0-1 violin plots represent the same statistical significance outlined in Figure 2.5. The dashed (solid) horizontal lines overlaying each violin plot represents each case types respective median (mean) duration.

2.3.2 Midlevel Mesocyclone Azimuthal Shear Analysis

While the primary focus of this study is on the bulk characteristics of LLMs, for completeness, we analyzed the 3–6 km AzShear as a proxy for the MLM over the same hour period (and 10-minute sub-periods) as the LLMs discussed in the previous section. During the first two sub-periods (60-to-50 and 50-to-40 minutes prior to G/F), the distributions of MLM AzShear values are essentially identical between all three case types (Fig. 2.9). Similar patterns continue between the weakly and non-tornadic cases for the remainder of the analysis period; gradually increasing in intensity until G/F. *The strongly tornadic cases, however, show a substantial increase* *in MLM intensity relative to both weakly and non-tornadic cases during the 40-to-30-minute sub-period, which persists for all sub-periods thereafter.* A consistently stronger MLM in excess of a half hour prior to G that is not found in weakly or non-tornadic MLMs, or in LLMs of any case type, is evidence of a potential dynamic precursor to strong tornado formation. Figure 2.10 provides example scans of Z_H and 3–6 km AzShear for G/F-~45 minutes and G/F-~35 minutes for strongly, weakly, and non-tornadic supercells.

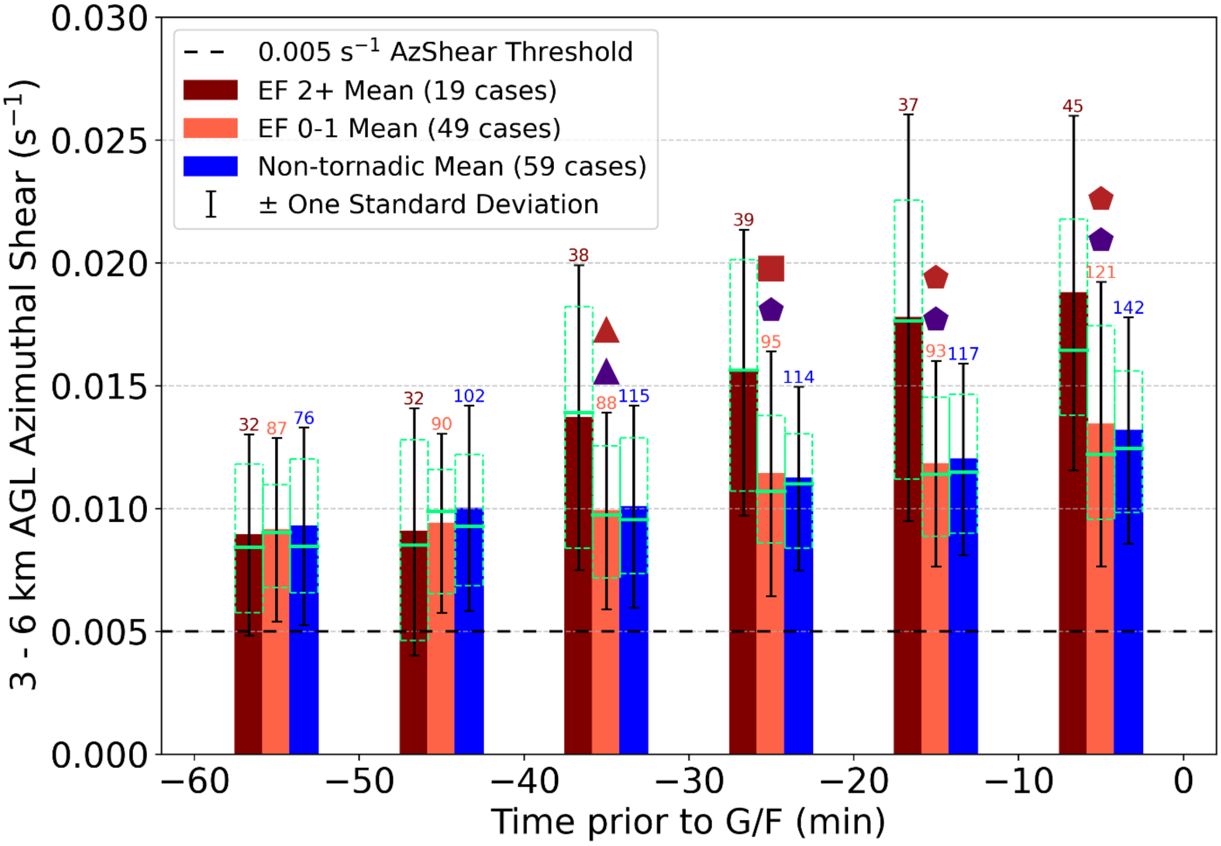

Figure 2.9: As in Fig. 2.5, but for the 3–6 km layer AzShear.

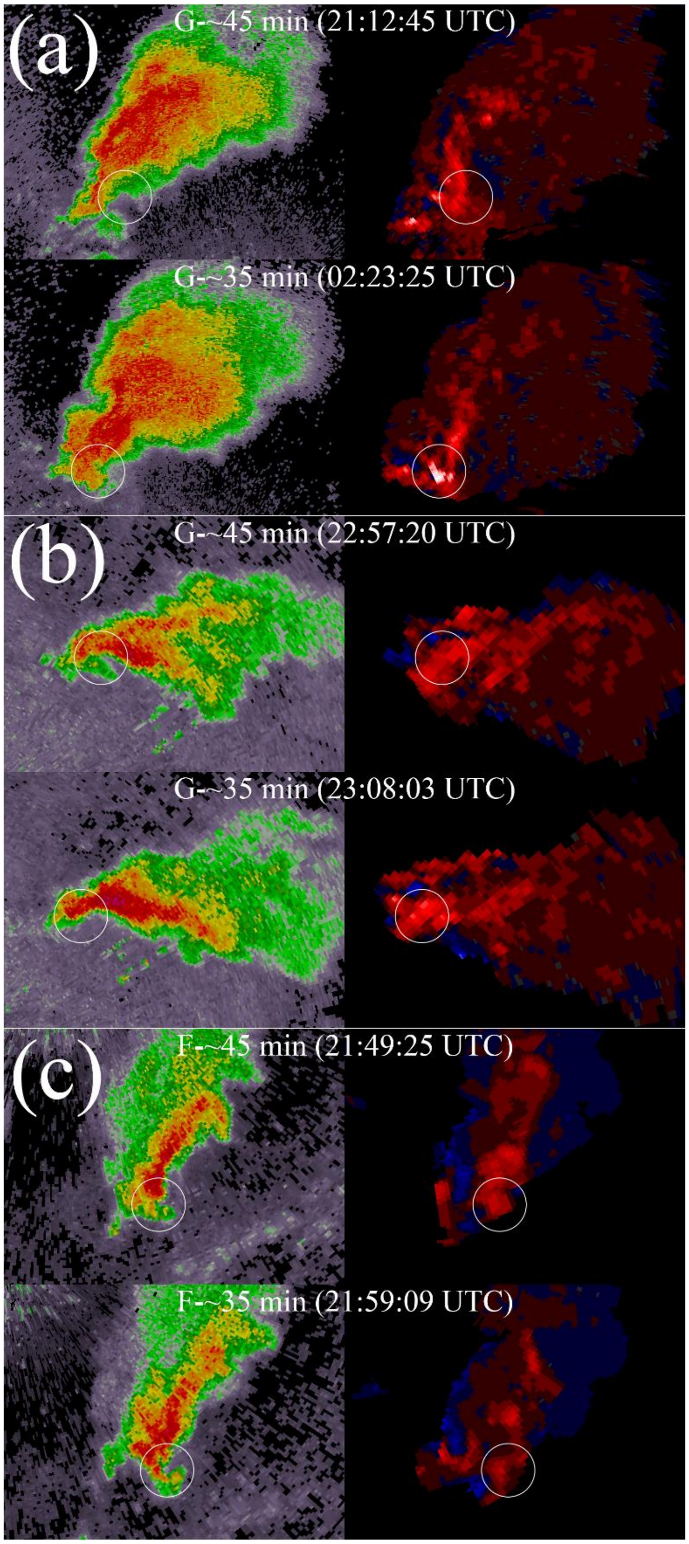

Figure 2.10: As in Fig. 2.6, but for 3–6 km AzShear (right) for G/F-~45 minutes (top sub-panels) and G/F-~35 minutes (bottom sub-panels).

The time-normalized-changes in these distributions are shown in Figure 2.11. In the early sub-periods (60-to-50- to 50-to-40-minute change), both weakly and non-tornadic cases exhibit significant increases in AzShear while strongly tornadic cases do not. However, for the next two sub-periods (the change from the 50-to-40- to 40-to-30-minute sub-periods) there is a significant increase in strongly tornadic AzShear. Another larger jump in strongly tornadic MLM AzShear occurs between the 30-to-20 and 20-to-10-minute sub-periods. The later distribution jump, however, shows more overlap with weakly and non-tornadic changes in MLM AzShear than the earlier change. Examining the time-normalized change further highlights how stark of an increase occurs in MLM intensity during this 10-minute period.

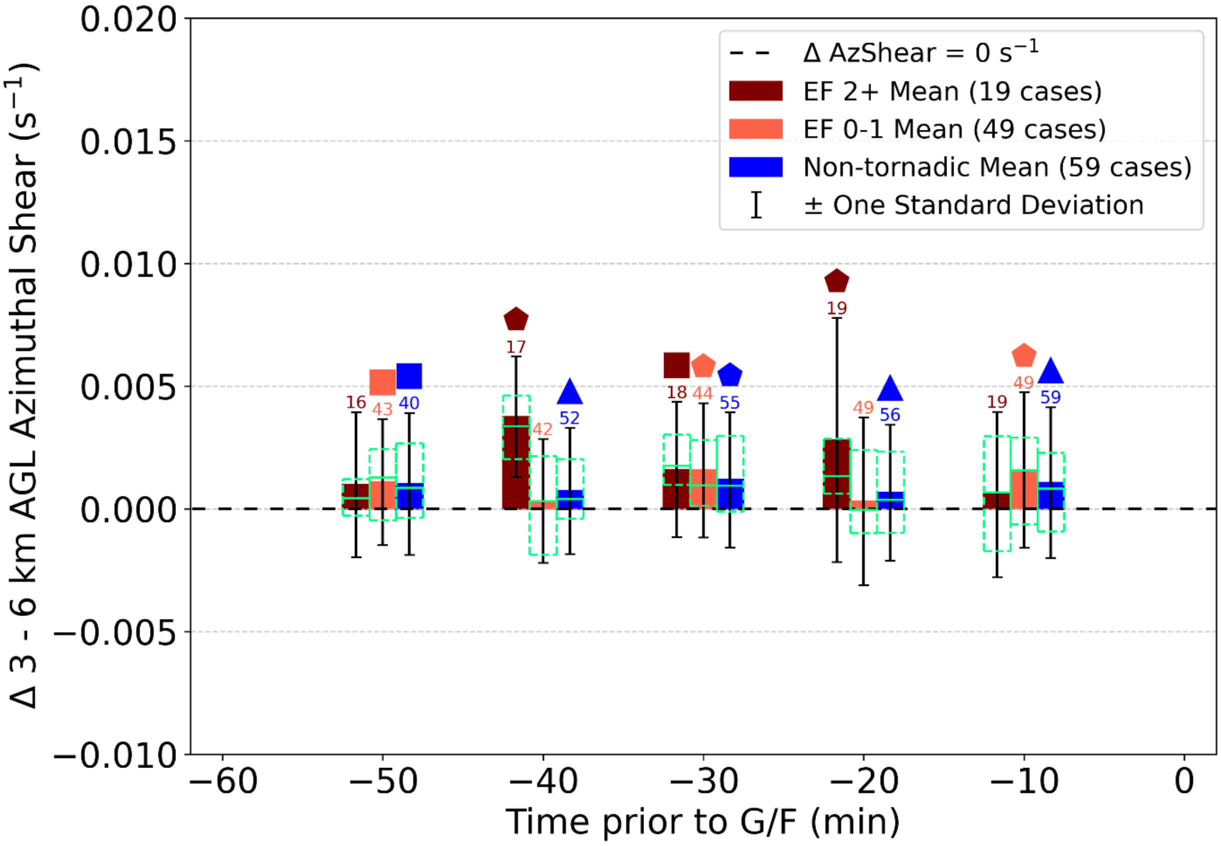

Figure 2.11: As in Fig. 2.7, but for the 3–6 km layer AzShear.

We again use the continuous time during which the MLM is at or exceeding the same AzShear threshold of 0.005 s^{-1} to evaluate transience. For MLMs there is little difference between the distributions of durations between case types (Fig. 2.12). Case type means are essentially the same (~50 minutes for strongly tornadic, ~48 minutes for weakly tornadic, and just shy of 50 minutes for non-tornadic MLMs). Medians show slightly more exaggerated differences (~57, ~57, and ~54 minutes for strongly, weakly, and non-tornadic respectively), but none of the distributions are significantly different from one another. We suspect that a higher AzShear threshold value for MLMs may elucidate some differences in transience that our low threshold cannot parse out since MLMs tend to be rotating much more rapidly than LLMs.

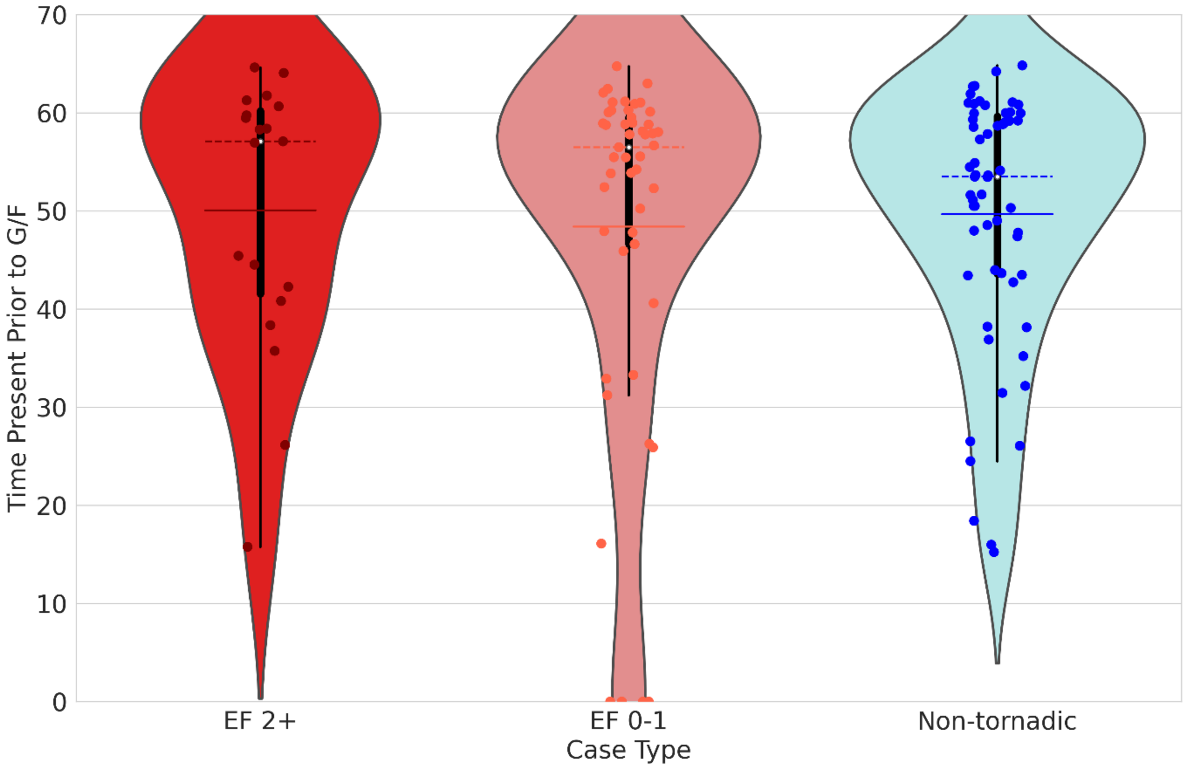

Figure 2.12: As in Fig. 2.8, but for the 3–6 km layer duration of AzShear at or above the AzShear threshold value.

2.3.3 Mesocyclone Inclination and Storm-Relative Separation Analyses

Of the studies we mentioned that addressed mesocyclone separation distance or tornado tilt, neither observational study (French et al. 2014; French and Kingfield 2019) addressed the time preceding G, let alone F. While the modeling studies (Guarriello et al. 2018; Brown and Nowotarski 2019) do address a long period leading up to tornadogenesis, again, neither study investigates simulations of non-tornadic supercells. As such, we analyzed the mesocyclone inclination angle (i.e., the angle from perfectly vertical) by using the mid-point of the layer in which the maximum LLM AzShear occurred, and the mid-point of the MLM layer as a proxy for mesocyclone tilt. Overall, there appears to be little difference in tilt between case types (Fig. 2.13). There are no significant differences between case types during any sub-period in the hour considered. Overall, strongly tornadic mesocyclones tended to be less tilted than weakly or non-tornadic cases, but the substantial overlap in distributions suggests that any role mesocyclone inclination may play is small in comparison to other mesocyclone characteristics.

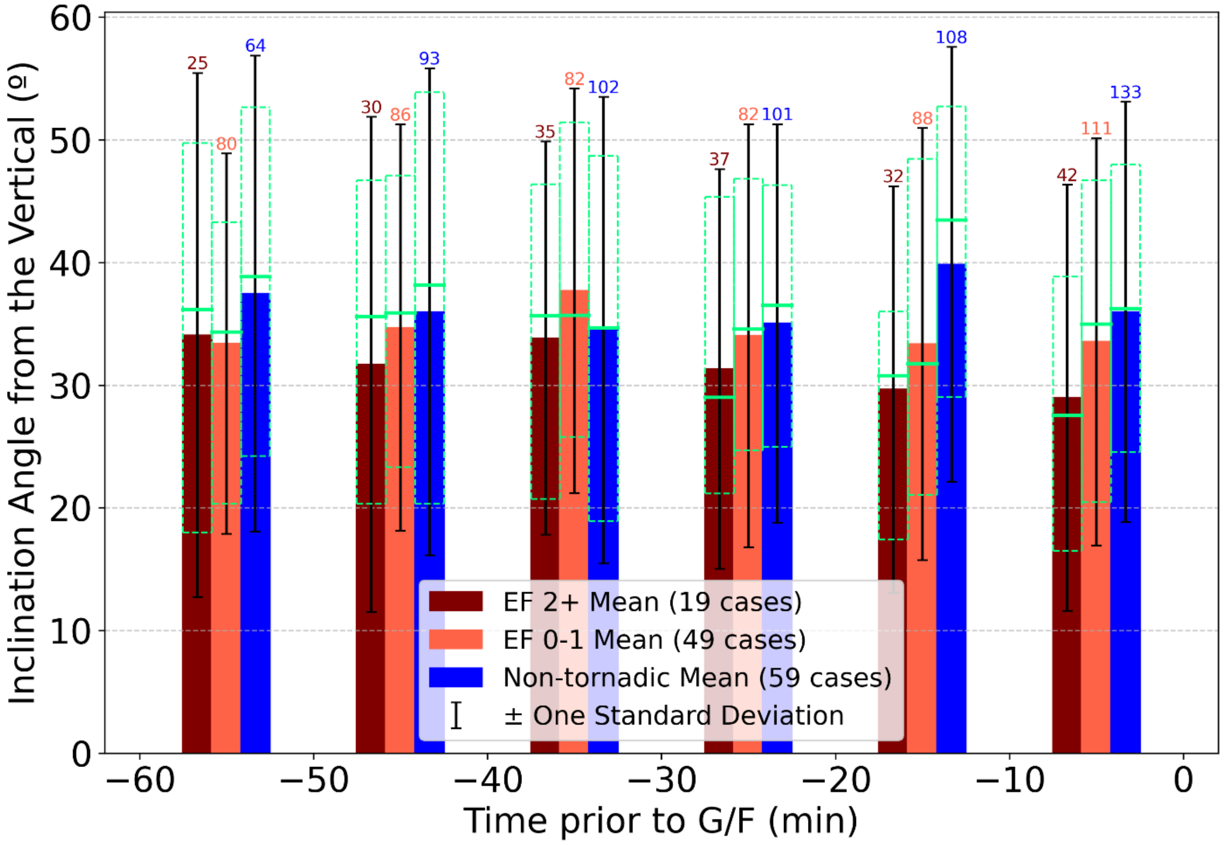

Figure 2.13: As in Fig. 2.5, but for the inclination of mesocyclones from the vertical (0º being perpendicular to the ground and 90º being parallel to the ground).

We also analyzed the physical separation of the LLM with respect to the MLM after removing storm motion (Fig. 2.14). In general, there is substantial overlap in both range and direction for all three case types. LLMs tend to be 2-to-3 km behind MLMs, on average, with respect to storm motion. Non-tornadic mean LLM location with respect to the MLM tends to be slightly left of storm motion while strongly tornadic cases tend to be slightly right of storm motion, but none of these case types are significantly different from one another in either range or relative direction. Therefore, the orientation of mesocyclones does not appear to play a critical role in differentiating among these three case types.

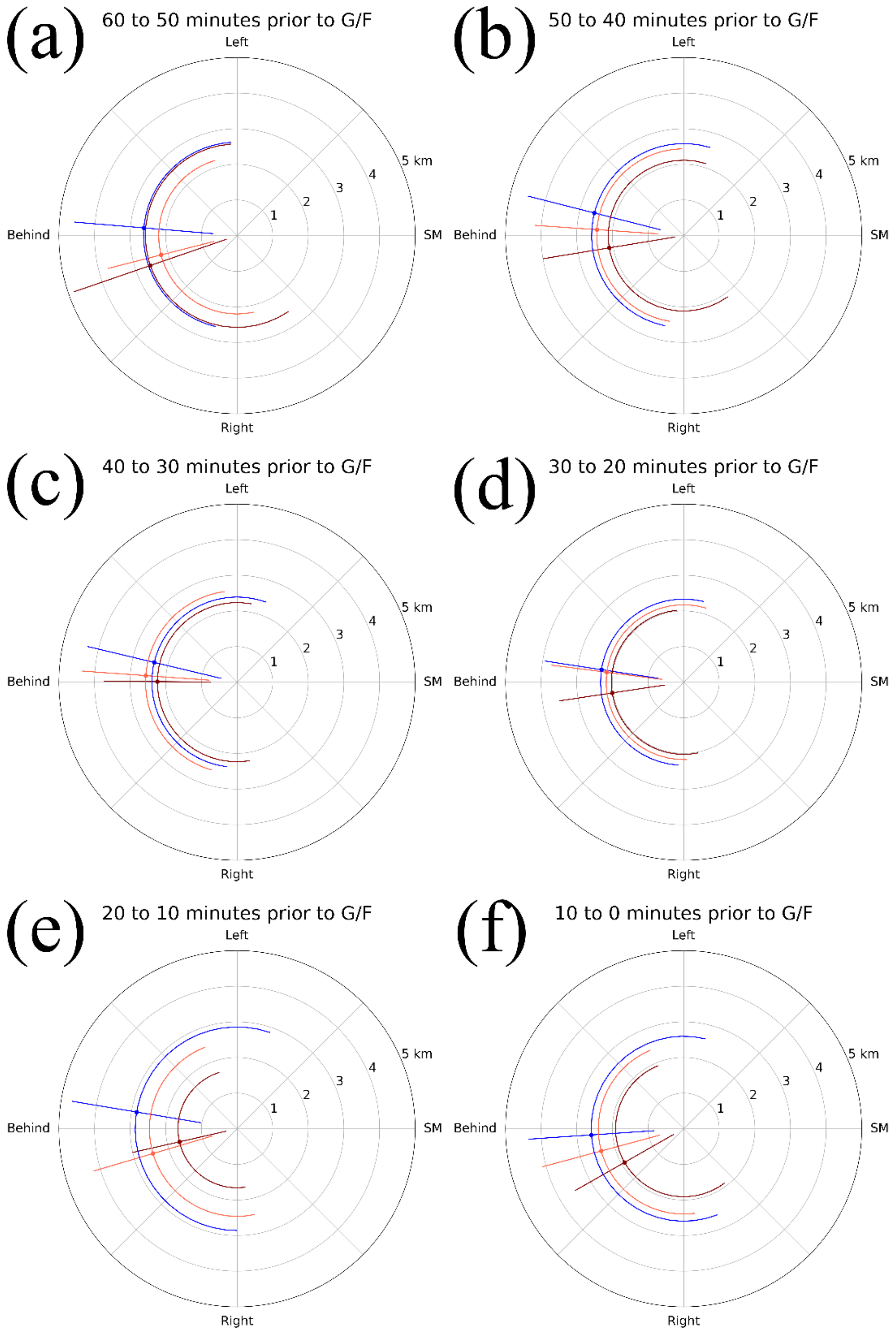

Figure 2.14: Polar plots showing the mean location and direction of the LLM with respect to the MLM (which would be at the origin point). The dark red, light red, and blue dots represent the strongly tornadic, weakly tornadic, and non-tornadic means with the straight (curved) lines representing one standard deviation in range (direction). “SM” represents storm motion.

2.3.4 *Bulk Near Storm Environment Analyses*

One identified control on tornadic potential is the NSE characteristics of air parcels being ingested by supercells. Generally, increasing low-level shear and higher boundary layer moisture/lower LCLs increases tornado likelihood, but no environmental characteristic has been found to be a direct control on this likelihood. To assess the NSEs of each case type, the mean value over the analysis period was taken for each case type for each NSE variable analyzed. The mean values were then analyzed in a bulk sense, with respect to the sub-period to sub-period distribution changes in all LLM layers and the MLM layer, and with respect to continuous mesocyclone durations to identify any NSE characteristic that may exhibit some relationship with the aforementioned variables.

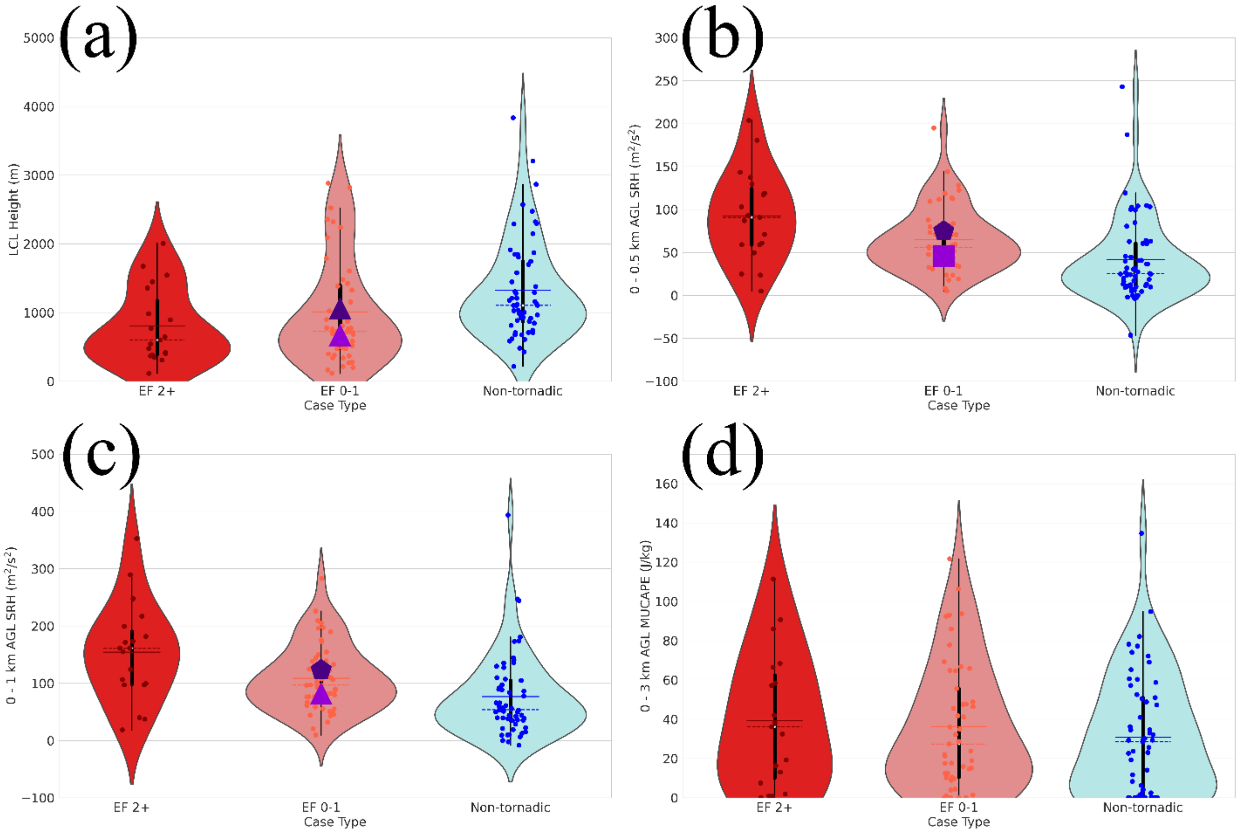

Figure 2.15: Violin plots of the distributions of the case mean (a) surface-based LCL height, (b) 0–500 m AGL SRH, (c) 0–1 km AGL SRH, and (d) 0–3 km AGL MUCAPE for (dark red) strongly tornadic, (light red) weakly tornadic, and (blue) non-tornadic cases. The shapes, and their

respective colors, present on top of some EF 0-1 violin plots represent the same statistical significance outlined in Figure 2.5. The dashed (solid) horizontal lines overlaying each violin plot represent the same values as in Figure 2.8.

Of the NSE variables analyzed, the surface-based LCL height, 0–500 m AGL SRH, and 0–1 km AGL SRH showed the most significant differences between case types, as expected (Fig. 2.15). The surface-based LCL heights for both strongly and weakly tornadic cases were significantly different from non-tornadic LCL heights at 95% confidence. Strongly tornadic cases show the lowest LCL heights overall, but are not significantly different from the weakly tornadic LCLs. Strongly tornadic and weakly tornadic 0–500 m and 0– 1km AGL SRH were significantly different from non-tornadic cases at 99.9% confidence for both SRH distributions and at 99% and 95% confidence for weakly tornadic 0–500 m and 0–1 km AGL SRH, respectively.

While visual differences are apparent between some NSE characteristics, namely the surface-based CAPE, MUCAPE, 0–6 km shear vector magnitude, 0–2 km AGL SRH, and 0–3 km AGL SRH (not shown), significant differences are only present between strongly tornadic and non-tornadic cases. Weakly tornadic cases exhibit substantial distribution overlap with the strongly and non-tornadic NSE characteristic distributions and do not appear to be useful in discriminating between environments that are more or less favorable for strong tornadoes.

Two NSE variables which showed essentially identical distributions between all three case types are the 0–3 km AGL MUCAPE (Fig. 2.15d) and the surface-based CIN (not shown). We identify some visual differences between the case types for these variables (i.e., a slightly lower mean/median 0–3 km AGL MUCAPE in non-tornadic environments), but overall, the distributions show no statistical differences between them.

We also analyzed some variables with the time-normalized change for the four LLM layers and one MLM layer shown in Figures 2.7 and 2.11, respectively, to see if any relationship exists between NSE characteristics and changes seen in the LLMs and MLMs (Fig. 2.16). We used the non-parametric Theil-sen estimator regression technique detailed in the methodology to look for any appreciable and consistent trends in the change in AzShear intensity from one sub-period to the next and the mean NSE that the storm existed in during the analysis period. While the presented analyses focus on the 50-to-40- to 40-to-30-minute change in the MLM compared to the three NSE variables where significant differences were present between both tornadic case types and the non-tornadic cases, the complete analyses were completed for all NSE characteristics for all LLM layers and the MLM layer for all sub-periods prior to G/F. As shown in Fig. 2.16 and for the rest of these analyses, there is no observed relationship between the NSE variables and changes in LLM or MLM intensity.

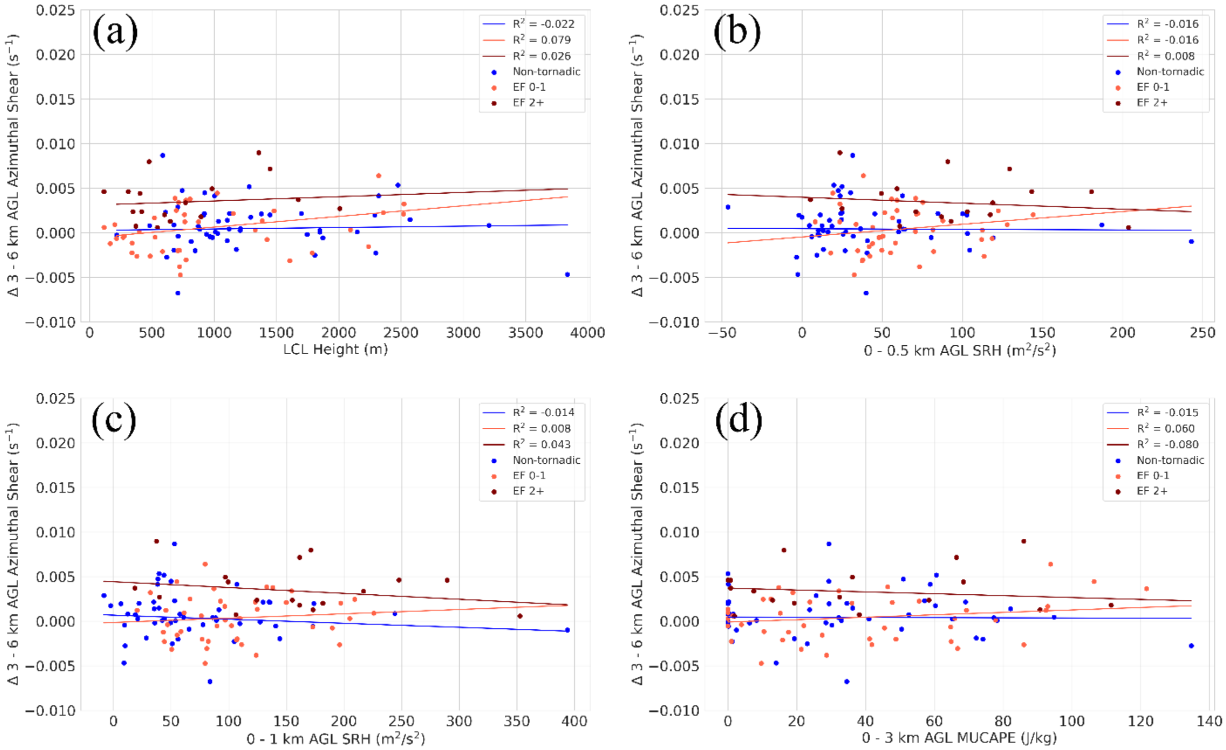

Figure 2.16: Scatter plots with Theil-sen estimator regression lines for the comparison of the 50-to-40- to 40-to-30-minute change in MLM AzShear for (dark red) strongly tornadic, (light red) weakly tornadic, and (blue) non-tornadic cases versus (a) surface-based LCL height, (b) 0–500 m

AGL SRH, (c) 0–1 km AGL SRH, and (d) 0–3 km MUCAPE. R^2 values for each regression line are shown in the legend next to the color of a given case type.

We also examined if NSE characteristics play any role in controlling mesocyclone transience by comparing them with all LLM layers (not shown) and the MLM layer (Fig. 2.17) continuous mesocyclone duration (i.e., Figures 2.8 and 2.12). Again, as with the changes in AzShear, there is no relationship between NSE characteristics and the continuous time prior to G/F that a mesocyclone is present. Some hints of trends appear present, but the R^2 values for any trends are low. Since we are using a blanket threshold of 0.005 s^{-1} for both the LLM and the MLM, and the results from Figure 2.12 suggest that a higher threshold may be needed to parse the differences in MLM continuous duration, there may be some relationship present that is not highlighted by the current methodology. However, we find no evidence that the NSE characteristics play a direct role in the changes in AzShear or the amount of time a mesocyclone is present prior to G/F.

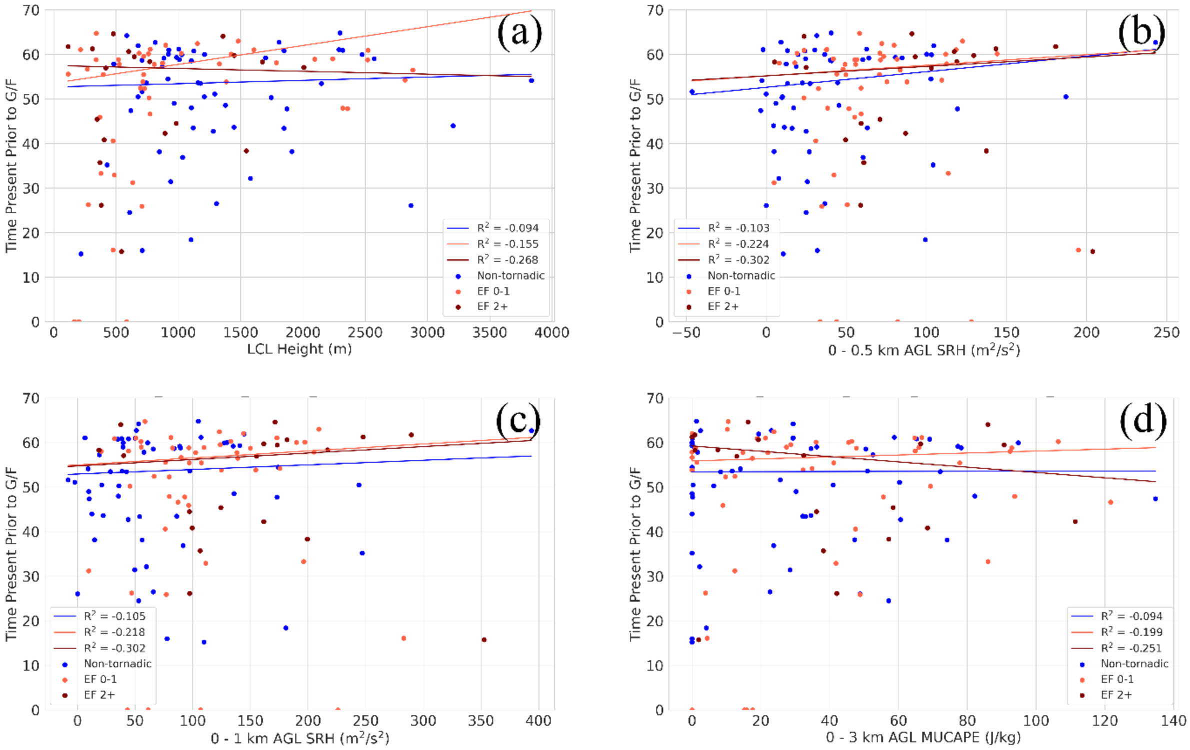

Figure 2.17: As in Fig. 2.16, but for the 3–6 km continuous duration of AzShear above the 0.005 s^{-1} threshold used to investigate mesocyclone transience.

2.3.5 *Threshold Sensitivity Analysis*

The AzShear threshold used in this study was selected from Burgess et al. (1979) and may not be optimal for assessing mesocyclone transience, especially for the MLM (Fig. 2.12). Therefore, we selected four additional threshold values (0.006 s^{-1}, 0.008 s^{-1}, 0.010 s^{-1}, and 0.012 s^{-1}) to evaluate how sensitive the analyses of transience are to the 0.005 s^{-1} threshold.

The 0–500 m layer shows little statistical sensitivity to the various thresholds. The continuous duration of AzShear above a given threshold, both for strongly and weakly tornadic cases, consistently remained significantly different from non-tornadic cases at 95% or greater (not shown). The continuous duration present decreased with increasing threshold values for all case types. Strongly tornadic, weakly tornadic, and non-tornadic mean continuous durations dropped from ~38 minutes, ~35 minutes, and ~22 minutes for the initial 0.005 s^{-1} threshold to ~15 minutes, ~9 minutes, ~4 minutes for the strictest 0.012 s^{-1} threshold, respectively.

Using 0.006 s^{-1} as a threshold for the 0–1 km layer introduces significant differences from non-tornadic continuous durations for both strongly and weakly tornadic cases with a negligible decrease in duration for tornadic cases (Fig. 2.18). Mean continuous durations for strongly and weakly tornadic cases decreases from ~42 minutes and ~43 minutes with the initial threshold to ~40 minutes for both by increasing to 0.006 s^{-1}, whereas non-tornadic mean continuous durations dropped from ~28 minutes to ~22 minutes. Further increasing the threshold improves the significant differences at the expense of continuous duration. Durations for the largest threshold decreased continuous duration to ~18 minutes, ~12 minutes, and ~3 minutes for strongly, weakly, and non-tornadic cases, respectively.

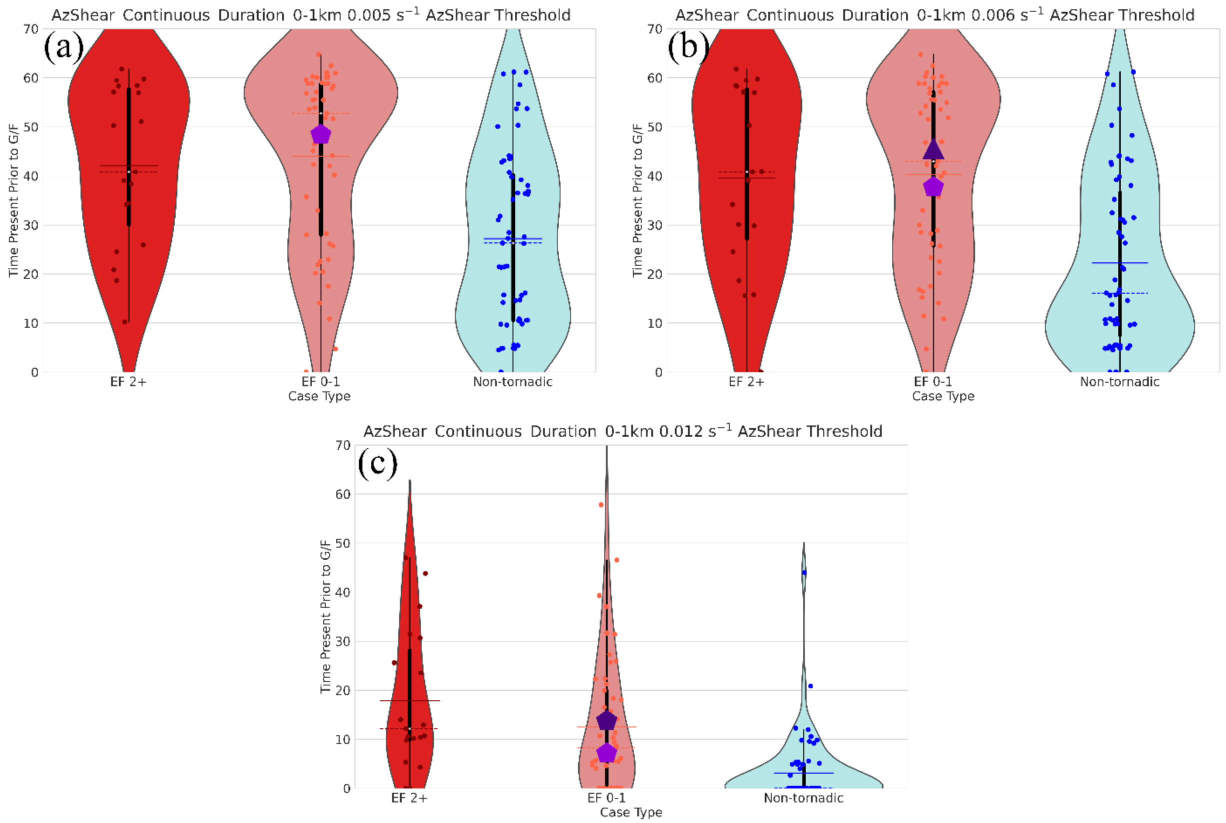

Figure 2.18: As in Fig. 2.8, but only for the 0–1 km layer to investigate AzShear threshold sensitivity for (a) the initial threshold, 0.005 s^{-1}, (b) 0.006 s^{-1}, and (c) 0.012 s^{-1}. Marker shapes and colors overlaying the EF 0-1 violin plots depict the same statistical significance outlined in Fig. 2.5.

Strongly and weakly tornadic cases do not both show significant differences from non-tornadic cases for the 0–2 km and 0–3 km layers until the 0.008 s^{-1} threshold is applied (not shown). However, weakly tornadic cases are significantly different from non-tornadic cases at the 0.005 s^{-1} threshold for the 0–2 km layer and at the 0.006 s^{-1} threshold for the 0–3 km layer. Using the initial threshold, the mean continuous duration for both tornadic case types straddles 50 minutes and ~38 and 45 minutes for 0–2 km and 0–3 km layers of non-tornadic cases. When the 0.008 s^{-1} threshold is applied, the continuous durations drop to ~41/~46 minutes, ~36/~39 minutes, and ~20/~25 minutes for strongly, weakly, and non-tornadic 0–2 km/0–3 km layer.

The MLM is the only layer where strongly tornadic cases are significantly different from both weakly and non-tornadic cases. By applying a sensitivity test, the need for a higher threshold for MLM analysis becomes clear (Fig. 2.19). The only threshold where the continuous duration of the MLM shows any significant differences is when using the 0.012 s^{-1} threshold value. We observe differences among the three distributions beginning with the 0.008 s^{-1} threshold, but they are not significantly different. Applying the 0.012 s^{-1} threshold introduces significant differences in duration between strongly and weakly tornadic cases only, at 95% confidence. The mean continuous durations for the 0.012 s^{-1} threshold are ~29 minutes, ~11 minutes, and ~17 minutes for strongly tornadic, weakly tornadic, and non-tornadic distributions.

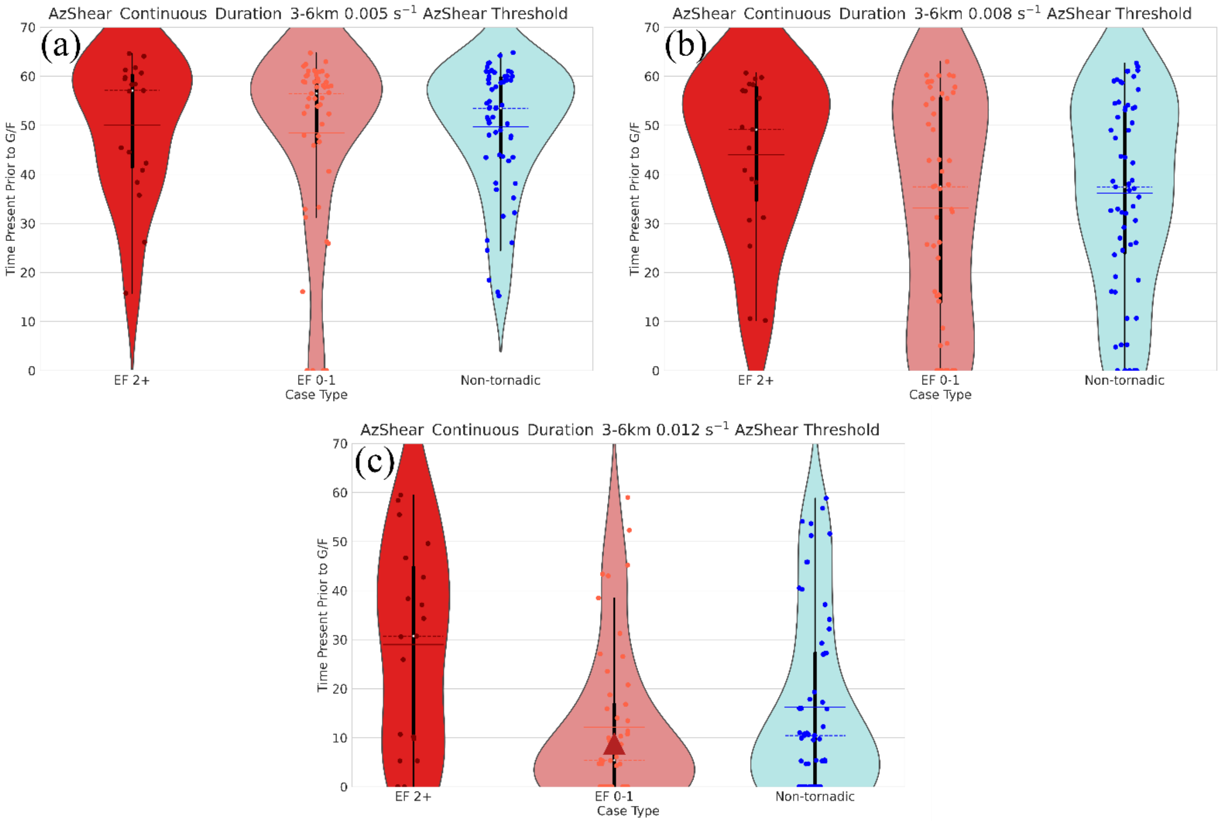

Figure 2.19: As in Fig. 2.17, but for the 3–6 km layer for (a) the initial threshold, 0.005 s^{-1}, (b) 0.008 s^{-1}, and (c) 0.012 s^{-1}.

The 0.012 s^{-1} threshold differentiates between strongly tornadic and weakly/non-tornadic MLM continuous durations better than the other thresholds we applied, so we reinvestigated the NSE using the continuous duration distributions generated from the higher threshold (Fig. 2.20). While strongly and weakly tornadic cases show positive trends in the four NSE variables shown, the R^2 values are low. The weak correlation reinforces the lack of evidence to attribute the transience of mesocyclones directly to specific NSE characteristics.

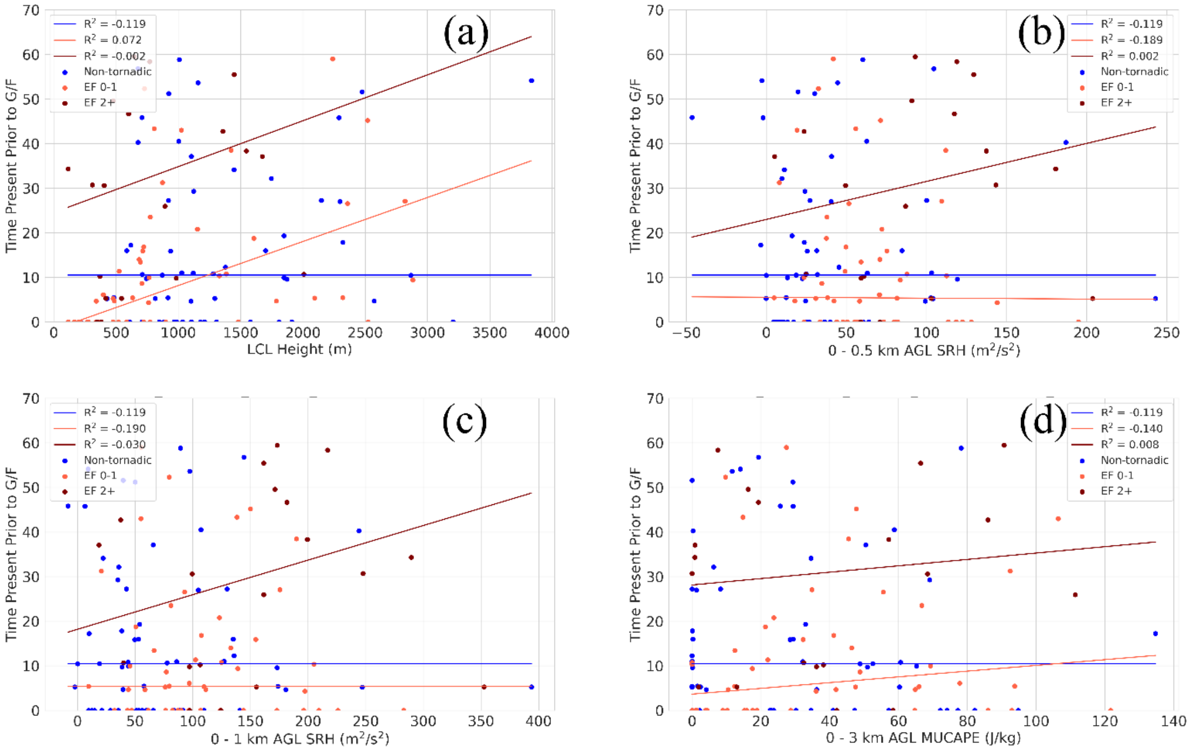

Figure 2.20: As in Fig. 2.17, but for the continuous duration above the 0.012 s^{-1} threshold.

2.4 Summary and Discussion

We investigated the intensity and transience of LLMs and MLMs for the hour period preceding tornadogenesis and tornadogenesis failure for 19 strongly tornadic, 49 weakly tornadic, and 59 non-tornadic supercells. We also compared mesocyclone intensity changes and transience with the mean NSE characteristics of the environments in which these supercells existed to search for any environmental control on the results presented herein. The mesocyclone inclination and separation distances/directions were investigated to elucidate any possible differences between the three case types. Lastly, we analyzed the sensitivity of these results to the AzShear threshold chosen based on a given mesocyclone layer. The key findings from this study are:

1. Strongly tornadic MLMs exhibit a significant increase in intensity between the 50-to-40- and 40-to-30-minute sub-periods, which remains significantly different from weakly and non-tornadic cases for all remaining sub-periods leading up to G/F (Fig. 2.9). The intensity jump in MLMs is not seen in weakly or non-tornadic MLMs and is also not seen in the LLM intensity distributions of any case type (Fig. 2.11). Figure 2.10 shows three example cases. The strongly tornadic case in the example jumped from ~0.008 s^{-1} at ~45 minutes prior to G to ~0.120 s^{-1} at ~35 minutes prior, whereas the weakly tornadic case shows essentially no appreciable change, and the non-tornadic case shows slight weakening between these scans.
2. Strongly tornadic MLMs also tend to be present for longer than both weakly and non-tornadic cases when using a more appropriate AzShear threshold of 0.012 s^{-1} rather than the initial threshold of 0.005 s^{-1} (Fig. 2.19). The 0.005 s^{-1} threshold was particularly poor at highlighting differences in MLM continuous duration as shown in the threshold sensitivity section (Fig. 2.12). While there is considerable separation

shown between strongly and non-tornadic MLM continuous durations, strongly tornadic MLM durations are only significantly different from weakly tornadic cases.

3. Both strongly and weakly tornadic LLM intensity distributions are significantly different from non-tornadic cases for most sub-periods prior to G/F (Fig. 2.5). However, the only periods where strongly and weakly tornadic cases are significantly different is during the last sub-period prior to G, suggesting that, while some distribution separation occurs earlier, LLM intensity between the two tornadic case types remains relatively similar until immediately prior to G. Radar depictions of the described statistical patterns depicted in Fig. 2.6 clearly show the sharp increase in 0–1 km AzShear in the strongly tornadic case, a marginal increase in the weakly tornadic case, and essentially steady state for non-tornadic cases.
4. Non-tornadic LLMs tend to be more transient than either tornadic case type for all layers considered (Figs. 2.8 and 2.18). We tested multiple thresholds on all the layer depths analyzed herein to address the sensitivity of the transience results to a specific AzShear threshold and found that the 0.005 s^{-1} threshold identified in Burgess et al. (1979) worked for 0–500 m AGL AzShear, but was increasingly worse for increasingly thick layers, as noted for MLMs. Thresholds of 0.006 s^{-1}, 0.008 s^{-1}, and 0.008 s^{-1} were found to elucidate differences between the 0–1 km, 0–2 km, and 0–3 km AGL, respectively.
5. The inclination angle (Fig. 2.13) and storm-motion-relative horizontal displacement of the LLM from the MLM (Fig. 2.14) show essentially no difference between case types. While there is some small hint that strongly and non-tornadic cases may exhibit some slight differences in tilt, none are significant, nor are the slighter differences shown in

storm-motion-relative separation distance and direction. However, as mentioned previously, no advection correction was performed on inclination angle or horizontal separation distance/direction and, as such, is subject to considerable errors which may overwhelm any relationship present.

6. While the mean NSE characteristics in which these supercells exist in show some significant differences (namely in surface-based LCL, 0–500 m AGL SRH, and 0–1 km AGL SRH; Fig. 2.15a,b,c), we lack evidence to attribute any NSE characteristic as a control on LLM or MLM intensity changes (Fig. 2.16) or continuous duration (Fig. 2.20). However, the lack of evidence does not mean that no relationship is present, and the presented lack of evidence may be caused by the coarseness of RAP data.

The findings in this study show that, in general, the low-levels show considerable differences between both tornadic case types and non-tornadic cases *while the midlevels exhibit stark differences between strongly tornadic and weakly/non-tornadic cases,* which has not been shown in any previous work that the authors are aware of. The difference between case types appears first in the midlevels and considerably later in the low-levels. Whatever process that may be occurring in the midlevels and causing the differences between strongly tornadic and weakly/non-tornadic MLM intensity, we lack evidence to attribute it to any NSE characteristic or difference in LLM/MLM positioning relative to one another. One interpretation of the results is that the difference in MLM intensity between strongly tornadic and weakly/non-tornadic cases is related to internal storm processes that occur in increasingly more intense tornadic supercells and which are present well before any differences in LLMs are apparent. Another possibility is that the RAP data used in this study does not adequately capture the “true” near-field (e.g., Parker 2014) NSE, and therefore is not able to properly represent whatever NSE characteristic may be controlling this increase in MLM AzShear. To rectify errors introduced by the coarse nature of RAP data, future work should use of HRRR data for NSE characteristic extraction. The higher resolution data provided from HRRR output may highlight more obvious relationships between mesocyclone characteristics and the NSE than the RAP.

The use of SRH, regardless of layer depth, may not sufficiently capture differences between different environments. SRH is dependent on both storm-relative flow and streamwise vorticity. Peters et al. (2020) showed that storm mode is almost exclusively dependent on the storm-relative flow rather than the streamwise vorticity. Streamwise vorticity was found only to have an effect on low-level updrafts and rotation, and had essentially no effect on midlevel rotation regardless of the magnitude of streamwise vorticity. The work presented in Peters et al. (2023) further states that streamwise vorticity acts as the main control on LLM intensity. However, Coffer and Parker (2018) showed a link between higher values of 0–500 m SRH and increasing organized LLMs, as well as higher tornadic potential They also state that, while 0–500m SRH does show the aforementioned link with LLMs and tornadic potential, there does not appear to be a clear demarcation between non-tornadic and tornadic 0–500 m SRH values. Goldacker and Parker (2021) also showed that both 0–500 m SRH and streamwise vorticity are important low-level updraft intensity, but only when environments are favorable for an internal dynamical response between the updraft's rotation and the VPPGA. Since Peters et al. (2023) showed that streamwise vorticity is the most important contributor from SRH, it stands to reason that the primary control on updraft rotation and therefore low-level updraft intensity results from streamwise vorticity. Since streamwise vorticity is not a RAP variable, analysis of it may show stronger relationships with the changes in rotational intensity and transience between the three case types analyzed herein than SRH.

One feature that has received a lot of attention in the literature relative to tornado formation, but that we do not believe plays a role in this MLM intensity increase, is the streamwise vorticity current (SVC; e.g., Orf et al. 2017; Murdzek et al. 2020; Schueth et al. 2021). Recent work has posited the importance of the SVC in supercell rotational intensity, but has been shown to exist for a short period of time prior to G and has also been seen in non-tornadic cases. While its importance in LLM intensity is not investigated, the amount of time prior to G that this MLM AzShear increase is seen is not consistent with observed SVC durations.

While the cause of the sharp increase in MLM intensity shown may be unclear at this point, the physics behind how this process may lead to more intense tornadoes is not. The rapid intensification of MLM rotation during the time prior to G would lead to a sharp drop in the pressure field in midlevels because of the non-linear pressure response in a rotating fluid, which would persist and intensify further in the remaining periods prior to G. A sharp drop in pressure would act to intensify the VPPGF, independent of NSE characteristics, between the low and midlevels. The resulting increase in the strength of the VPPGF would act to intensify the updraft between layers, further acting to tilt and stretch any near surface vorticity present. Analyses of the 0–3 km MUCAPE shows that any difference in updraft intensity may not be directly controlled by the environment because of the striking similarity between all three case type distributions.

In general, strong MLMs (i.e., AzShear ≥ 0.012 s^{-1}) are continuously present for nearly twice as long in strongly tornadic cases than in weakly and non-tornadic cases. The longer continuous duration of MLMs in strongly tornadic cases allows more time for other complex processes, such as the generation of favorable rear-flank downdraft thermodynamics (and therefore buoyancy), the development of a downdraft leading to the enhancement of vortex tilting via the “slippage” (Davies-Jones and Brooks 1993; Dahl et al. 2014), more time to ingest higher near-surface environmentally generated shear (Coffer et al. 2019), etc., necessary for tornadogenesis to occur. LLMs, however, tend to be less transient in strongly and weakly tornadic cases than in non-tornadic cases. In fact, both sets of tornadic LLMs show similar distributions of continuous AzShear duration for all LLM layers when using greater AzShear thresholds. *Overall, we interpret our results to imply that, to form a tornado, a given supercell needs a strong, longer-lived LLM than in a non-tornadic supercell, but to form a strong tornado, a supercell also needs a strong, longer-lived MLM.*

While our study shows that strong rotation develops in the midlevels first, we do not argue against "bottom-up" or "non-descending" tornadogenesis discussed in recent literature (e.g., French et al. 2013; Roberts et al. 2016; Houser et al. 2022). The proposed tornadogenesis processes occur on sub-minute time scales, whereas this study investigates 10-minute sub-periods from WSR-88D data, which has already been shown to have an insufficient temporal resolution to capture tornadogenesis. Instead, based on the results presented herein, we argue that, as speculated in Wakimoto et al. 1998 and Ziegler et al. 2001, tornadogenesis is a "hybrid" process. In this hybrid process, a MLM is already present and an area of near-surface vorticity is ingested immediately preceding tornadogenesis. A stronger MLM would result in a stronger VPPGF, and therefore more tilting and stretching of any near-surface vorticity present. Weakly and non-tornadic cases have MLMs that are generally the same intensity for a given sub-period, but weakly tornadic cases show LLM intensities more similar to strongly tornadic cases for the same sub-period. This discrepancy in LLM and MLM intensity between case types suggests that tornadogenesis, as a whole, is dependent on the low-level rotation, not the midlevels. In this interpretation, weakly tornadic and strongly tornadic storms both ingest areas of stronger near-surface vorticity to generate tornadoes. However, the key difference is the strength of the MLM. We believe that the lack of a strong

MLM, and therefore a strong VPPGF, in weakly tornadic cases acts as a regulator on tornado intensity, and that weakly tornadic events would, therefore, be more similar to hybrid landspout tornado events, rather than strongly tornadic events.

One problem of note is the small number of strongly tornadic cases used in this study. While this is the largest number of strongly tornadic cases investigated in this manner, we still lack a sufficient sample size to properly assess whether the MLM signature is a real pattern or noise of the smaller sample size. Statistical significance testing suggests that they are not, but we plan to add more strongly tornadic cases in the future to further validate or disprove this signature. These results also have not been assessed for their utility in nowcasting tornado potential or intensity, as it is outside the scope of this study. Assuming the stark increase in MLM intensity remains obvious after adding additional strongly tornadic cases, the results presented herein may be useful in assessing probabilities of tornado (or strong tornado) formation.

Chapter 3

Overall Conclusions

The work presented herein is an attempt to address some important unanswered questions about the bulk characteristics of tropospheric convection, one of the many hazards storms can produce, the environments in which they exist, and the relationships (if any) between storm environments and the investigated processes. Part one of this dissertation provided detailed analyses of sea-breeze induced convective cells of various size and the framework for attempting further studies of this kind using similar a similar methodological approach. Climatologies using large observational radar datasets can provide bulk characteristics of different convective cell types in a given region, can be used to directly compare with cloud model output through radar simulators, and can provide information about bulk microphysics if polarimetry is included, among many other uses. This study allows for further investigation into bulk convective characteristics in different regions. However, the thresholds used herein may not be valid for purely continental or maritime convection and changes to the defined thresholds may provide interesting information about how convective characteristics vary by region. Further work should be done using the methodology presented here in different regions to investigate any regional differences which may exist between different convective types.

Part two of this dissertation closely examined the characteristics of LLMs and MLMs in strongly, weakly, and non-tornadic supercells during the hour preceding G/F. Interestingly, we found that the key differentiating factor between strongly tornadic and weakly/non-tornadic cases occurred in the MLM, counter to what we hypothesized. The NSE, while clearly different in certain aspects between case types, does not play an obvious role in the large jump in AzShear in strongly tornadic cases, AzShear between 40 and 30 minutes prior to G, or in how long LLMs or MLMs are continuously present. However, in the future, better model analysis sounding tools may allow for isolating streamwise vorticity from SRH to determine if there is an observational link between it and mesocyclone transience. Our results may help provide insight into a previously unknown process within supercells, but further analyses of strongly tornadic cases are needed to validate or disprove this signal. We have already speculated as to what physical process occurs when the MLM intensification occurs, but the reasoning for this MLM intensification remains unknown.

The mesocyclone analyses would greatly benefit from the use of a tracking algorithm, like the MCIT algorithm, but further algorithms would need to be developed in order to detect the maximum AzShear values occurring only within the hook echo region of supercells automatically. While MCIT can easily detect the supercells we are analyzing, it collects bulk statistics about these cells for a given time step and does not isolate specific regions of the storm for analysis. While outside the scope of this study, future work investigating supercell mesocyclones should consider attempting this type of case selection method to drastically increase the number of cases available.

This dissertation revealed climatological characteristics of different types of convective cells, one of their most detrimental hazards, and the environments in which the cells and their hazards form. The results can be used to evaluate the representativeness of simulated physical processes and help to improve the severe weather prediction. Further studies to assess differences in convection in different regions across the world will lead to better understanding of the convection as a whole. Through the use of radar simulators, the climatologies presented here can be directly compared with model output, allowing for more direct inferences from simulated storms and hazards.

References

Abbott, T. H., and T. W. Cronin, 2021: Aerosol invigoration of atmospheric convection through increases in humidity. *Sci.*, **371**, 83–85, doi:10.1126/science.abc5181.

Amburn, S. A., and P. L. Wolf, 1997: VIL density as a hail indicator. Wea. Forecasting, 12, 473–478, doi: 10.1175/1520-0434(1997)012<0473:VDAAHI>2.0.CO;2.

Beck, J., and C. Weiss, 2013: An assessment of low-level baroclinity and vorticity within a simulated supercell. *Mon. Wea. Rev.*, **141**, 649–669, doi:10.1175/MWR-D-11-00115.1.

Benjamin, S. G., S. S. Weygandt, J. M. Brown, M. Hu, C. R. Alexander, T. G. Smirnova, J. B. Olson, E. P. James, D. C. Dowell, G. A. Grell, H. Lin, S. E. Peckham, T. L. Smith, W. R. Moninger, J. S. Kenyon, and G. S. Manikin, 2016: A North American Hourly Assimilation and Model Forecast Cycle: The Rapid Refresh. *Mon. Wea. Rev.*, **144**, 1669–1694, doi:10.1175/MWR-D-15-0242.1.

Bergemann, M., and C. Jakob, 2016: How important is tropospheric humidity for coastal rainfall in the tropics? *Geophys. Res. Lett.*, **43**, 5860–5868, doi:10.1002/2016GL069255.

Birch, C. E., S. Webster, S. C. Peatman, D. J. Parker, A. J. Matthews, Y. Li, and M. E. E. Hassim, 2016: Scale interactions between the MJO and the western maritime continent. *J. Climate*, 29, 2471–2492, doi:10.1175/JCLI-D-15-0557.1.

Bony, S., B. Stevens, D. M. W. Frierson, C. Jakob, M. Kageyama, R. Pincus, T. G. Shepherd, S. C. Sherwood, A. P. Siebesma, A. H. Sobel, M. Watanabe, and M. J. Webb, 2015: Clouds, circulation, and climate sensitivity. *Nature Geoscience*, **8**, 261–268, doi:10.1038/ngeo2398.

Boyer, C. H., and J. M. L. Dahl, 2020: The mechanisms responsible for large near-surface vertical vorticity within simulated supercells and quasi-linear storms. *Mon. Wea. Rev.*, **148**, 4281–4297, doi:10.1175/MWR-D-20-0082.1.

Brown, M., and C. J. Nowotarski, 2019: The influence of lifting condensation level on low-level outflow and rotation in simulated supercell thunderstorms. *J. Atmos. Sci.*, **76**, 1349–1372, doi:10.1175/JAS-D-18-0216.1.

Burgess, D. W., R. J. Donaldson, T. Sieland, and J. Hinkelman, 1979: Final report on the Joint Doppler Operational Project (JDOP 1976–1978). Part I: Meteorological applications. NOAA Tech. Memo. ERL NSSL-86, NOAA, 84 pp.

Chavas, D. R., and D. T. Dawson II, 2021: An idealized physical model for the severe convective storm environmental sounding. *J. Atmos. Sci.*, **78**, 653–670, doi:10.1175/JAS-D-20-0120.1.

Chrisman, J. N., 2009: Automated Volume Scan Evaluation and Termination (AVSET)—A simple technique to achieve faster volume scan updates. 34th Conf. on Radar Meteorology, Williamsburg, VA, Amer. Meteor. Soc., P4.4, https://ams.confex.com/ams/34Radar/techprogram/paper_155324.htm.

Chrisman, J. N., 2013: Dynamic scanning. NEXRAD Now, 22, 1–3, https://www.roc.noaa.gov/WSR88D/PublicDocs/NNOW/NNow22c.pdf.

Chrisman, J. N., 2014: Multiple elevation scan option for SAILS (MESO-SAILS)—The next step in dynamic scanning for the WSR-88D. Radar Operations Center, 27 pp., https://www.roc.noaa.gov/wsr88d/PublicDocs/NewTechnology/MESO-SAILS_Description_Briefing_Jan_2014.pdf.

Chrisman, J. N., 2016: Mid-volume rescan of low-level elevations (MRLE): A new approach to enhance sampling of quasi-linear convective systems (QLCSs). New Radar Technologies Web Page, NOAA/NWS/Radar Operations Center, 21 pp., https://www.roc.noaa.gov/WSR88D/PublicDocs/NewTechnology/DQ_QLCS_MRLE_June_2016.pdf.

Coffer, B. E., and M. D. Parker, 2017: Simulated supercells in nontornadic and tornadic VORTEX2 environments. *Mon. Wea. Rev.*, **145**, 149–180, doi:10.1175/MWR-D-16-0226.1.

Coffer, B. E., M. D. Parker, J. M. L. Dahl, L. J. Wicker, and A. J. Clark, 2017: Volatility of tornadogenesis: An ensemble of simulated nontornadic and tornadic supercells in VORTEX2 environments. *Mon. Wea. Rev.*, **145**, 4605–4625, doi:10.1175/MWR-D-17-0152.1.

Coffer, B. E., and M. D. Parker, 2018: Is there a “tipping point” between simulated nontornadic and tornadic supercells in VORTEX2 environments? *Mon. Wea. Rev.*, **146**, 2667–2693, doi:10.1175/MWR-D-180050.1.

Coffer, B. E., M. D. Parker, L. Thompson, B. T. Smith, and R. E. Jewell, 2019: Using near-ground storm relative helicity in supercell tornado forecasting. *Wea. Forecasting*, **34**, 1417–1435, doi:10.1175/WAF-D-19-0115.1.

Coffer, B. E., M. D. Parker, J. M. Peters, A. R. Wade, 2023: Supercell low-level mesocyclones: Origins of inflow and vorticity. *Mon. Wea. Rev.*, **151**, 2205–2232, doi:10.1175/MWR-D-22-0269.1.

Colin, M., and S. C. Sherwood, 2021: Atmospheric convection as an unstable predator-pray process with memory. *J. Atmos. Sci.*, **78**, 3781–3797, doi:10.1175/JAS-D-20-0337.1.

Crum, T. D. and R. L. Alberty, 1993: The WSR-88D and the WSR-88D operational support facility. *Bull. Amer. Meteor. Soc.*, **74**, 1669–1688, doi: 10.1175/1520-0477(1993)074<1669:TWATWO>2.0.CO;2.

Dahl, J. M. L., M. D. Parker, and L. J. Wicker, 2014: Imported and storm-generated near-ground vertical vorticity in a simulated supercell. *J. Atmos. Sci.*, **71**, 3027–3051, doi:10.1175/JAS-D-13-0123.1.

Davies-Jones, R. P., 1984: Streamwise vorticity: The origin of updraft rotation in supercell storms. *J. Atmos. Sci.*, **41**, 2991–3006, doi:10.1175/1520-0469(1984)041<2991:SVTOOU>2.0.CO;2.

Davies-Jones, R., and H. E. Brooks, 1993: Mesocyclogenesis from a theoretical perspective. *The Tornado: Its Structure, Dynamics, Prediction, and Hazards, Geophys. Monogr.*, No. 79, Amer. Geophys. Union, 105–114.

Doswell, C. A., III, and Burgess D. W., 1993: Tornadoes and tornadic storms: A review of conceptual models. *The Tornado: Its Structure, Dynamics, Prediction and Hazards, Geophys. Monogr.*, **79**, Amer. Geophys. Union, 161–172, doi:10.1029/GM079p0161.

Dowell, D. C., C. R. Alexander, E. P. James, S. S. Weygandt, S. G. Benjamin, G. S. Manikin, B. T. Blake, J. M. Brown, J. B. Olson, M. Hu, T. G. Smirnova, T. Ladwig, J. S. Kenyon, R. Ahmadov, D. D. Turner, J. D. Duda, and T. I. Alcott, 2022: The High-Resolution Rapid Refresh (HRRR): An hourly updating convection-allowing forecast model. Part I: Motivation and system description. *Wea. Forecasting*, **37**, 1371–1395, doi:10.1175/WAF-D-21-0151.1.

Dunn, O. J., 1964: Multiple comparisons using rank sums. *Technometrics*, **6**, 241–252, doi: 10.1080/00401706.1964.10490181.

Edwards, R., J. G. LaDue, J. T. Ferree, K. Scharfenberg, C. Maier, and W. L. Coulbourne, 2013: Tornado Intensity Estimation: Past, Present, and Future. *Bull. Amer. Meteor. Soc.*, **94**, 641–653, doi:10.1175/BAMS-D-11-00006.1.

Fan, J., D. Rosenfeld, Y. Zhang, S. E. Giangrande, Z. Li, L. A. T. Machado, S. T. Martin, Y. Yang, J. Wang, P. Artaxo, H. M. J. Barbosa, R. C. Braga, J. M. Comstock, Z. Feng, W. Gao, H. B. Gomes, F. Mei, C. Pöhlker, U. Pöschl, and R. A. F. De Souza, 2018: Substantial convection and precipitation enhancements by ultrafine aerosol particles. *Sci.*, **359**, 411–418, doi:10.1126/science.aan8461.

Fischer, J., and J. M. L. Dahl, 2020: The relative importance of updraft and cold pool characteristics in supercell tornadogenesis using highly idealized simulations. *J. Atmos. Sci.*, **77**, 4089–4107, doi:10.1175/JAS-D-20-0126.1.

French, M. M., H. B. Bluestein, I. PopStefanija, C. Baldi, and R. T. Bluth. 2013: Reexamining the vertical development of tornadic vortex signature in supercells. *Mon. Wea. Rev.*, **141**, 4576–4601, doi:10.1175/MWR-D-12-00315.1.

French, M. M., H. B. Bluestein, I. PopStefanija, C. Baldi, and R. T. Bluth. 2014: Mobile, phased-array Doppler radar observations of tornadoes at X band. *Mon. Wea. Rev.*, **142**, 1010–1036, doi:10.1175/MWR-D-13-00101.1.

French, M. M., W. Burgess, E. R. Mansell, and L. J. Wicker, 2015: Bulk hook echo raindrop sizes retrieved using mobile, polarimetric Doppler radar observations. *J. Appl. Meteor. Climatol.*, **54**, 423–450, doi:10.1175/JAMC-D-14-0171.1.

French, M. M., and D. M. Kingfield, 2019: Dissipation characteristics of tornadic vortex signatures associated with long-duration tornadoes. *J. Appl. Meteor. Climatol.*, **58**, 317–339, doi:10.1175/JAMC-D-18-0187.1.

Fridlind, A. M., X. Li, D. Wu, M. van Lier-Walqui, A. S. Ackerman, W. Tao, G. M. McFarquhar, W. Wu, X. Dong, J. Wang, A. Ryzhkov, P. Zhang, M. R. Poellot, A. Neumann, and J. M. Tomlinson, 2017: Derivation of aerosol profiles for MC3E convection studies and use in simulations of the 20 May squall line case. *Atmos. Chem. Phys.*, **17**, 5947–5972, doi:10.5194/acp-17-5947-2017.

Fridlind, A. M., M. van Lier-Walqui, S. Collis, S. E. Giangrande, R. C. Jackson, X. Li, T. Matsui, R. Orville, M. H. Picel, D. Rosenfeld, A. Ryzhkov, R. Weitz, and P. Zhang, 2019: Use of polarimetric radar measurements to constrain simulated convective cell evolution: a pilot study with Lagrangian tracking. *Atmos. Meas. Tech.*, **12**, 2979–3000, doi:10.5194/amt-12-2979-2019.

Gagin, A., D. Rosenfeld and R. E. Lopez, 1985: The relationship between height and precipitation characteristics of summertime convective cells in south Florida. *J. Atmos. Sci.*, **42**, 84–94.

Goldacker, N. A., and M. D. Parker, 2021: Low-level updraft intensification in response to environmental wind profiles. *J. Atmos. Sci.*, **78**, 2763–2781, doi:10.1175/JAS-D-20-0354.1.

Grabowski, W. W., and H. Morrison, 2021: Supersaturation, buoyancy, and deep convection dynamics. *Atmos. Chem. Phys.*, **21**, 13997–14018, doi:10.5194/acp-21-13997-2021.

Greene, D. R., and R. A. Clark, 1972: Vertically Integrated Liquid Water – A new analysis tool. *Mon. Wea. Rev.*, **100**, 548–552, doi:10.1175/1520-0493(1972)100<0548:VILWNA>2.3.CO;2.

Grzych, M. L., B. D. Lee, and C. A. Finley, 2007: Thermodynamic analysis of supercell rear-flank downdrafts from Project ANSWERS. *Mon. Wea. Rev.*, **135**, 240–246, doi:10.1175/MWR3288.1.

Guarriello, F., C. J. Nowotarski, and C. C. Epifanio, 2018: Effects of the low-level wind profile on outflow position and near-surface vertical vorticity in simulated supercell thunderstorms. *J. Atmos. Sci.*, **75**, 731–753, doi:10.1175/JAS-D-17-0174.1.

Haurwitz, B., 1947: Comments on the sea-breeze circulation. *J. Atmos. Sci.*, **4**, 1–8, doi:10.1175/1520-0469(1947)004<0001:COTSBC>2.0.CO;2.

Hitschfeld, W., 1960: The motion and erosion of convective storms in severe vertical wind shear. *J. Atmos. Sci.*, **17**, 270–282, doi:10.1175/1520-0469(1960)017<0270:TMAEOC>2.0.CO;2.

Houser, J. L., H. B. Bluestein, K. Thiem, J. Snyder, D. Reif, and Z. Wienhoff, 2022: Additional evaluation of the spatiotemporal evolution of rotation during tornadogenesis using rapid-scan mobile radar observations. *Mon. Wea. Rev.*, **150**, 1639–1666, doi:10.1175/MWR-D-21-0227.1.

Hu, J., D. Rosenfeld, D. Zrnic, E. Williams, P. Zhang, J. C. Snyder, A. Ryzhkov, E. Hashimshoni, R. Zhang, and R. Weitz, 2019a: Tracking and characterization of convective cells through their maturation into stratiform storm elements using polarimetric radar and lightning detection. *J. Atmos. Res.*, **226**, 192–207, doi:10.1016/j.atmosres.2019.04.015.

Hu, J., D. Rosenfeld, A. Ryzhkov, D. Zrnic, E. Williams, P. Zhang, J. C. Snyder, R. Zhang, and R. Weitz, 2019b: Polarimetric radar convective cell tracking reveals large sensitivity to cloud precipitation and electrification properties of CCN. *J. Geophys. Res. Atmos.*, **124**, 12194–12205, doi:10.1029/2019jd030857.

Igel, A. L., M. R. Igel, and S. C. van den Heever, 2015: Make it a double? Sobering results from simulations using single-moment microphysics schemes. *J. Atmos. Sci.*, **72**, 910–925, doi:10.1175/JAS-D-14-0107.1.

Igel, A. L., and S. C. van den Heever, 2021: Invigoration or enervation of convective clouds by aerosols? *Geophys. Res. Lett.*, **48**, e2021GL093804, doi:10.1029/2021GL093804.

James, E. P., C. R. Alexander, D. C. Dowell, S. S. Weygandt, S. G. Benjamin, G. S. Manikin, J. M. Brown, J. B. Olson, M. Hu, T. G. Smirnova, T. Ladwig, J. S. Kenyon, and D. D. Turner, 2022: The High-Resolution Rapid Refresh (HRRR): An hourly updating convection-allowing forecast model. Part II: Forecast performance. *Wea. Forecasting*, **37**, 1397–1417, doi:10.1175/WAF-D-21-0130.1.

Jensen, M. P., J. H. Flynn, L. M. Judd, P. Kollias, C. Kuang, G. Mcfarquhar, R. Nadkarni, H. Powers, and J. Sullivan, 2022: A succession of cloud, precipitation, aerosol, and air quality field experiments in the coastal urban environment. *Bull. Amer. Meteor. Soc.*, **103**, 103–105, doi:10.1175/BAMS-D-21-0104.1.

Kerr, C. A., D. J. Stensrud, and X. Wang, 2019: Diagnosing convective dependencies on near-storm environments using ensemble sensitivity analyses. *Mon. Wea. Rev.*, **147**, 495–517, doi:10.1175/MWR-D-18-0140.1.

Kingfield, D. M., and J. G. LaDue, 2015: The relationship between automated low-level velocity calculations from the WSR-88D and maximum tornado intensity determined from damage surveys. *Wea. Forecasting*, **30**, 1125–1139, doi:10.1175/WAF-D-00096.1.

Kingfield, D. M., K. M. Calhoun, K. M. de Beurs, and G. M. Henebry, 2018: Effects of city size on thunderstorm evolution revealed through a multiradar climatology of the central United States. *J. Appl. Meteor. Climatol.*, **57**, 295–317, doi:10.1175/JAMC-D-16-0341.1.

Kollias, P., E. Luke, M. Oue, and K. Lamer, 2020: Agile adaptive radar sampling of fast-evolving atmospheric phenomena guided by satellite imagery and surface cameras. *Geophys. Res. Lett.*, **47**, e2020GL088440, doi:10.1029/2020GL088440.

Kruskal, W. H., and A. Wallis, 1952: Use of ranks in one-criterion variance analysis. *J. Amer. Stat. Assoc.*, **47**, 583–621, doi:10.2307/2280779.

Kumjian, M. R., and A. V. Ryzhkov, 2008: Microphysical differences between tornadic and non-tornadic supercell rear-flank downdrafts revealed by dual-polarization radar measurements. Preprints, *24th Conf. on Severe Local Storms*, Savannah, GA, Amer. Meteor. Soc., 3B.4. [Available online at https://ams.confex.com/ams/pdfpapers/141912.pdf.]

Kumjian, M. R., 2011: Precipitation properties of supercell hook echoes. *Electron. J. Severe Storms Meteor.*, **6** (5). [Available online at http://ejssm.org/ojs/index.php/ejssm/article/viewArticle/93.]

Kumjian, M. R., Z. J. Lebo, and A. M. Ward, 2019: Storms producing large accumulations of small hail. *J. Appl. Meteor. Climatol.*, **58**, 341–364, doi:10.1175/JAMC-D-18-0073.1.

Ladino, L. A., A. Korolev, I. Heckman, M. Wolde, A. M. Fridlind, and A. S. Ackerman, 2017: On the role of ice-nucleating aerosol in the formation of ice particles in tropical mesoscale convective systems. *Geophys. Res. Lett.*, **44**, 1574–1582, doi:10.1002/2016GL072455.

Lamer, K., P. Kollias, E. P. Luke, B. P. Treserras, M. Oue, and B. Dolan, 2023: Multisensor agile adaptive sampling (MAAS): a methodology to collect radar observations of convective cell lifecycle. *J. Atmos. Oceanic Technol.*, doi:10.1175/JTECH-D-23-0043.1.

Lebo, Z. J., and J. H. Seinfeld, 2011: Theoretical basis for convective invigoration due to increased aerosol concentration. *Atmos. Chem. Phys.*, **11**, 5407–5429, doi:10.5194/acp-11-5407-2011.

Lebo, Z. J., 2018: A numerical investigation of the potential effects of aerosol-induced warming and updraft width and slope on updraft intensity in deep convective clouds. *J. Atmos. Sci.*, **75**, 535–554, doi:10.1175/JAS-D-16-0368.1.

Lee, M., S. D. Schubert, M. J. Suarez, J. E. Schemm, H. Pan, J. Han, and S. Yoo, 2008: Role of convection triggers in the simulations of the diurnal cycle of precipitation over the United States Great Plains in a general circulation model. *J. Geophys. Res. Atmos.*, **113**, D02111, doi:10.1029/2007JD008984.

Mahalik, M. C., B. R. Smith, K. L. Elmore, D. M. Kingfield, K. L. Ortega, and T. M. Smith, 2019: Estimates of Gradients in Radar Moments Using a Linear Least Squares Derivative Technique. *Wea. Forecasting*, **34**, 415–434, doi:10.1175/WAF-D-18-0095.1.

Mann, H. B., and D. R. Whitney, 1947: On a test of whether one of two random variables is stochastically larger than the other. *Ann. Math. Stat.*, **18**, 50–60, doi:10.1214/aoms/1177730491.

Markowski, P. M., J. M. Straka, and E. N. Rasmussen, 2002: Direct surface thermodynamic observations within the rear-flank downdrafts of nontornadic and tornadic supercells. *Mon. Wea. Rev.*, **130**, 1692–1721, doi:10.1175/1520-0493(2002)130<1692:DSTOWT>2.0.CO;2.

Markowski, P. M., Y. Richardson, E. Rasmussen, J. Straka, R. Davies-Jones, and R. J. Trapp, 2008: Vortex lines within low-level mesocyclones obtained from pseudo-dual-Doppler radar observations. *Mon. Wea. Rev.*, **136**, 3513–3535, doi:10.1175/2008MWR2315.1.

Markowski, P. M., M. Majcen, Y. Richardson, J. Marquis, and J. Wurman, 2011: Characteristics of the wind field in three nontornadic low-level mesocyclones observed by the Doppler on

Wheels radars. *Electron. J. Severe Storms Meteor.*, **6** (3). [Available online at http://www.ejssm.org/ojs/index.php/ejssm/article/viewArticle/75.]

Markowski, P. M., Y. Richardson. J. Marquis, R. Davies-Jones, J. Wurman, K. Kosiba, P. Robinson, E. Rasmussen, and D. Dowell, 2012: The pretornadic phase of the Goshen County, Wyoming, supercell of 5 June 2009 intercepted by VORTEX2. Part II: Intensification of low-level rotation. *Mon. Wea. Rev.*, **140**, 2916–2938, doi:10.1175/MWR-D-11-00337.1.

Markowski, P. M., and Y. P. Richardson, 2014: The influence of environmental low-level shear and cold pools on tornadogenesis: insights from idealized simulations. *J. Atmos. Sci.*, **71**, 243–275, doi:10.1175/JAS-D-13-0159.1.

Markowski, P. M., 2016: An idealized numerical simulation investigation of the effects of surface drag on the development of near-surface vertical vorticity in supercell thunderstorms. *J. Atmos. Sci.*, **73**, 4349–4385, doi:10.1175/JAS-D-16-0150.1.

Markowski, P. M., 2020: What is the intrinsic predictability of tornadic supercell thunderstorms? *Mon. Wea. Rev.*, **148**, 3157–3180, doi:10.1175/MWR-D-20-0076.1.

Marquis, J., Y. Richardson, P. Markowski, J. Wurman, K. Kosiba, and P. Robinson, 2016: An investigation of the Goshen County, Wyoming, tornadic supercell of 5 June 2009 using EnKF assimilation of mobile mesonet and radar observations collected during VORTEX2. Part II: Mesocyclone-scale processes affecting tornado formation, maintenance, and decay. *Mon. Wea. Rev.*, **144**, 3441–3463, doi:10.1175/MWR-D-15-0411.1.

Mashiko, W., 2016: A numerical study of the 6 May 2012 Tsukuba City supercell tornado. Part II: Mechanisms of tornadogenesis. *Mon. Wea. Rev.*, **144**, 3077–3098, doi:10.1175/MWR-D-15-0122.1.

Miller, M. L., V. Lakshmanan, and T. M. Smith, 2013: An automated method for depicting mesocyclone paths and intensities. *Wea. Forecasting*, **28**, 570–585, doi:10.1175/WAF-D-12-00065.1.

Mulholland, J. P, S. W. Nesbitt, R. J. Trapp, K. L. Rasmussen, and P. V. Salio, 2018: Convective storm life cycle and environments near the Sierras de Córdoba, Argentina. *Mon. Wea. Rev.*, **146**, 2541–2557, doi:10.1175/MWR-D-18-0081.1.

Murdzek, S. S., P. M. Markowski, Y. P. Richardson, 2020: Simultaneous dual-Doppler and mobile mesonet observations of streamwise vorticity currents in three supercells. *Mon. Wea. Rev.*, **148**, 4859–4874, doi:10.1175/MWR-D-20-0239.1.

Orf, L., R. Wilhelmson, B. Lee, C. Finley, and A. Houston, 2017: Evolution of a long-track violent tornado within a simulated supercell. *Bull. Amer. Meteor. Soc.*, **98**, 45–68, doi:10.1175/BAMS-D-15-00073.2.

Oue, M., A. Tatarevic, P. Kollias, D. Wang, K. Yu, and A. M. Vogelmann, 2020: The Cloud Resolving Model Radar Simulator (CR-SIM) version 3.2: Description and applications of a virtual observatory. *Geosci. Model Dev.*, **13**, 1975–1998, doi:10.5194/gmd-13-1975-2020.

Oue, M., S. M. Saleeby, P. J. Marinescu, P. Kollias, and S. C. van den Heever, 2022: Optimizing radar scan strategies for tracking isolated deep convection using observing system simulation experiments. *Atmos. Meas. Tech.*, **15**, 4931–4950, doi:10.5194/amt-15-4931-2022.

Park, J. M., S. C. van den Heever, A. L. Igel, L. D. Grant, J. S. Johnson, S. M. Saleeby, S. D. Miller, and J. S Reid, 2020: Environmental controls on tropical sea breeze convection and resulting aerosol redistribution. *J. Geophys. Res. Atmos.*, **125**, e2019JD031699, doi:10.1029/ 2019JD031699.

Parker, M. D., 2014: Composite VORTEX2 supercell environments from near-storm soundings. *Mon. Wea. Rev.*, **142**, 508–529, doi:10.1175/MWR-D-13-00167.1.

Parker, M. D., and J. M. L. Dahl, 2015: Production of near-surface vertical vorticity by idealized downdrafts. *Mon. Wea. Rev.*, **143**, 2795–2816, doi:10.1175/MWR-D-14-00310.1.

Peters, J. M., C. J. Nowotarski, and J. P. Mulholland, 2020: The influences of effective inflow layer streamwise vorticity and storm-relative flow on supercell updraft properties. *J. Atmos. Sci.*, **77**, 3033–3057, doi:10.1175/JAS-D-19-0355.1.

Peters, J. M., B. E. Coffer, M. D. Parker, C. J. Nowotarski, J. P. Mulholland, C. J. Nixon, and J. T. Allen, 2023: Disentangling the influences of storm-relative flow and horizontal streamwise vorticity on low-level mesocyclones in supercells. *J. Atmos. Sci.*, **80**, 129–149, doi:10.1175/JAS-D-22-0114.1.

Peters, K., C. Hohenegger, and D. Klocke, 2019: Different representation of mesoscale convective systems in convection-permitting and convection-parameterizing NWP models and its implications for large-scale forecast evolution. *Atmos.*, **10**, 503, doi:10.3390/atmos10090503.

Pratt, J., 1959: Remarks on zeros and ties in the Wilcoxon signed rank procedures. *J. Amer. Stat. Assoc.*, **54**, 655–667, doi:10.1080/01621459.1959.10501526.

Pulkkinen, S., D. Nerini, A. Perez Hortal, C. Velasco-Forero, U. Germann, A. Seed, and L. Foresti, 2019a: pysteps - a community-driven open-source library for precipitation nowcasting. *Poster presented at the 3rd European Nowcasting Conference*, Madrid, ES. doi: 10.13140/RG.2.2.31368.67840.

Pulkkinen, S., D. Nerini, A. Perez Hortal, C. Velasco-Forero, U. Germann, A. Seed, and L. Foresti, 2019b: Pysteps: an open-source Python library for probabilistic precipitation nowcasting (v1.0). *Geosci. Model Dev.*, **12**, 4185–4219. doi:10.5194/gmd-12-4185-2019.

Radar Operations Center, 2015: WSR-88D Volume Coverage Pattern (VCP) improvement initiatives. New Radar Technologies Web Page, NOAA/NWS/Radar Operations Center, 8pp., https://www.roc.noaa.gov/WSR88D/PublicDocs/NewTechnology/New_VCP_Paradigm_Public_Oct_2015.pdf.

Radar Operations Center, 2022: NEXRAD technical information. NEXRAD Technical Information Web Page, NOAA/NWS/Radar Operations Center, https://www.roc.noaa.gov/WSR88D/Engineering/NEXRADTechInfo.aspx.

Roberts, B., M. Xue, A. D. Schenkman, and D. T. Dawson II, 2017: The role of surface drag in tornadogenesis within an idealized supercell simulation. *J. Atmos. Sci.*, **73**, 3371–3395, doi:10.1175/JAS-D-15-0332.1.

Roberts, B., and M. Xue, 2017: The role of surface drag in mesocyclone intensification leading to tornadogenesis within an idealized supercell simulation. *J. Atmos. Sci.*, **74**, 3055–3077, doi:10/1175/JAS-D-16-0364.1.

Roberts, B., M. Xue, and D. T. Dawson II, 2020: The effect of surface drag strength on mesocyclone intensification and tornadogenesis in idealized supercell simulations. *J. Atmos. Sci.*, **77**, 1699–1721, https://doi.org/10.1175/JAS-D-19-0109.1.

Rosenfeld, D., 1987: Objective method for analysis and tracking of convective cells as seen by radar. *J. Atmos. Oceanic Technol.*, **4**, 422–434.

Rosenfeld, D., Y. Zheng, E. Hashimshoni, M. L. Pöhlker, A. Jefferson, C. Pöhlker, X. Yu, Y. Zhu, G. Liu, Z. Yue, B. Fischman, Z. Li, D. Giguzin, T. Goren, P. Artaxo, H. M. J. Barbosa, U.

Pöschl, and M. O. Andreae, 2016: Satellite retrieval of cloud condensation nuclei concentrations by using clouds as CCN chambers. *Proc. Natl. Acad. Sci. USA*, **113**, 5828–5834, doi:10.1073/pnas.1514044113.

Rotunno, R., 1983: On the linear theory of the land and sea breeze. *J. Atmos. Sci.*, **40**, 1999–2009, doi:10.1175/1520-0469(1983)040<1999:OTLTOT>2.0.CO;2.

Rotunno, R., and Klemp J., 1985: On the rotation and propagation of simulated supercell thunderstorms. *J. Atmos. Sci.*, **42**, 271–292, doi: 10.1175/1520-0469(1985)042%3C0271:OTRAPO%3E2.0.CO;2.

Ryzhkov, A. V., T. J. Schuur, D. W. Burgess, and D. S. Zrnic, 2005: Polarimetric tornado detection. *J. Appl. Meteor. Climatol.*, **44**, 557–570, doi:10.1175/JAM2235.1.

Ryzhkov, A. V., M. Pinsky, A. Pokrovsky, and A. Khain, 2011: Polarimetric radar observation operator for a cloud model with spectral microphysics. *J. Appl. Meteor. Climatol.*, **50**, 873–894, doi:10.1175/2010JAMC2363.1.

Schenkman, A. D., M. Xue, and M. Hu, 2014: Tornadogenesis in a high-resolution simulation of the 8 May 2003 Oklahoma City supercell. *J. Atmos. Sci.*, **71**, 130–154, doi:10.1175/JAS-D-13-073.1.

Schenkman, A. D., M. Xue, and D. T. Dawson II, 2016: The cause of internal outflow surges in a high-resolution simulation of the 8 May 2003 Oklahoma City tornadic supercell. *J. Atmos. Sci.*, **73**, 353–370, doi:10.1175/JAS-D-15-0112.1.

Schueth, A., C. Weiss, and J. M. L. Dahl, 2021: Comparing observations and simulations of the streamwise vorticity current and the forward-flank convergence boundary in a supercell storm. *Mon. Wea. Rev.*, **149**, 1651–1671, doi:10.1175/MWR-D-20-0251.1.

Sen, P. K., 1968: Estimates of the regression coefficient based on Kendall's tau. *J. Amer. Stat. Assoc.*, **63**, 1379–1389, doi:10.1080/01621459.1968.10480934.

Sessa, M. F., and R. J. Trapp, 2020: Observed relationship between tornado intensity and pretornadic mesocyclone characteristics. *Wea. Forecasting*, **35**, 1243–1261, doi:10.1175/WAF-D-19-0099.1.

Sheffield, A. M., S. M. Saleeby, and S. C. van den Heever, 2015: Aerosol-induced mechanisms for cumulus congestus growth. *J. Geophys. Res. Atmos.*, **120**, 8941–8952, doi:10.1002/2015JD023743.

Skinner, P. S., C. C. Weiss, M. M. French, H. B. Bluestein, P. M. Markowski, and Y. P. Richardson, 2014: VORTEX2 observations of a low-level mesocyclone with multiple internal rear-flank downdraft momentum surges in the 18 May 2010 Dumas, Texas, supercell. *Mon. Wea. Rev.*, **142**, 2935–2960, doi:10.1175/MWR-D-13-00240.1.

Smith, T. C., S. G. Benjamin, J. M. Brown, S. Weygandt, T. Smirnova, and B. Schwartz, 2008: Convective forecasts from the hourly updated, 3-km high resolution rapid refresh (HRRR) model. *24th Conf. on Severe Local Storms*, Savannah, GA, Amer. Meteor. Soc., 11.1, https://ams.confex.com/ams/24SLS/techprogram/paper_142055.htm.

Straka, J. M., E. N. Rasmussen, R. P. Davies-Jones, and P. M. Markowski, 2007: An observational and idealized numerical examination of low-level counter-rotating vortices toward the rear flank of supercells. *Electron. J. Severe Storms Meteor.*, **2**(8), 1–22, doi:10.55599/ejssm.v2i8.13.

Tao, T., and T. Tamura, 2020: Numerical study of the 6 May 2012 Tsukuba supercell tornado: Vorticity sources responsible for tornadogenesis. *Mon. Wea. Rev.*, **148**, 1205–1228, doi:10.1175/MWR-D-19-0095.1.

Thiel, H., 1950: A rank invariant method of linear and polynomial regression analysis i, ii, iii. Proceedings of the Koninklijke Nederlandse Akademie Wetenschappen, *Series A Math. Sci.*, **53**, 386-392, 521-525, 1397-1412.

Thompson, R. L., B. T. Smith, A. R. Dean, and P. T. Marsh, 2013: Spatial distributions of tornadic near-storm environments by convective mode. *Electronic J. Severe Storms Meteor.*, **8**(5), 1–22.

Trapp, R. J., 1999: Observations of nontornadic low-level mesocyclones and attendant tornadogenesis failure during VORTEX. *Mon. Wea. Rev.*, **127**, 1693–1705, doi:10.1175/1520-0493(1999)127<1693:OONLLM>2.0.CO;2.

Trapp, R. J., G. J. Stumpf, and K. L. Manross, 2005: A reassessment of the percentage of tornadic mesocyclones. *Wea. Forecasting*, **20**, 680–687, doi:10.1175/WAF864.1.

Tuftedal, K. S., M. M. French, D. M. Kingfield, and J. S. Snyder, 2021: Observed bulk hook echo drop size distribution evolution in supercell tornadogenesis and tornadogenesis failure. *Mon. Wea. Rev.*, **149**, 2539–2557, doi:10.1175/MWR-D-20-0353.1.

Varble, A., E. J. Zipser, A. M. Fridlind, P. Zhu, A. S. Ackerman, J. Chaboureau, S. Collis, J. Fan, A. Hill, and B. Shipway, 2014: Evaluation of cloud-resolving and limited area model intercomparison simulations using TWP-ICE observations: 1. Deep convective updraft properties. *J. Geophys. Res. Atmos.*, **119**, 13891–13918, doi:10.1002/2013JD021371.

Wakimoto, R. M., C. Liu, and H. Cai, 1998: The Garden City, Kansas, storm during VORTEX 95. Part I: Overview of the storm's life cycle and mesocyclogenesis. *Mon. Wea. Rev.*, **126**, 372–392, doi:10.1175/1520-0493(1998)126<0372:TGCKSD>2.0.CO;2.

Wicker, L. J., and R. B. Wilhelmson, 1995: Simulation and analysis of tornado development and decay within a three-dimensional supercell thunderstorm. *J. Atmos Sci.*, **52**, 2675–2703, doi: 10.1175/1520-0469(1995)052<2675:SAAOTD>2.0.CO;2.

Wilcoxon, F., 1945: Individual comparisons by ranking methods. *Biom. Bull.*, **1**, 80–83, doi:10.2307/3001968.

Wolfensberger, D. and A. Berne, 2018.: From model to radar variables: a new forward polarimetric radar operator for COSMO, *Atmos. Meas. Tech.*, **11**, 3883–3916, doi:10.5194/amt-11-3883-2018.

Wurman, J., D. Dowell, Y. Richardson, P. Markowski, E. Rasmussen, D. Burgess, L. Wicker, and H. B. Bluestein, 2012: The second verification of the origins of rotation in tornadoes experiment: VORTEX2. *Bull. Amer. Meteor. Soc.*, **93**, 1147–1170, doi:10.1175/BAMS-D-11-00010.1.

Zhu, P., J. Dudhia, P. R. Field, K. Wapler, A. Fridlind, A. Varble, E. Zipser, J. Petch, M. Chen, and Z. Zhu, 2012: A limited area model (LAM) intercomparison study of a TWP-ICE active monsoon mesoscale convective event. *J. Geophys. Res. Atmos.*, **117**, D11208, doi:10.1029/2011JD016447.

Ziegler, C. L., E. N. Rasmussen, T. R. Shepherd, A. I. Watson, and J. M. Straka, 2001: The evolution of low-level rotation in the 29 May 1994 Newcastle–Graham, Texas, storm complex during VORTEX. *Mon. Wea. Rev.*, **129**, 1339–1368, https://doi.org/10.1175/1520-0493(2001)129<1339:TEOLLR>2.0.CO;2.

Zittel, W. D., 2019: Theory and concept of operations for multi-PRF dealiasing algorithm’s VCP 112. New Radar Technologies Web Page, NOAA/NWS/Radar Operations Center, 13 pp., https://www.roc.noaa.gov/WSR88D/PublicDocs/NewTechnology/Theory_ConOps_VCP112.pdf.